A Flexible Single-Step 3D Nanolithography Approach via Local Anodic Oxidation: Theoretical and Experimental Studies

By

Jian Gao

A thesis submitted to the University of Strathclyde

for the degree of

Doctor of Philosophy

Centre for Precision Manufacturing

Department of Design, Manufacturing and Engineering Management

Faculty of Engineering

University of Strathclyde

April 2023

Declaration Statement

This thesis is the result of the author's original research. It has been composed by the author and has not been previously submitted for examination, which has led to the award of a degree.

Signed: Jian Gao Date: 28/04/2023

List of Publications

This thesis is partially based on four previously published works, including three journal articles and one conference proceeding. These publications are outlined below.

- **Gao, J.**, Luo, X. C., Fang, F. Z., & Sun, J. N. (2021). Fundamentals of Atomic and Close-to-atomic Scale Manufacturing: a review. *International Journal of Extreme Manufacturing*, 4(1), 012001. https://doi.org/10.1088/2631-7990/ac3bb2

- **Gao, J.**, Luo, X. C., ... & Fan, P. F. (2023). Atomistic Insights into Bias-Induced Oxidation on Passivated Silicon Surface through Reaxff MD Simulation. *Applied Surface Science*, 626, 157253. https://doi.org/10.1016/j.apsusc.2023.157253

- **Gao, J.**, Luo, X. C., ... & Yan, Y. D. (2022). Three-dimensional Nanostructures Enabled by Customised Voltage Waveform-Induced Local Anodic Oxidation Lithography. In Proceedings of the 22nd International Conference and Exhibition of the European Society for Precision Engineering and Nanotechnology (pp. 285-288). https://www.euspen.eu/knowledge-base/ICE22262.pdf

- Luo, X. C., **Gao, J.**, ... & Hasan, R. Md. M. (2023). Flexible Single-Step Fabrication of Programmable 3D Nanostructures by Pulse-Modulated Local Anodic Oxidation. *CIRP Annals - Manufacturing Technology*, https://doi.org/10.1016/j.cirp.2023.04.030

The work reported in each paper was conducted by the author of this thesis as an individual PhD student. In each case, co-authors provided the same level of general and editorial guidance as they provided for the PhD thesis as a whole.

Signed: Jian Gao Date: 28/04/2023

Other publications during PhD:

- **Gao, J.**, Luo, X. C., Xie, W. K., & Qin, Y. (2023). Annisotropy Study of Bias-Induced Oxidation on Silicon. *Surfaces and Interfaces*, (To submit)
- **Gao, J.**, Luo, X. C., ... & Geng, Y. Q. (2022). Insight into Atomic-Scale Adhesion at the C–Cu Interface During the Initial Stage of Nanoindentation. *Nanomanufacturing and Metrology*, 5(3), 250-258. https://doi.org/10.1007/s41871-022-00149-3
- Fan, P. F., **Gao, J.**, ... & Luo, X. C. (2022). Scanning Probe Lithography: State-of-the-art and Future Perspectives. *Micromachines*, 13(2), 228. https://doi.org/10.3390/mi13020228
- **Gao, J.**, Luo, X. C., ... & Geng, Y. Q. (2021). A First-principles Study of the Atomic-scale Adhesion in Nanoscratching of Copper by an Atomic Force Microscope Tip. Paper presented at *7th International Conference on Nanomanufacturing, Xi'an, China*. (Oral presentation, paper recommended to the journal of *Nanomanufacturing and Metrology*)
- Luo, X. C., Guo, X. G., **Gao, J.**, Goel, S., & Chavoshi, S. Z. (2022). Molecular Dynamics Simulation of Advanced Machining Processes. In *Advanced Machining Science* (pp. 385-424). *CRC Press*. https://doi.org/10.1201/9780429160011

Abstract

The field of nanotechnology has experienced rapid growth in recent years, fuelled by the increasing need for high-performance next-generation nano/quantum devices/products possessing 3D nanostructures with sub-10 nm feature sizes. As a result, there is a high demand for a new flexible nanofabrication technique capable of generating various 3D nanostructures with high precision and efficiency. Local anodic oxidation (LAO) nanolithography is a promising nanofabrication technique for the in-lab prototyping of nanoproducts due to its high precision, low environmental requirement, and ease of use. However, challenges remain with current LAO nanofabrication techniques to meet the processing demands of next-generation nanoproducts. These challenges include limited throughput, high defect rates, and inflexibility in generating various nanostructures. Consequently, the existing 3D LAO nanofabrication methods suffer from high costs and inefficiencies. Addressing these challenges is crucial for advancing the capabilities of LAO nanolithography and unlocking its full potential in nanofabrication. In this thesis, a novel flexible single-step nanofabrication approach was developed to generate diverse 3D nanostructures with sub-10 nm feature sizes through pulse-modulated LAO nanolithography. Compared with other tool and condition control methods, pulse modulation is easier to achieve with precise tunability, enabling flexible, high-precision, and cost-effective 3D nanofabrication.

A clear and in-depth understanding of the manufacturing mechanisms at the atomic and molecular scales is crucial in determining the influencing factors during the manufacturing process. This thesis thus first used the reactive force field (ReaxFF) molecular dynamics simulation method to investigate the reaction mechanisms of the

LAO process. A comprehensive analysis of bonding, molecular, and charge indicates that the bias-induced oxidation led mainly to the creation of Si–O–Si bonds in the oxide film and the consumption of H_2O. In contrast, the oxidised surface's chemical composition remained unchanged during the bias-induced oxidation process. In addition, parametric studies further revealed the dependence of electric field strength and humidity on the bias-induced oxidation process and their respective influencing mechanisms. A good agreement was achieved through qualitative comparison between simulation and experimental results.

Secondly, this thesis proposed a new pulse-modulated LAO nanolithography approach to realise flexible and efficient fabrication of various 3D nanostructures. The process was designed on the principle that the amplitude or width of the pulse can control the lateral and vertical growth of each nanodot while the tuning of pulse periods can determine the position of each nanodot based on certain tip scan speeds and trajectories. Feasibility tests were conducted on an atomic force microscope (AFM) to demonstrate the capability of this approach in fabricating various nanostructures with the minimum linewidth at sub-10 nm and height variations at sub-nm.

Finally, nanofabrication experiments were conducted to investigate the capabilities of pulse-modulated LAO nanolithography in achieving flexible, accurate, and efficient fabrication of 3D nanostructures. Based on the systematic parametric study on the effects of pulse period, amplitude, and width through the LAO experiment, a process model was developed to provide a clear and detailed interpretation of the nanofabrication process. This model links the geometry of 3D nanostructures with arrays of pulse periods, amplitudes, and widths, allowing for active control of the LAO process. The fabrication of several 3D nanostructures was experimentally validated by

comparing the fabricated and predicted results, demonstrating good agreement. The fabricated three-dimensional curved surface could achieve the average form accuracy and precision at sub-nm levels. Higher efficiency was achieved by using a high scan rate, enabling the creation of a nanoscale lens structure consisting of four thousand nanodots within 50 seconds. The efficiency and accuracy of the proposed flexible single-step nanofabrication approach were, therefore, fully demonstrated.

Acknowledgments

I would like to express my sincere gratitude to my supervisor, Prof. Xichun Luo, for providing invaluable guidance, support, and encouragement throughout my PhD study. I would also like to thank my co-supervisor, Prof. Yi Qin, for his support and for offering me a research assistant position in his group. I am deeply grateful to Dr. Wenkun Xie for his insightful suggestions for my research works.

Special thanks to my colleague Mr. Dino Bertolaccini for the valuable suggestions and guidance for the development of the pulse generator. I would also like to thank Dr. Francisco Espinosa Barea from Instituto de Ciencia de Materials de Madrid, CSIC, Spain, as well as Dr. Sergey Lemeshko and Dr. Vishal Panchal from Bruker Corporation for the guidance on the AFM operation. I am grateful to Prof. Fengzhou Fang and Prof. Jining Sun for providing valuable suggestions for journal publications.

I am sincerely grateful to my parents, uncles and aunts for their unwavering care, support and love. Also, I would like to thank my girlfriend, Dr. Junfan Qu, for her patience, love, support and encouragement.

I would also like to express my thanks to my friends and colleagues, including Dr. Wenlong Chang, Dr. Yankang Tian, Dr. Rashed Hasan, Dr. Pengfei Fan, Dr. Zhengjian Wang, and everyone at the Centre for Precision Manufacturing who have been supportive and helpful throughout my research journey.

Financial support from EPSRC (EP/K018345/1, EP/T024844/1, EP/V055208/1), the Royal Society-NSFC international exchange programme (IEC\NSFC\181474), and UKRI Fellowship programme (EP/X021963/1) is thankfully acknowledged. I also recognise the use of the ARCHIE-WeSt High-Performance Computer at the University of Strathclyde for simulation research.

Table of Contents

List of Tables

List of Figures

Nomenclature

U	interaction energy
σ'	equilibrium separation, van der Waals radius
r	interparticle distance
ε	depth of the potential well
Ψ	wave function
n	principal quantum number
l	angular quantum number
ml	magnetic quantum number
$\frac{1}{2}\hbar, -\frac{1}{2}\hbar$	spin angular momentum
$\boldsymbol{r}$	position vector
t_i	time
i	imaginary unity
$\hbar$	reduced Planck's constant
$\hat{\mathrm{H}}$	Hamiltonian operator
λ	de Broglie wavelength
h	Planck's constants
m	mass
v	velocity
E	energy
E_{bond}	bond order energy
E_{val}	valence angle energy
E_{tors}	torsion angle energy

E_{over}	over-coordination penalty energy
E_{under}	undercoordination penalty energy
E_{lp}	long-pair energy
BO_{ij}	bond order between two atoms i and j
r_{ij}	the interatom distance between atoms of i and j
r_0^{σ}	semi-empirical parameters for sigma bonds
r_0^{π}	semi-empirical parameters for π bonds
$r_0^{\pi\pi}$	semi-empirical parameters for double π bonds
p_{bo}	semi-empirical parameters for bond orders
E_{vdW}	van der Waals interaction energy
E_{Coul}	Coulomb interaction energy
E_{H-bond}	H-bonds energy
V	Coulomb potential
$\boldsymbol{p}$	momentum
Φ	scalar potential
$\boldsymbol{A_v}$	vector potential
e	electron charge
m_0	the rest mass of the electron
c	speed of light
M	mass of the atom
θ	scattering angle during the interaction
x_1, x_2	positions of two electrons
w_{ee}, v_{ext}	soft-Coulomb potential
T_k	kinetic energy of the target atom

ϑ	scatter angle in the centre of mass coordinate system
(x_{ci}, y_{ci})	tip position, or the centre coordinate of each nanodot
T'	pulse start time
f	scan rate
L	scan size
d	spacing between the adjacent scan lines
h_o	oxide line height
w_o	oxide line width
A	pulse amplitude
t	pulse width
T	pulse period
p	profile of a Gaussian surface
C	proportional constant of Gaussian function
σ	standard deviation of Gaussian function
d_f	full diameter at half height
P	profile of nanostructures
$\boldsymbol{V}$	the amplitudes of a series of pulses
$\boldsymbol{t}$	the widths of a series of pulses
$\boldsymbol{T}$	the periods of a series of pulses
V_{ref}	analog reference voltage
V_{out}	output voltage
V_{dac}	digital DAC output
t_{delay}	delay setting time

Abbreviations

EBL	electron beam lithography
FIBL	focused ion beam lithography
EUVL	extreme ultraviolet lithography
SPL	scanning probe lithography
LAO	local anodic oxidation
ReaxFF	reactive force field
MD	molecular dynamics
AFM	atomic force microscope
STM	scanning tunnelling microscope
SPM	scanning probe microscope
HDL	hydrogen depassivation lithography
DFT	density functional theory
DFTB	density functional based tight binding
KMC	kinetic Monte Carlo
o-SPL	oxidation scanning probe lithography
SPC/E	extended simple point charge model
TIP3P	transferable intermolecular potential 3P
DC	direct current
ALE	atomic layer etching
ALD	atomic layer deposition
TMA	trimethylaluminum
DNQ	diazonaphthoquinone
IC	integrated circuit

TD-DFT	time-dependent density functional theory
FEBE	focused electron etching
FEBD	focused electron beam deposition
SEM	scanning electron microscope
STEM	scanning transmission electron microscope
HIB	Helium ion beam
FIB	focused ion beam
ACSM	atomic and close-to-atomic scale manufacturing
LJ	Lennard-Jones
LDA	local density approximation
GGA	generalized gradient approximation
LAMMPS	Large-scale Atomic/Molecular Massively Parallel Simulator
QEq	charge equilibration
NVT	canonical ensemble
RDF	radial distribution functions
RH	relative humidity
SCM	scanning capacitance microscopy
FWHM	full width at half maximum
FDHM	full diameter at half maximum
P–P	peak to peak
API	application programming interface
CoO	cost of ownership

Chapter 1 Introduction

1.1 Background

Nanomanufacturing has enabled the creation of small structures with unique properties arising from quantum, electromagnetic, and thermal effects. This has led to the development of nanotechnology-enabled products in various fields, including data storage, clean energy, quantum computing and communication. In recent years, emerging next-generation nano/quantum products and devices, such as heat-assisted magnetic recording hard disks, atomic clocks, photonic integrated circuits, and plasmonic solar cells, feature higher performance and unique functionalisation. These products are designed with extremely small feature sizes and diverse shapes on different materials, raising the need for cost-effective and flexible 'lab-to-fab' nanofabrication techniques.

Current semiconductor-based nanofabrication approaches, including optical lithography, electron beam lithography (EBL), focused ion-beam lithography (FIBL), self-assembly, nanoimprint lithography, and scanning probe lithography (SPL), are either expensive, slow or suffer from high defect rates due to multi-step processing for complex nanostructures [1]. For example, optical lithography and EBL/FIBL often rely on capital-intensive equipment with the cost ranging from $1 million for an EBL system to $450 million for the latest extreme ultraviolet lithography (EUVL) machine [2]. Nanoimprint lithography is usually performed based on expensive industrial-scale machines and often suffers from a high defect rate during mould release [3]. EBL, FIBL, and SPL are slow and limited in scalability [1,4]. Self-assembly is low-cost but limited in the fabrication of complex and 3D nanostructures [5]. In addition, some of

these methods could be inflexible in generating nanostructures with various shapes, as one type of tool (mask/stamp) can only make one type of structure.

Local anodic oxidation (LAO) nanolithography is a promising candidate technique to achieve the fast and flexible prototyping of functional nanoproducts due to its advantages in atomic-level resolution, direct surface patterning ability, and low instrument cost [6,7]. This nanofabrication process relies on the controlled oxidation of conductive surfaces in anodic solutions, which is induced by an enhanced local electric field achieved by applying a bias between the nanoscale probes/electrodes and substrate. Despite the significant progress made in LAO nanolithography, several challenges must be addressed to meet the processing demands of the next-generation nanoproducts. Firstly, the underlying mechanisms of the process have not been fully discovered due to the difficulties in experimental observation of the chemical reactions involved. Furthermore, the current nanofabrication process for diverse 3D nanostructures through LAO is often accompanied by low throughput, high defect rates, and inflexibility due to its dependence on complex and expensive control systems or multi-step operations. Overcoming these challenges and constraints of LAO nanolithography thus becomes the key motivation behind this thesis.

1.2 Aim and objectives

The aim of this thesis is to establish a flexible, cost-effective, and efficient nanofabrication process for 3D nanostructures based on the LAO technique. Uncovering the underlying reaction mechanisms during the LAO process is also a crucial aspect of this research, as it will aid in the fundamental understanding and optimisation of the nanofabrication process. The primary objectives are:

- To identify fundamental knowledge gaps and research challenges in atomic scale and sub-10 nm manufacturing techniques.
- To gain an in-depth atomistic understanding of the reaction mechanism and the parametric effects of the LAO process.
- To establish a flexible 3D LAO nanolithography process and a test platform.
- To develop an analytical process model for pulse-modulated LAO nanolithography.
- To validate the pulse-modulated LAO nanolithography process through fabricating various 3D nanostructures.

1.3 Thesis structure

This thesis is organised in six chapters, as outlined in Figure 1-1.

Chapter 1 introduces the background, motivation, aim, and objectives of this research. It also lays out the structure of the thesis.

Chapter 2 reviews the atomic scale and sub-10 nm manufacturing techniques, summarises the fundamentals of interactions among these manufacturing processes, and presents a comparison of reviewed nanolithography techniques. The knowledge gaps in sub-10 nm manufacturing research are also identified in this chapter.

Chapter 3 presents the reactive force field (ReaxFF) molecular dynamics (MD) simulation for the LAO process. A detailed and comprehensive analysis of the chemical bonds, molecules, and charges indicates that the dominant reactions of the LAO include the consumption of H_2O and the creation of Si–O–Si bonds. In addition, this chapter performs the parametric study, which demonstrates the effects of different electric fields and humidity on the LAO process.

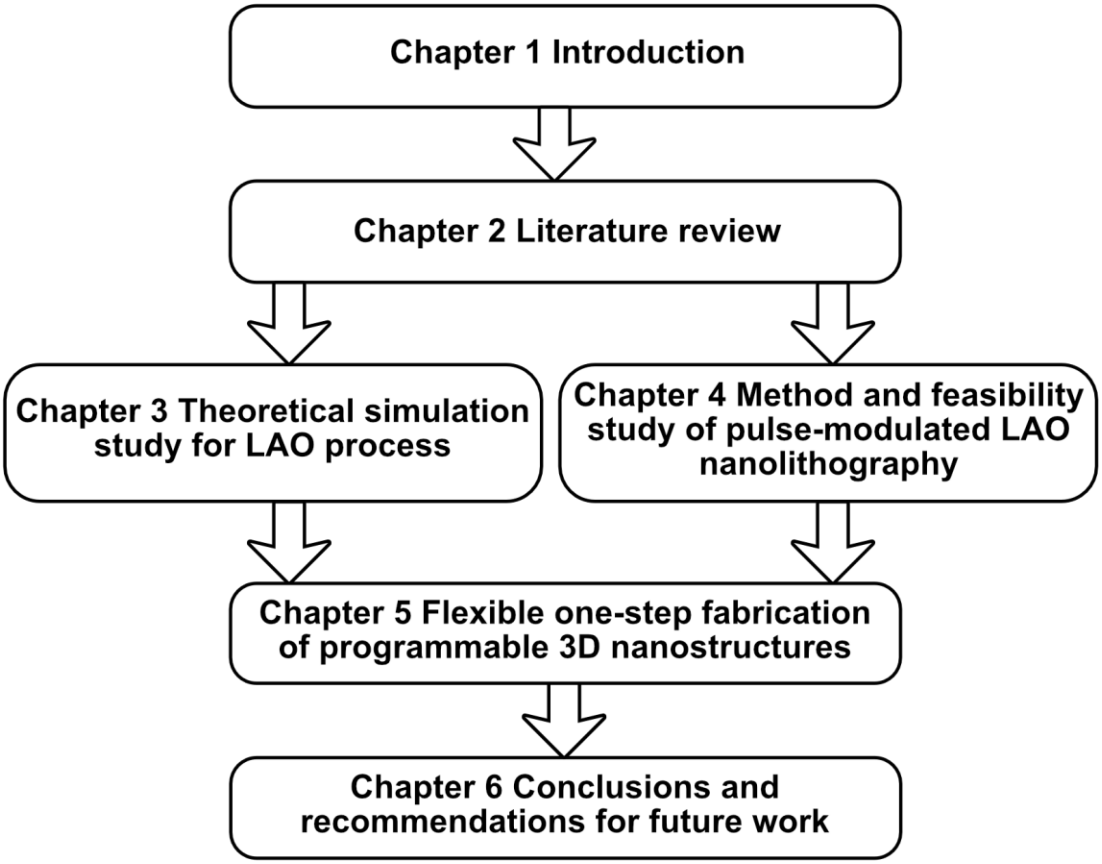

Figure 1-1. Flowchart of the thesis structure.

Chapter 4 proposes a new pulse-modulated LAO nanolithography process and its implementation on an atomic force microscope (AFM). The chapter also provides a feasibility study of the fabrication of various nanostructures using the proposed method and developed test platform.

Chapter 5 presents an analytical process model for the proposed pulse-modulated LAO nanolithography approach. This model is built through the experimental study of the relationship between pulse parameters and the geometry of the fabricated nanostructures. This chapter also presents the development and validation of a fully programmable pulse generator, through which the pulse-modulated LAO is used to fabricate complex 3D nanostructures. The nanofabrication experiments further

confirm that pulse-modulated LAO provides a flexible, effective, and efficient approach to achieving 3D nanofabrication with good accuracy and precision.

Chapter 6 presents the conclusions of this thesis and introduces research recommendations to enhance the nanofabrication capabilities of the proposed approach.

Chapter 2 Literature review

2.1 Introduction

This chapter reviews the current state of the art of manufacturing techniques at atomic and sub-10 nm scales, summarises fundamental interactions in these manufacturing processes and their descriptions, and presents a comparison of reviewed manufacturing techniques. In Section 2.2, advanced atomic scale or sub-10 nm manufacturing processes are introduced, including the mechanisms, dominant interactions, and theoretical research. In Section 2.3, a summary is given regarding the fundamentals of atomic and energy beam-matter interactions, along with their theoretical descriptions. Section 2.4 discusses the comparisons of reviewed techniques. Finally, Section 2.5 summarises the current research challenges and knowledge gaps.

2.2 State-of-the-art atomic scale and sub-10 nm manufacturing processes

As the functionality and performance of nanoproducts continue to advance, the manufacturing precision and feature scale required for the nanostructures are decreasing towards sub-10 nm or atomic scale [4,8]. Manufacturing at this scale was regarded as a new era of manufacturing with promising futures [9]. This section will introduce the atomic scale and sub-10 nm manufacturing processes in terms of mechanisms, dominant interactions, and simulation studies.

2.2.1 STM tip-based atom manipulation

2.2.1.1 Introduction

In 1990, IBM first achieved atom manipulation using a scanning tunnelling microscope (STM) to form the logo of ‘IBM’ with Xe atoms on a Ni surface [10]. After that, manipulation of Ag [11], Co [12], Pt [13], CO [14], H [15], and $B_{10}H_{14}$ [16]

was also accomplished. The atom manipulation experiments include lateral manipulation and vertical manipulation, as shown in Figure 2-1 (a) and (b). In lateral manipulation, the adatoms can be manipulated in pulling, sliding, or pushing manners [17]. Through adjusting the tip-sample distance and tunnelling current, the lateral 'pulling' can be realised by the following procedure: i) the conductive tip is placed at a close distance to surfaces, allowing the van der Waals forces to attract the adatom towards the tip; ii) as the tip scans the sample surface, the adatom can be pulled along the tip-scanning direction while remaining bound to the surface; iii) once the adatom arrives at the desired position, the tip is retracted to a higher position, leaving the adatom on the surface.

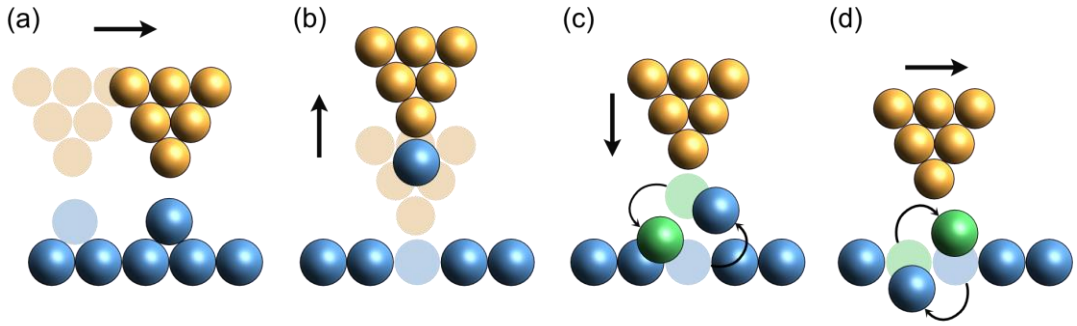

Figure 2-1. Schematic of SPM tip-based atom manipulation processes: (a) vertical manipulation, (b) lateral manipulation, (c) vertical interchange, and (d) lateral interchange.

With the help of tip-sample bias, STM can also induce vertical atom manipulation, as shown in Figure 2-1 (b). In the vertical manipulation process, the adatom must overcome the energy barrier that allows the transfer from the sample surface to the STM tip. As the tip gets closer to the adatom, the energy barrier can approach zero. Under the action of tunnelling current, the adatom can obtain energy from tunnelling electrons and transfer from the sample surface to the tip. When the tip is lifted from

the surface, the adatom can follow the tip and be pulled up. If a reverse voltage is applied, the adatom on the tip can also be transferred back to the surface when the tip-surface distance is small enough. Through this mechanism, vertical manipulation has been accomplished for Xe [18], CO [14], and H [15] atoms.

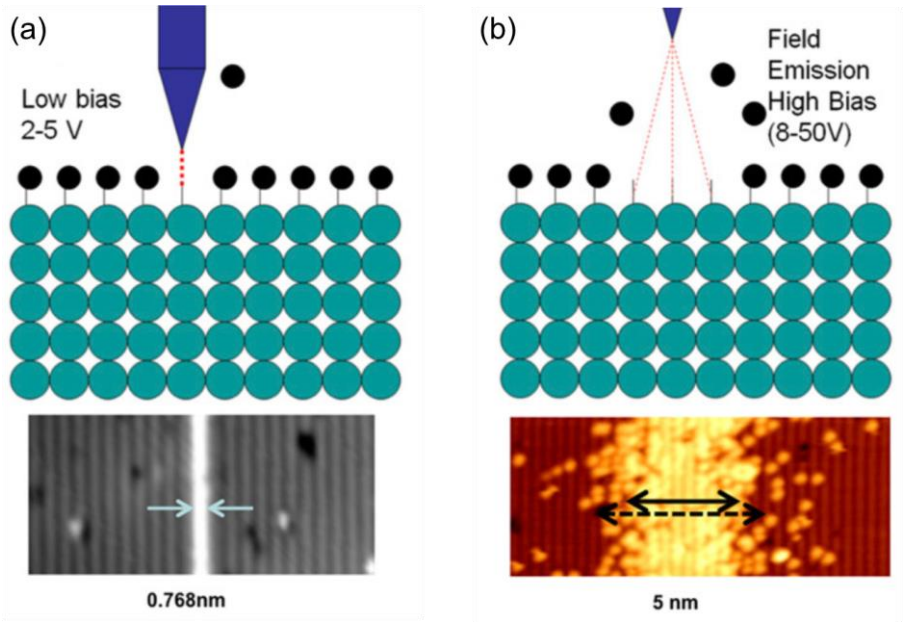

Figure 2-2. Schematic of two modes for HDL processes: (a) atomically precise mode HDL and (b) field emission mode HDL. Reprinted with permission from Ref [19]. Copyright (2018) American Vacuum Society.

In particular, the STM tip-based desorption of H-passivated Si (1 0 0)–2×1 [20] is also named hydrogen depassivation lithography (HDL), which is one of the popular atomically precision manufacturing methods. When the tunnelling current passes through the tip-sample gap, the Si–H covalent bonds break due to the interaction with electrons, and then the hydrogen atoms escape from the surface. Through the scanning of the tip, the hydrogen atoms are thus removed from the surface site by site [21]. The position and degree of desorption can be parametrically controlled over tip scanning and tunnelling current, which opens the possibility for automation.

To conclude, the mechanisms of atom manipulation or removal using STM tips are expressed as follows. For lateral manipulation, purely mechanical interactions, such as Pauli exclusion and van der Waals forces, dominate the process. For vertical manipulation, the tunnelling current provides the energy to induce manipulation. For the HDL process, the desorption of H atoms can occur in two different mechanisms under different tip-sample biases: field emission and vibrational excitation [15], corresponding to two operation modes of HDL, as shown in Figure 2-2 [21]. One mechanism is the field emission mode under which the bias voltage normally exceeds ~7 V. During this process, electrons will be field emitted from the tip to the sample. Because the energy of the incident electrons is higher than the desorption threshold energy, the interaction will expose H atoms on the surface. In field emission mode, the tip is usually at a higher position, and the exposure occurs within a large surface area; the resolution is thus limited to 5 nm [22]. Another is the atomically precise mode, which makes HDL a successful atomically precise manufacturing technique. It was experimentally shown that desorption occurs even when the electrons' energy is below the threshold (with a bias less than ~5 V [21]), but the desorption rate is significantly decreased and strongly dependent on the current. This indicates multiple electrons are involved in the desorption [15]. Persson [23] has demonstrated that the atom transfer is driven by a multiple vibrational excitation mechanism with energy coming from tunnelling electrons.

2.2.1.2 Simulation research

The quantum mechanics-based first-principles calculation is a reliable method to describe the nuclear-nuclear, electron-electron, and electron-nuclear interactions in the atom manipulation ensemble. In previous studies, first-principles methods have been

used to study the STM tip-based manipulation because of the accurate description of the relaxed atomic structures, interaction energy, and the energy barriers for atom transfer. These results contributed to the understanding of the process mechanisms and provided instructions on the experimental protocols. Kobayashi et al. [24] studied the vertical manipulation of a single Na atom between an STM tip and a surface, the results of which indicated that tip-surface bias caused different effects on positive and negative surfaces. Quaade et al. [25] studied the single-atom switch on silicon with the first-principles methods. Their studies showed that the electronic excitation of a localised surface resonance could explain the principal effects of switch control and a higher transfer rate at a higher temperature. Nguyen et al. [26] used the first-principles method to study the diffusion barrier of the Se vacancy on $PdSe_2$, which was lower than that of the vacancies on MoS_2 and TiO_2. Xie et al. [27] employed both semi-empirical and first-principles simulations to study the manipulation mechanisms of a Cu adatom on a Cu (1 1 1) surface. Their results summarised the influence of tip height and structures. Liu et al. [28] studied the STM atom manipulation on YBr_3, and the simulation determined the possibility of inserting Ti adatom into atomic pores and the energy barriers for vertical and lateral movements.

2.2.2 AFM tip-based atom manipulation

2.2.2.1 Introduction

Compared with STM tip-based manipulation, the AFM tip-based methods can work for more materials, including semiconductors, metals, and insulators. In 2003, Oyabu's group used the AFM for the first time for the atom manipulation experiment [29]. The experiment was conducted by vertically removing and depositing a Si atom on a Si (1 1 1)-(7×7) surface [29]. When an AFM tip indents on the sample, the interaction can

remove one atom from its equilibrium position or deposit one atom back into an existing vacancy at the surface. Later, AFM tip-based atom manipulation was also implemented in lateral directions with pulling and pushing manners [30]. Furthermore, the atom interchange mechanism was observed in the AFM tip-based manipulation experiment. The strongly bound atoms between the tip and sample may interchange both vertically [31] and laterally [32], as shown in Figure 2-1 (c) and (d). This mechanism differs from other previously reported mechanisms. Phenomenologically, atomic interchanges occur due to a reduction in diffusion barriers caused by tip-sample interactions.

2.2.2.2 Simulation research

Without the tunnelling current, AFM tip-based manipulation is mainly governed by short-range interactions. Depending on the materials of the tool and sample, the dominant interactions may include Pauli repulsion, ionic, covalent, and metallic bonding interactions. The quantum nature of these interactions suggests that the process needs to be described with the first-principles methods. The related simulation studies based on density functional theory (DFT) or density functional tight binding (DFTB) have been conducted to investigate the relaxation, atomic interactions, energy barriers for atom transfer or interchange, and minimum energy paths [33,34]. Sugimoto et al. [33] used the *fireball* code to unveil the vacancy-mediated lateral manipulation of adatoms on Si (1 1 1)-7×7 surface. It was found that the bonds between the adatom and the surface atoms were weakened under the tip-sample interaction, which reduced the barriers of atom diffusion between adjacent sites. This method was also used to explain the vertical atom interchange between the tip and Sn/Si (1 1 1)-($\sqrt{3}\times\sqrt{3}$) R30° surface [31], the key atomistic processes involved and the energy

barriers for the manipulations were studied. Enkhtaivan et al. [34] studied tip relaxation in lateral atom manipulation. Their findings indicated that the underlying mechanisms were the structural relaxation of the tip apex and the formation of the bonds with the diffusing adatom. Bamidele et al. [35] used a combination of first-principles methods and kinetic Monte Carlo (KMC) algorithm to study the dynamics and statistics for 'super'-Cu atoms on the p (2×1) Cu (1 1 0): O surface. A novel mechanism that combines the atomic jump and surface diffusion was revealed.

2.2.3 LAO nanolithography

In addition to atom manipulation, SPM tips can induce surface modifications by adding external energy or materials. The sharp tips provide strong localisation, enabling nanopatterning on material surfaces. These processes are collectively known as SPL techniques, which include thermal SPL [36,37], LAO nanolithography [6,7], dip-pen nanolithography [38], mechanical SPL or scanning probe machining [39], bias-induced SPL [40], and more [6,41,42].

Local anodic oxidation (LAO) nanolithography, also known as oxidation scanning probe lithography (o-SPL), is one of the most popular techniques because of the advantages of high resolution, direct surface modification ability, low instrument cost, high reproducibility, *in-situ* imaging, compatibility with other lithographic processes, and low environmental requirements [7]. Since Dagata et al. [43] first created nanoscale oxide patterns on Si (1 1 1) surface by introducing bias to the STM, this method has attracted considerable research interest and has been well developed due to various potential applications of nanoscale oxide. The height of oxide can achieve from several to tens of nanometres, which is robust enough to serve as a mask for subsequent etching [44]. In addition, the LAO process offers a direct and

straightforward method for modifying the sample surface, providing a feasible way to build nanoscale circuits, and showing great potential for the fabrication of nanoelectronics devices [45–52]. Recent advances with the use of multi-tip arrays or structured nanoelectrodes have demonstrated that LAO can enable large-scale nanopatterning on various materials, including metals, semiconductors, 2D materials, and thin-layer polymers [7,9,53–56].

2.2.3.1 Mechanism

LAO nanolithography is a process that involves controlled oxidation induced by localised electric field. For the LAO process on silicon surfaces in ambient conditions, the presence of an enhanced electric field and surface-adsorbed water were considered as essential conditions that induce a series of physical and chemical reactions [57].

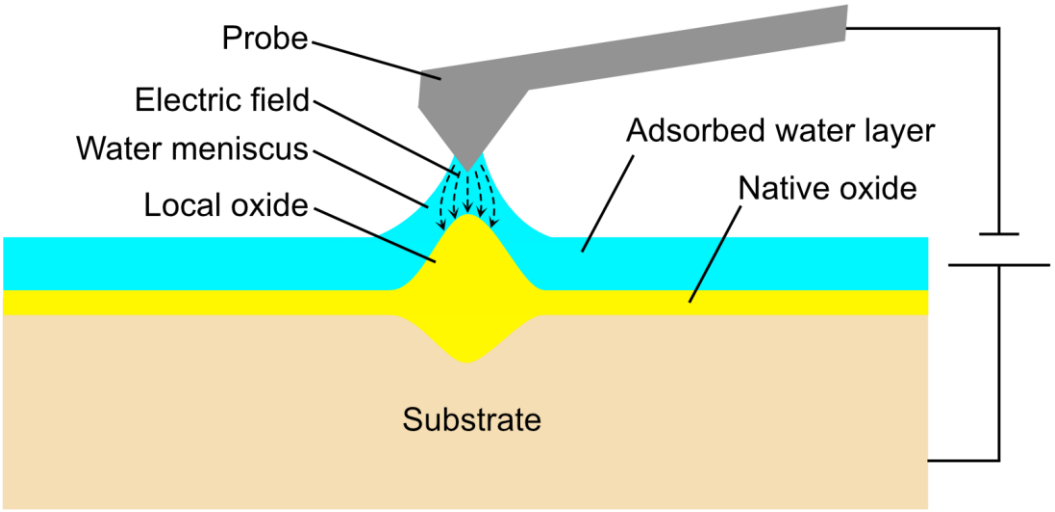

Figure 2-3. Schematic of LAO mechanism.

Figure 2-3 demonstrates the reaction mechanisms of LAO. When the tip and substrate are in close proximity, a water meniscus bridge can be formed (This process may require the application of a tip-surface bias). Then, the connection of the external power supply creates an enhanced electric field (order 10^9 to 10^{10} V/m [58–61])

between the tip and surface, which can dissolve the water molecules and direct oxyanions towards the substrate and form oxide on the surface. Since the volume of silicon oxide is larger than that of silicon [40], the oxidation process eventually results in surface oxide protrusions.

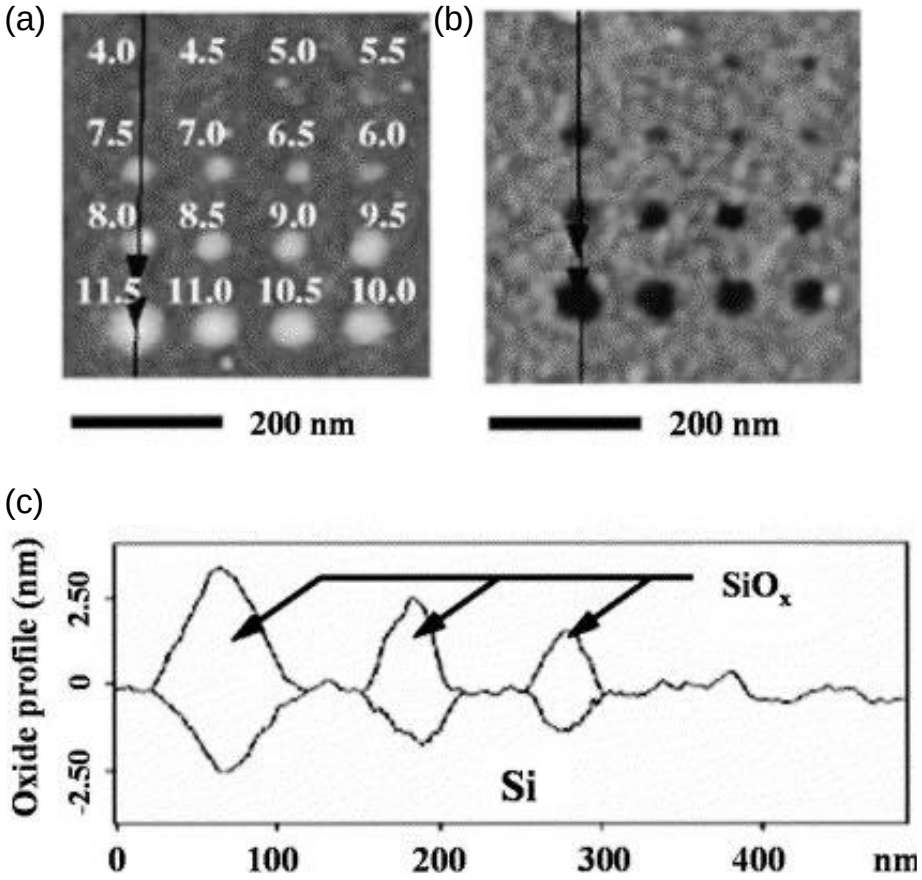

Figure 2-4. (a) Oxide dots made by LAO using tapping mode AFM on Si (1 0 0): H, p-doped (B), ρ = 14–21 Ω·cm. Writing parameters: pulse duration 20 ms, voltage from 4 to 11.5 V, and amplitude 2 nm, (b) same patterns after a 5 s HF dip, and (c) cross-sections of both measurements. Reprinted with permission from Ref [62]. Copyright (1998) AIP Publishing.

Fontaine et al. [62] conducted a study on the oxidized and post-etched surface, as shown in Figure 2-4. Their findings indicated that the height of the oxide corresponds

to 60% of the total height of the oxide thickness. The oxide created by LAO was also found with a lower density at 2.05 g/cm^3, compared to the silicon oxide obtained in thermal oxidation, which has a density of 2.27 g/cm^3 [63]. In addition, a large amount of water was found within the oxide created by LAO, with approximately 4–5% in mass [64,65]. This implies that the local oxide created by LAO may not be directly used to build transistors. Additional steps, such as post-annealing or integration with other semiconductor processing techniques, are required to enhance its compatibility and functionality.

Avouris et al. [60] measured a current of 10^{-14} A during the LAO process, which suggested that LAO is an electrochemical reaction process (Faradaic process) [66]. For the LAO process of a silicon substrate, they suggested that the reaction on the surface (anode) is [66]:

$$\mathrm{Si} + 4\mathrm{h}^+ + 2\mathrm{OH}^- \rightarrow \mathrm{SiO_2} + 2\mathrm{H}^+ \quad (2\text{-}1)$$

and the reaction on the tip (cathode) is [66]:

$$2\mathrm{H}^+ + 2e^- \rightarrow \mathrm{H_2} \quad (2\text{-}2)$$

On the basis of the above reactions, the oxidation growth depends on the transport of oxyanions between the tip and sample, which is influenced by the properties of substrate material, shape of the water layer, and tip-sample bias. Therefore, oxidation growth can be affected by various parameters, including tip scanning speed [62], tip-sample bias and separation[67], humidity [68], anodic solutions [59], and charge build-up [64]. However, the dominant mechanism varies depending on different voltage exposure times and oxide thicknesses. Snow et al. [69] conducted measurements on the kinetics of the LAO process under conditions of high humidity and pulsed bias. Their findings indicated that the oxidation reaction is mainly driven by the production

of OH^- ions in cases of moderate oxide thickness (a few nm) and exposure times (typically less than 10 ms). However, for long exposure times (typically more than 100 ms) and thick oxide, the kinetics can eventually be dominated by the effects of ion diffusion, space charge, and stress.

2.2.3.2 Simulation research on LAO nanolithography

To gain an in-depth understanding of these reactions, various simulation methods have been used in previous studies. Theogene et al. [70] used finite element simulations to study the underlying mechanism of electric field enhancement in the LAO process and decoupled the influence of applied voltage, tip curvature radius, semi-angle, and tip-sample distance on electric field distribution. The research outcome indicated that high electric field enhancement could be achieved through the use of a sharp tip with a small tip radius and a semi-angle. Cramer et al. [71] applied extended simple point charge model (SPC/E) potentials-based MD simulations to reveal and visualise the microscopic details of the bias-induced build-up process of the water bridge, which provided the molecular description of the threshold voltage and hysteresis behaviour. Choi et al. [72] used the transferable intermolecular potential 3P (TIP3P) model to simulate the water bridge formation, thinning, and snap-off, and obtained the simulation results-based force-distance curve, which is well consistent with the experimental results.

Despite these progresses in simulation studies, the mechanism of the chemical reactions between the conductive substrate and water layer remains incompletely understood. LAO process includes the chemical reactions within various chemical components and bonds, which are critical to the manufacturing process and its outcomes. However, due to the large number of atoms in the reaction system, including

water molecules, silicon, and their reactants, modelling using first-principles methods can be rather challenging. ReaxFF MD simulation, on the other hand, is an ideal approach for handling chemical reactions in a large number of molecules. It provides irreplaceable advantages in elucidating bonding interactions, chemical composition, and atomic dynamics behaviours, while also being more computationally efficient than first-principles methods [73,74]. This method has been successfully applied to similar reaction systems in the studies of surface oxidation [75–83], chemical mechanical polishing [84–89], nanoscale contact and tribology [90–92]. In the study of nanoelectrode lithography, Hasan et al. [93,94] used ReaxFF MD simulation to investigate the bias-induced oxidation mechanism and its dependence on the electric field, humidity, and crystallographic orientation. However, these studies assumed the oxidation began on a pristine silicon surface. In reality, upon exposure to atmospheric humidity, a surface passivation layer can be immediately formed on the surface before the introduction of the electric field. It can be inferred that the existence of the surface passivation layer will affect the subsequent bias-induced oxidation process, but it remains unclear.

2.2.3.3 LAO through AFM

Since Day and Allee [63] first applied AFM to achieve nano-oxidation, AFM has demonstrated a distinct advantage over its predecessor STM. The tip-sample bias required in LAO can be exerted independently of the microscope control of AFM, which allows a decent modulation of tip-sample distance, allowing a continuous and consistent reaction process. In addition, AFM can enable the concurrent fabrication and imaging of oxides, which facilitates the optimisation of process parameters. AFM

can work under three different modes for the LAO process: contact mode, tapping mode, and non-contact mode, as introduced in Figure 2-5.

2.2.3.3.1 Contact-mode AFM

When contact-mode AFM is used for LAO, a force in the range of 10 to 100 nN is applied to the sample surface while maintaining a zero tip-sample distance. The force exerted by the cantilever was considered with a slight but perceptible impact on the oxide height. However, it could weaken the tip lifetime and pattern reproducibility, particularly when using probes with small tip curvatures. Besides, due to the tip-sample contact, oxide patterns often exhibited a broad linewidth even when using probes with sharp tips. The large width of oxide patterns can be attributed to the scattering distribution of the electric field around the tip during the tip-sample contact. This phenomenon ultimately compromises the resolution of LAO lithography. However, when a large radius AFM tip is used, its robustness makes it possible to achieve high-speed LAO, which increases the patterning efficiency [95].

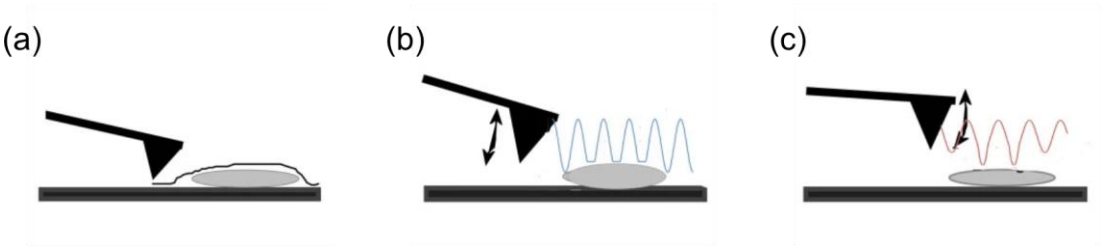

Figure 2-5. AFM operation modes: (a) contact mode, (b) tapping mode (intermittent contact), and (c) non-contact mode. Reprinted with permission from Ref [96]. CC BY 2.0. Copyright (2013) The Authors.

2.2.3.3.2 Tapping-mode AFM

Dynamic force microscopy has been developed by introducing an oscillating cantilever to the sample surface. Tapping mode is one of the dynamic modes of AFM, wherein

the tip is driven at a frequency close to the resonance frequency of the cantilever. The tip-surface contact is dominated by repulsive forces, which can be reflected by cantilever amplitude change. During the imaging and LAO nanolithography, the tip-sample contact can be maintained to be constant through the AFM control system. Compared with contact mode, tapping mode utilises an oscillation period in the order of 10^{-6} to 10^{-5} s, resulting in a shorter tip-sample interaction time and reduced shear forces on the tip. This leads to an extended tip lifetime, making tapping mode a preferred mode in both imaging and LAO application.

The formation of a water meniscus between the tip and sample is critical for the LAO process, which provides the necessary ionic species, strength-enhanced electric field, and spatial confinement to pattern the silicon surface. In contrast to contact mode AFM where water meniscus bridges the tip and sample naturally, tapping mode AFM kept the average tip-surface distance at a few to tens of nanometres. In this case, the formation of a water bridge has to be driven by the electric field [67,97]. The formation and breaking of the water bridge thus become important factors that affect the occurrence of the LAO process. Without a constant tip-sample contact, the lateral dimension of the water bridge can be reduced to several tens of nanometres. This provides a further restricted reaction region for oxidation, allowing the creation of sub-10 nm nanostructures.

2.2.3.3.3 Noncontact-mode AFM

Another dynamic mode used in LAO is the noncontact mode AFM. In this mode, the interaction between the tip and sample occurs within the attractive force range, ensuring that the tip never touches the surface. This configuration further extends the tip lifetime. Garcia et al. [97] first developed this approach and used pulsed voltages

in the milliseconds range to perform LAO even when the AFM tip did not directly contact the sample surface. Through this method, thousands of oxide dots are fabricated without causing any degradation of the needle tip, leading to further extended tip lifetimes and reduced surface defects. In addition, the tip-surface distance can be adjusted to enlarge or shorten the size of the water bridge. This operation can further reduce the oxide size [67,98], allowing the creation of sub-10 nm nanostructures (minimum feature sizes were found to be 4 nm after considering the tip convolution effect) [99,100]. The main drawback of this technique is that the feedback loop is turned off during the oxidation process, which makes it difficult to achieve large-scale continuous patterns.

2.2.3.4 Voltage supply

In the early stages of LAO nanolithography, continuous direct current (DC) voltages were used to achieve surface nano-oxidation. However, continuous DC voltage might not be necessary for the LAO process, as Snow and Campbell [95] reported that it took only a few microseconds to obtain 1 nm of oxide thickness. In addition, this method had a major drawback because the strong tip-surface interaction caused by DC voltage led to poor reliability of the tip. In 1999, Legrand and Stiévenard [101] demonstrated that pulsed voltage has several advantages over DC voltage in the LAO process, including reduced charge accumulation, more accurate voltage control, and enhanced reliability and resolution of the oxidation process [102]. As the duty cycle of the pulsed voltage can be kept very low, the average voltage value applied to the cantilever is typically less than 1 V. This prevents any undesirable reaction of the microscope feedback loop. In addition, LAO using high amplitude and short duration pulses can enhance the aspect ratio in resulting nanostructures because a high voltage pulse

produces a fast growth rate in the vertical direction, and a short pulse duration restricts the lateral diffusion of ionic species and space charge effects, together contributing to the aspect ratio enhancement [103]. In 2003, Clement et al. [104] obtained oxide patterns with an aspect ratio of 0.3 using 100 ns pulses.

2.2.3.5 3D nanofabrication

Since the invention of LAO nanolithography [43], a wide range of nanostructures have been fabricated, but most of them have relatively simple geometries in the shapes of nanodots, nanolines, or 2D surface patterns. The further development of LAO could depend on its capabilities, effectiveness and flexibility in achieving 3D nanostructures [105].

Lorenzoni and Torre [106] applied DC pulses to create the single nanodots on SiC with high aspect ratios and showed the potential for creating 3D structures consisting of arrays of multi-height dots step by step. Fernandez-Cuesta et al. [107] demonstrated the creation of multilayer nanostructures on silicon nitride films on silicon surfaces by applying different voltages during AFM scanning. They also discovered a correlation between the oxidation growth and the detected current, which was monitored during the reaction process. Johannes et al. [108] developed a more sophisticated computer-aided design coupled contact-mode LAO that can precisely replicate designed 3D nanopatterns. The height variations in the structures were achieved by applying various voltages during AFM scanning. Chen et al. [109] applied a similar method, named local gray-scale oxidation, where different voltages were used at each pixel to enable 3D nanopatterning and successfully fabricated lens nanostructures on the silicon substrate. Kim et al. [110] demonstrated that controlling the pulse duration can allow for precise dimensional control over nanoscale patterns. Furthermore, they showed that

repeated oxidation could create nanostructures with multilayers. Choi et al. [111] presented the nanofabrication of hierarchical nanostructures through a combination of LAO and wet etching. During the process, LAO was performed to create a resist layer which served as a mask for the further wet etching process. Kim et al. [112] found that repeated oxidation could create 3D pyramidal patterns, the mechanism of which is due to increased energy absorption. They also found that a 10-time repetition of LAO can apparently enhance oxidation growth along the *z*-axis. Yang and Zhao [113] used a coupling AFM lithography, in which probes served as both cutting tool and electrode, to create 2.5 D patterns on conductive materials with depths of 6–80 nm and square widths from the nanoscale to the microscale. They concluded that coupling AFM lithography can achieve a higher material removal rate and a smoother patterned surface in the fabrication of 2.5D hierarchical micro/nanostructures.

However, these methods have several limitations. First, contact-mode AFM was widely used for the LAO nanolithography process [106–109,111,113]. The tip-sample contact makes it difficult to achieve sub-10 nm feature size. Moreover, the tip wear caused by contact can easily compromise the patterning resolution and consistency, which adversely affect the results. Secondly, step-by-step operations or well-developed control systems [108–110,112,113] were utilised when obtaining 3D nanostructures, which can increase the error rate, lower the patterning efficiency, and raise the implementation cost. In addition, there is a lack of comprehensive studies on the effects of control parameters on the geometry of 3D nanostructures, hindering deterministic and digital 3D nanofabrication. Therefore, the development of a more precise, flexible, and efficient method is necessary to advance 3D LAO nanolithography further.

2.2.4 ALE

2.2.4.1 Introduction

Atomic layer etching (ALE) and atomic layer deposition (ALD) are two promising processing techniques in the industry for semiconductor materials. These techniques rely on the inherent chemical self-limiting properties of materials to ensure the removal or deposition of atomic layers.

ALE process consists of two reaction steps in each cycle, as shown in Figure 2-6 (a). The first step modifies the surface layer into easy-to-etch materials through the adsorption of precursors, and the second removes the reaction layer through energy species, typically a beam of low-energy ions [114]. The purge processes separate these two steps to remove extra precursors and by-products. In this ALE process, the uppermost interlayer chemical bonds are weakened by the chemical reactions in the first process and completely broken by ionic bombardment in the second.

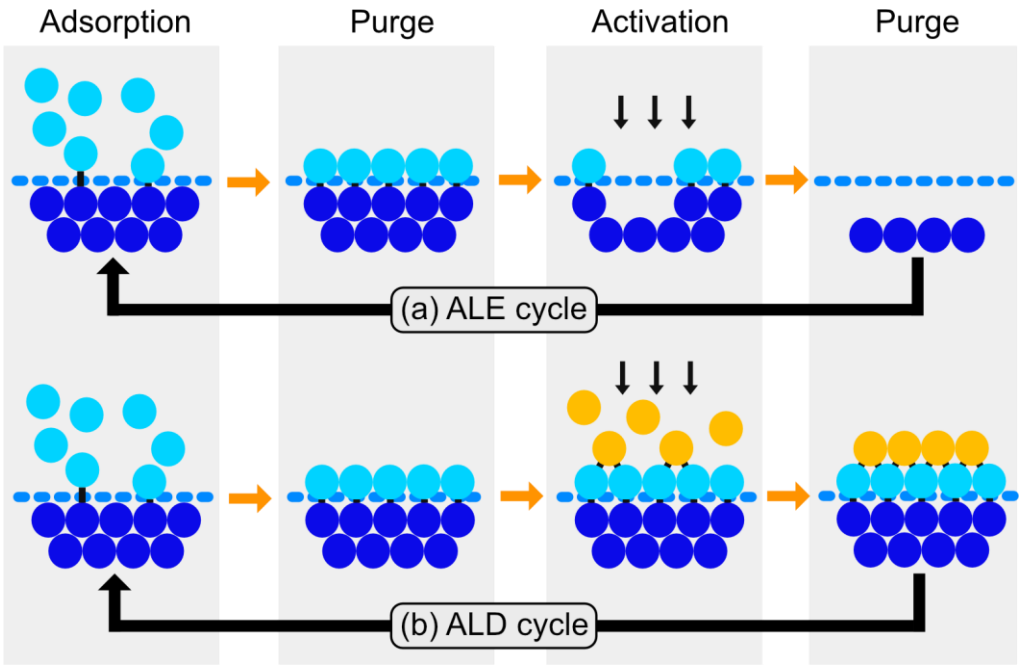

Figure 2-6. An illustration of self-limiting processes. One cycle of a typical (a) ALE process and (b) ALD process.

2.2.4.2 Simulation research

Chemical bonding apparently plays an important role in the ALE process. To give a better understanding of the bond forming and breaking, first-principles methods have been used to evaluate the reactivity and desorption energy in ALE processes. Konh et al. [115] used the DFT methods to calculate the energy required to remove Co atoms from Co (1 0 0) surfaces and the effect of surface defects on the etching process. Kim et al. [116] studied the energies for Cl adsorption and Ar^+-ion desorption on MoS_2 to unveil the mechanism of its ALE process. Longo et al. [117] studied ALE processes on an organic polymer surface using oxygen pulses. The results demonstrated the self-limiting nature of ALE and the fact that the formation of C–O–C bridge bonds leads to structural change.

2.2.5 ALD

2.2.5.1 Introduction

ALD is one of the most popular semiconductor processing techniques. Similar to ALE, the ALD process normally involves four processes, as demonstrated in Figure 2-6 (b). The main difference from ALE lies in the third step, which introduces another type of precursor, allowing the formation of a single layer of compound on the surface. As for the energy source, ALD can use thermal energy or plasma to enhance the reaction process. The plasma-enhanced ALD process can activate the chemical reaction even at a lower temperature with better film properties, which makes it a versatile method for nanofabrication in emerging applications [118]. In addition, the selective techniques provide a new method of ALD. Modifying the chemical properties of the surface can control the adsorption of precursors on the selected region. The selection strategies promote the formation of desired films on a surface while simultaneously

avoiding deposition in adjacent regions, which is considered a “chemical patterning” process [119]. The selective techniques will not only eliminate the edge placement errors in semiconductor nanomanufacturing but also bring us closer to the long-held dream of fabricating materials in a bottom-up fashion using atoms as building blocks [120–122].

2.2.5.2 Simulation research

The atomic-layer resolution of the ALD process relies on the chemical bonding interactions to bind the precursors and surface atoms. The chemical features of the precursor, including volatility, self-decomposition, reactivity with substrate, dissolution, and purity, require an in-depth understanding [123]. The first-principles method has been used in previous research to study the ALD process [124]. The simulation mainly aims to unveil the reaction energies, atomic structures, and diffusion barriers [125–127], with results assisting the design of precursors, the evaluation of reaction rates, and input parameters. Recently, ReaxFF MD simulation method was applied to the ALD process [128,129]. Through the modelling of chemisorb of trimethylaluminum (TMA) on Ge (1 0 0) surface, the temperature dependence of ALD was revealed with detailed reaction mechanisms. The results were found to be in good agreement with experimental measurement [128]. As such, ReaxFF can help determine the optimal processing conditions to produce high-quality deposition results. Furthermore, as the atomic-scale ALD is relative to the feature and reactor scale, the modelling of which normally requires multiscale modelling approaches [130]. A combined method of first-principles calculations and Monte Carlo simulation could address the stochastic nature, which makes it more suitable to simulate the collaborative and kinetic behaviours of the ALD process [131–133]. The results are

expected to provide better control over the reactions and further optimisation of processing parameters.

2.2.6 Laser-based processes

2.2.6.1 Introduction

Photolithography is a sophisticated technique widely used in semiconductor industry, and its recent advance has promoted the commercialisation of the 5 nm process. The interaction between light and electrons in molecules is the basic mechanism of the photolithography process. Just as electrons occupy atomic orbitals in atoms, electrons in molecules occupy molecular orbitals. When one or more photons are absorbed, an electron can transfer from one orbital to another, resulting in different outcomes depending on the atom or molecule to which the electron belongs. When an atom is excited by absorbing a photon, the electron that was activated to the high-energy orbital will normally jump back to the original orbital to sustain the ground state. However, there could be various consequences after an electron in a molecule is excited. For instance, the chemical bond can break if the electron moves from a bonding molecule orbital to an antibonding orbital. The broken bonds create dangling bonds with a high chemical reactivity and induce other chemical reactions. Eventually, if the process breaks down large molecules into smaller fragments and increases their solubility, the mechanism represents positive resist lithography; if the process leads to the creation of bonds between chains and forms more complex molecules, the process is called polymerizing and dominates the negative resist photography.

The photochemical reaction for positive resist is illustrated to describe the mechanisms of photolithography. The positive resist normally consists of three materials: a base resin, an inhibitor, and volatile solvents. The inhibitor, which is a sensitive compound

to light with a certain range of wavelengths, serves to impede the dissolution of resists. When exposed to light, the inhibitor will decompose due to the photochemical reaction, and the process will create soluble by-products and leave behind patterns after dissolving.

For example, diazonaphthoquinone (DNQ) can absorb ultraviolet light with wavelengths from approximately 300 nm to 450 nm. The absorption bands can be assigned to n-π* (S0–S1), and π-π* (S1–S2) transitions in the DNQ molecule. The DNQ decomposes through Wolff rearrangement to form a ketene [134]. In the presence of water, the decomposition product forms an indanecarboxylic acid, which is base-soluble, as shown in Figure 2-7. After dissolution, regions of the resist film that were unexposed to light will remain on the surface.

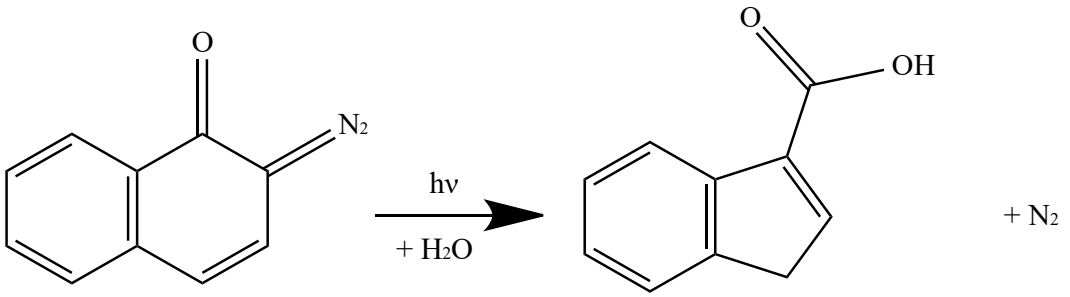

Figure 2-7. Photolysis of a DNQ molecule. Reprinted with permission from Ref [134]. Copyright (1992) American Chemical Society.

Classical photolithography is based on photochemical reactions, which has contributed to the miniaturisation of integrated circuit (IC) chips, but the theoretical limit makes it difficult to achieve atomic-scale patterns. One restriction lies in the sensitivity of photoresists. Classical photolithography normally uses resist materials that are very sensitive to laser dose, which makes the reaction region equal to or larger than the laser spot size. However, a recent study [135] proposed another light-based lithographic

method, where the chemical reaction is induced by the laser thermal effect, with the potential to further reduce feature size. The process utilised an inorganic resist with a higher reaction threshold for laser energy. The reaction only occurred at the centre area with close-to-maximum laser energy density, which made the feature size equal to or much smaller than the laser spot size. Similarly, through the photothermal effect, laser beams can also be taken as an alternative to STM for H-depassivation processes [136]. An ultraviolet laser can selectively heat silicon to a temperature so depassivation can occur while maintaining a good order of atoms on the surface. Compared with SPM tip-based method, the light-based process can greatly enhance the depassivation throughput. The workflow has been experimentally demonstrated [137].

2.2.6.2 Simulation research

As photolithography steps into the atomic or sub-10 nm scale, the atomic-scale effects of light-induced reactions on materials become more critical. Therefore, a reliable physical and mathematical modelling method is necessary to optimise this technique. The time-dependent density functional theory (TD-DFT) method has emerged in the study of laser-induced interactions and effects. This method combines the advantages of DFT and time-dependent formalism, allowing the accurate determination of absorption spectra, photochemical reactions, and excitations [138]. Waterland et al. [138] calculated materials' excitation energies and transition moments in the vacuum ultraviolet. The results could assist in searching materials for photolithography at a certain wavelength range. Palma et al. [139] used the TD-DFT method to explain the mechanisms of C–Br scission and C–C coupling processes in the photolithographic process of graphene nanoarchitecture. Ando [140] predicted the refractive index

dispersion of fluoro-compounds using the TD-DFT methods. The results identified some materials with high refractive indices and good transparency.

2.2.7 Focused electron/ion beam-based processes

2.2.7.1 Focused electron beam-based process

The aberration-corrected electron beam has reduced the electron beam spot to 0.1 nm^3 [141], which makes the electron beam a candidate tool for sub-10 nm or atomic scale manufacturing processes. Like photolithography, the electron beam can also create patterns by inducing chemical reactions in polymers. Through the interaction between electron beams and molecules, electrons in the bonds can be excited through inelastic scattering, thus breaking the bonds and changing the structure of the substrate. The electron-polymer interactions in EBL may lead to two results: the polymer chains may break into small fragments or break off the side groups and link to other chains to form larger molecules. Normally, both reactions happen together, but one of these will be the dominant process and determine the result. If irradiation causes a break in the main polymer chain so that it can be dissolved, the polymer is a positive resist. If irradiation links the chains and forms a network, making it insoluble, the polymer is a negative resist.

The inelastic scattering electron can also be used to induce the etching or deposition of precursors, which is known as focused electron beam etching (FEBE) or focused electron beam deposition (FEBD), as shown in Figure 2-8. In these methods, precursors are introduced near the substrate and absorbed on the surface. When the compound of precursors and surface atoms is exposed to a thin electron beam, normally by scanning electron microscope (SEM) or scanning transmission electron microscope (STEM), the electron-induced reaction will occur at the interaction region.

In the FEBE process, the reaction will convert surface atoms into volatile compounds, thus removing the surface atoms. In the FEBD process, the reaction will produce nonvolatile dissociation products and form the deposition. With the digital scanning of small-diameter beams and the proper selection of precursors and substrates, nanometre-scale structures can be created [142,143].

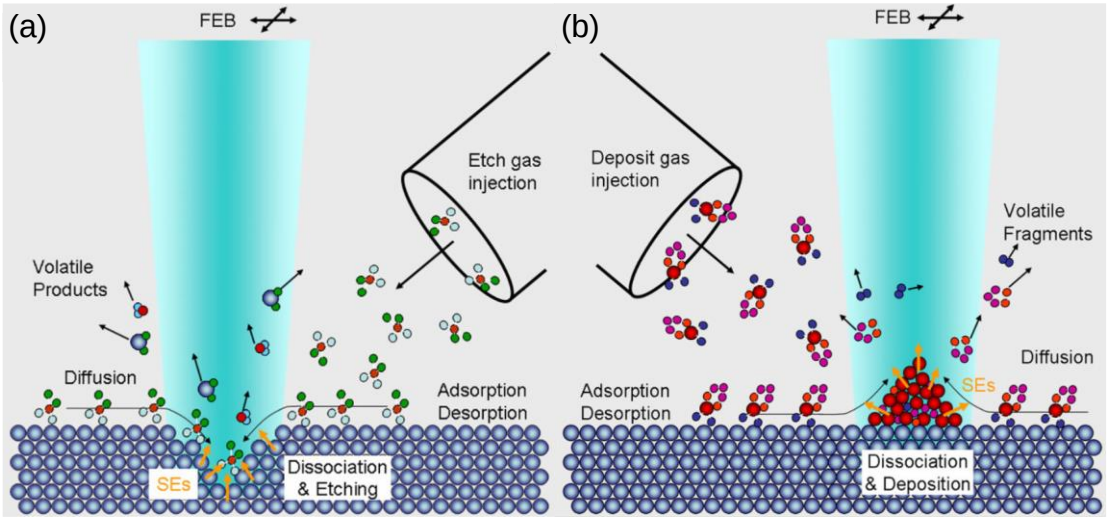

Figure 2-8. Schematics of (a) FEBE and (b) FEBD processes. Reprinted with permission from Ref [144]. Copyright (2015) American Vacuum Society.

For 2D materials, electron beams have been used to create atomic scale patterns or manipulate atomic defects [145]. The mechanism is through delivering high energy to the target atom and inducing atom displacement. When the energy delivered is higher than the displacement threshold, the atom can be ejected from its lattice site and form knock-on damage. Besides, the defect atoms in 2D materials that are weakly bound to substrate atoms can be manipulated to their nearby site by using a thin electron beam [146]. The underlying mechanism is that the energy delivered is higher than the atom diffusion threshold.

2.2.7.2 Focused ion beam-based processes

With the development of low-temperature ion sources, recent research has demonstrated the capability to generate ion beams with sub-nanometer spot sizes and a maximum current of several nanoamps [147–149]. This development positions them as a potential lithography tool for atomic scale and sub-10 nm manufacturing processes [150]. The helium ion beam (HIB) is one of these promising tools. The helium ion source can be made of a single crystal metal fabricated in a needle shape, with the end terminated with only several atoms (up to seven atoms) [151]. Such a unique configuration enables the HIB with ultra-fine spot size. In fact, the de Broglie wavelength of helium ions is smaller than electrons with the same energy (e.g., at 10 keV, the de Broglie wavelength for a helium ion and an electron is 0.1 and 10 pm, respectively), which indicates that HIB has a higher spatial resolution than an electron beam. Among all known elements, helium has the smallest atomic radius (~1/5 of a gallium ion), which makes it easier to pass through the sample, resulting in a deeper implantation depth.

The advantage is also evident in the case of helium ions due to their small atomic radius, which makes them highly resistant to scattering near the surface. This property enables a high lateral resolution, making helium ions an ideal tool for imaging and nanofabrication of thin-layer materials, particularly 2D materials. It has been experimentally demonstrated that HIB lithography can fabricate nanolines with less than 10 nm in width with a 20 nm pitch [153]. Due to its high spatial resolution at the surface, HIBs have been used in the nanofabrication of 2D materials, including graphene [154] and MoS_2 [155], achieving nanometre and sub-nanometre scale structures, the mechanism of which is demonstrated in Figure 2-9.

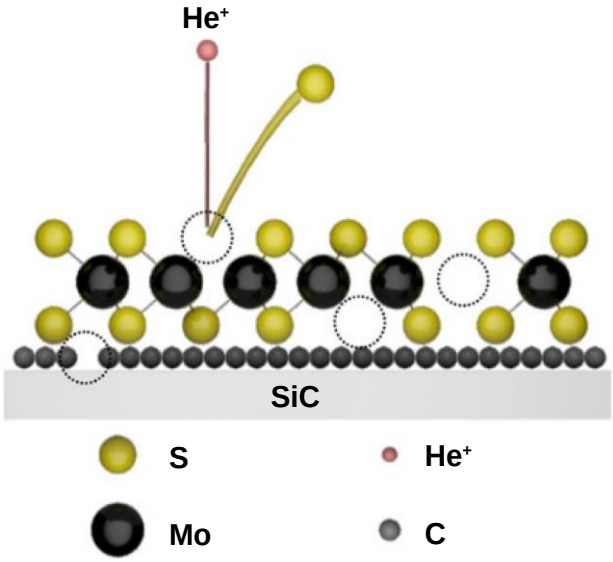

Figure 2-9. Schematic of defects created by helium ion sputtering on single-layer MoS_2 on graphene/SiC. The defects include sulphur vacancies, a molybdenum vacancy, and defects in the graphene layer. Reprinted with permission from Ref [152]. Copyright (2020) American Chemical Society.

In addition to subtractive manufacturing, focused ion beam (FIB) can also be used for additive manufacturing at micro- and nanoscales. FIB-induced deposition, also known as ion beam-assisted chemical vapour deposition, is another feature that is used extensively in FIB applications. Selected materials may be deposited onto a target surface by the introduction of appropriate gases into the system. The deposition process was first reported by Gamo et al. [156], who studied the process for the deposition of Al from $Al(CH)_3$ and W from WF_6. This technique provides the ability to deposit functional materials onto almost any solid substrate with nanometre spatial resolution. Unlike the ion sputtering process, which is mainly based on elastic scattering between the ions and target atoms, the deposition process is induced by the electrons generated in inelastic scattering. These secondary electrons could break the chemical bonds of the precursor gas molecules and form different components. Some

of which remain volatile, and others are deposited onto the surface. Tight beam control is critical to a successful FIB-assisted deposition since the precursor gas can easily be depleted and then cause the net deposition rate to be negative, resulting in net material removal. In order to maintain a constant positive deposition rate, the beam cannot stay at the same time point for a long time. It must move to another location and then come back to the same point to give the surrounding precursor gas enough time to replenish the depletion.

2.2.7.3 Simulation study

First-principles methods have been used to simulate the electron/ion beam-based manufacturing processes to reveal the mechanisms of beam-matter interactions. The threshold displacement energies for semiconductors were calculated in several studies [157–159] to evaluate the defects generation under the interaction of particle beams [160]. The defect formation under the particle beam-matter interaction can be described by either DFT or DFTB simulation, which could determine the irritation and defect features of the materials [161–163]. The electronic stopping mechanisms for certain materials were investigated by a TD-DFT method to evaluate the electronic stopping power [164–166] and electronic excitations [167,168]. Besides, the combination of TD-DFT and classical MD methods offered a simultaneous dynamic simulation of electrons and ions, which provided an unbiased insight into the interaction between the particle beams and target atoms [169].

2.3 Fundamentals of interactions in atomic scale and sub-10 nm manufacturing processes

As reviewed in the previous section, chemical bonding interactions are crucial in the manufacturing process at atomic or sub-10 nm scale, and their accurate description

requires simulation methods based on quantum theory rather than classic theory. This section will first summarise the different types of manufacturing and their simulation tools and dominant theories across scales. Then, the fundamentals of atomic and energy beam-matter interactions will be introduced along with their quantum mechanical descriptions.

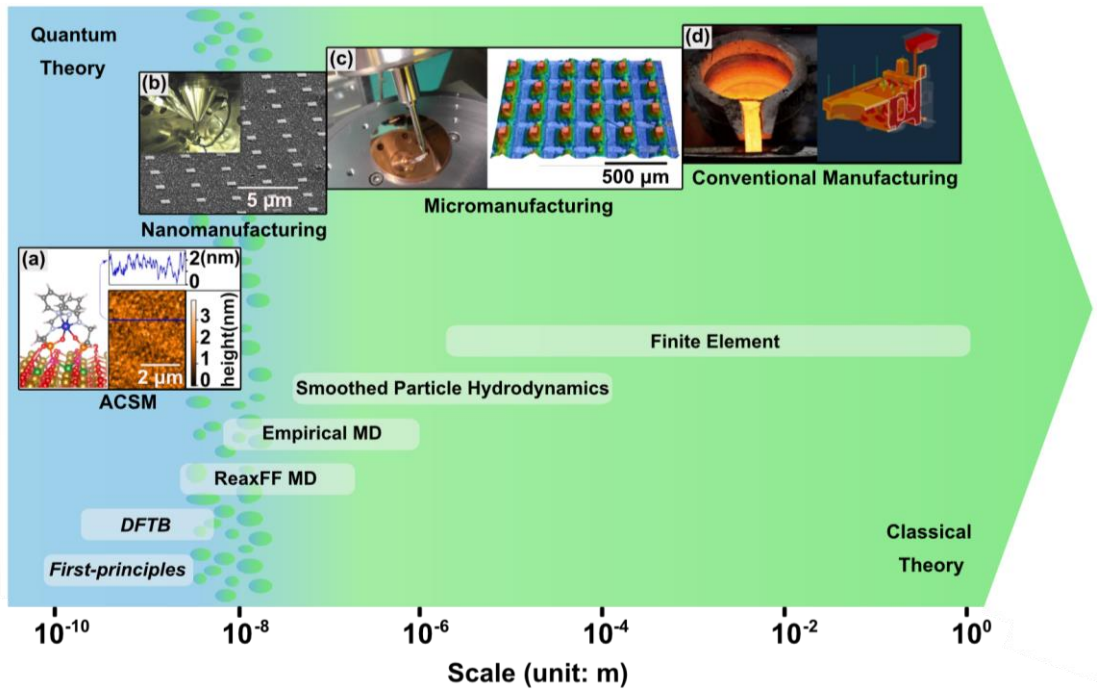

Figure 2-10. A length scale map of manufacturing systems, modelling methods, and dominant theories. (a) ACSM. Reprinted with permission from Ref [173]. CC BY 4.0. Copyright (2016) The Authors. (b) Nanomanufacturing. (c) Micromanufacturing. Reprinted with permission from Ref [174]. CC BY 4.0. Copyright (2017) The Authors. (d) Conventional manufacturing.

2.3.1 Manufacturing across atomic and macroscopic scales

As time and size scales continue to shrink, there should be a transition between macroscopic and atomic scales, beyond which classical theories become inaccurate in describing manufacturing behaviour. Instead, manufacturing below this scale is

dominated by quantum theory [9,170]. However, quantum theory and classical theory are completely different in nature. The transition from one to another is neither like a boundary nor a smooth gradience [171], but as a buffer where two theories cannot mix smoothly. Figure 2-10 summarises the manufacturing systems, modelling methods, and dominant theories across the length scales. It shows that atomic and close-to-atomic scale manufacturing (ACSM) is governed by quantum theory, while micromanufacturing and conventional manufacturing are governed by classical theory. In nanomanufacturing, when the length scale is below 10 nm, quantum effects start to become more apparent [172].

Classical theory has been widely used to describe conventional and micro manufacturing, and even some aspects of nanomanufacturing, as it typically yields the same analytical results as the quantum theory at these scales. Besides, classical theory is preferred due to its intuitive nature and lack of complex and difficult-to-solve quantum mechanical descriptions. Dominated by classical theory, traditional manufacturing processes are often deterministic, creating products in good consistency. However, further miniaturisation pushes contemporary manufacturing toward sub-10 nm or atomic scale, where both manufactured patterns and manufacturing tools may only involve a small number of atoms. At this scale, the phenomena, including chemical bond forming and breaking, electron excitation and ionisation, photochemical reaction, and particle and wave duality that related to quantum mechanics become apparent. These phenomena cannot be explained by classical theory unless resorting to the basics of quantum mechanics [170]. As a result, manufacturing at this scale will show non-classical features and unique phenomena, the explanation of which must be based on quantum mechanics. Therefore, the

fundamentals of interactions deserve to be understood and summarised in-depth, as they are critical for manufacturing at sub-10 nm and atomic scales.

As discussed in the previous section, the sub-10 nm or atomic scale manufacturing techniques, including SPM tip-based processes, ALE/ALD processes, and laser/electron/ion beam-based processes, rely on interatomic and energy beam-matter interactions. The fundamentals of these interactions will be introduced as follows.

2.3.2 Atomic interactions

For manufacturing processes, the interactions among atoms are the most important factors that affect the patterning accuracy, whether external energy sources are present or not. This is particularly true for SPM tip-based atom manipulation and chemical self-limiting processes, where the atomic interactions are the key factors that determine the processing results.

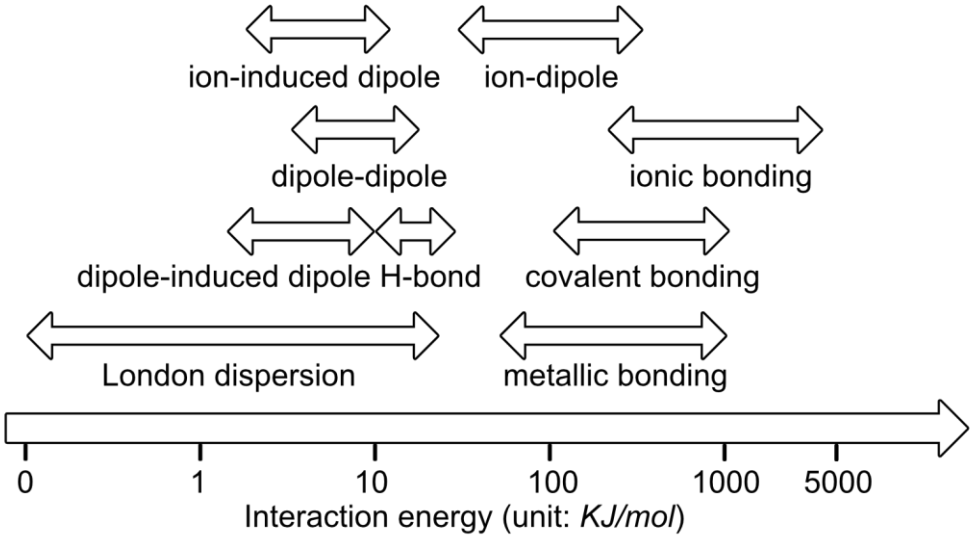

Figure 2-11. Comparison of the magnitude of different bonding mechanisms that bind atoms together. Data based on Ref [175].

Between atoms, the repulsive interaction mainly arises from Pauli repulsion; while the attractive interaction can be divided into intermolecular (non-bonding) interactions

(including ion-dipole and ion-induced dipole interactions, van der Waals interactions of dipole-dipole, dipole-induced dipole, and induced dipole-induced dipole interactions), and intramolecular (bonding) interactions (including ionic, covalent, and metallic bonding interactions). Their energies are collectively shown in Figure 2-11. These interactions can play important roles in generating atomic-scale patterns, and their quantum mechanical effects require a proper description.

2.3.2.1 Pauli repulsion

It is easy to understand that there are repulsive forces between two approaching atoms. For hydrogen molecules, the Coulomb force is the main source of the repulsion. However, this is a special case. For other atoms, the repulsive interaction is mainly caused by Pauli repulsion, which is a quantum mechanical phenomenon with no classical analogy. To explain the Pauli repulsion, let's imagine two helium atoms approaching each other until their electron orbitals start to overlap. Since the $1s$ shells of two helium atoms are already occupied by two electrons, the overlapping will confuse the energy states, leading to the emergence of two electrons with the same four quantum numbers in the same orbital. This state violates the Pauli exclusion principle, so electrons will divert to higher energy states to satisfy the rules. This process will cause a repulsive interaction. With the decrease of interatom distance, the repulsive 'force' ramps more quickly than the Coulomb force, which will dominate the source of repulsion in most circumstances.

2.3.2.2 Covalent bonding

Covalent bonds connect two atoms by sharing a pair or pairs of electrons. Due to the formation of a full electron shell, the energy of a shared state is lower than that of the separate atoms. Covalent bonds form in different types for different atoms, such as

sigma bonds, *pi* bonds, polar bonds, and complex hybridisations. In diamond, sp^3 hybridisation forms a very stable structure between carbon atoms with a binding energy of 7.3 eV [176]. When two atoms are identical or have similar electron affinities, the electron pair is shared equally, as in the molecules of hydrogen, nitrogen, and oxygen. However, if one atom shows a higher electronegativity than the other, the electron pairs will be closer to the more electronegative one and form a polar covalent bond. The polar covalent bond can give the molecule a polarized charge distribution, making it possible to form weak bonds with other polar molecules. Examples can be seen in water, sulphide, and hydrogen chloride. It is worthwhile to note that the above description only covers the general features of covalent bonds; a full explanation of covalent bonds must be based on the quantum mechanical description of electron pairs with the Schrödinger equation.

2.3.2.3 Ionic bonding

Ionic bonds form when complete electron transfer occurs between atoms, resulting in oppositely charged ions. According to the octet rule, metal atoms intend to lose their outermost electrons, while nonmetal atoms tend to accept them, both with the aim of achieving the noble gas configuration. When they meet, electrons will transfer from the metal atoms to the nonmetal ones. This results in the formation of ions, which can be bound together by electrostatic attraction. Since electrostatic attraction is isotropic, one ion can form multiple ionic bonds, which makes them very difficult to break. This explains the high hardness and melting points of ionic materials.

2.3.2.4 Metallic bonding

Metallic bonding theory argues that metals are a mixture of valence electrons and metal cations. These cations consist of nuclei and electrons in the inner shell. In metal, one

atom can contact many other atoms numerous other atoms, allowing for the sharing of valence electrons with neighbouring atoms. This sharing of electrons extends throughout the entire metallic solid, as nearby atoms continue to share their electrons with their own neighbouring atoms. Consequently, all valence electrons in the whole metallic solid are shared by all metal cations. Because only two electrons are allowed in an orbital, electrons will move freely among a large number of orbitals in metal. Since metallic bonds are isotropic, electron gases will attract metal cations as closely as possible, leading to a close-packed crystal structure. The properties of metals, including conductivity, thermal resistance, and strength, are all related to the nature of metallic bonding interactions.

2.3.2.5 Ion-dipole and ion-induced dipole forces

In addition to van der Waals forces, ion-dipole and ion-induced dipole forces are two important intermolecular interactions. Because ions carry a stronger charge compared to dipole moments, ion-dipole and ion-induced dipole interactions usually have stronger interaction energies than dipole-dipole and dipole-induced dipole interactions, as shown in Figure 2-11. Through electrostatic interactions, ions form non-bonding interactions with dipoles or induced dipoles. When a polar molecule and an ion are placed closely, their positions and orientations will be rearranged until the ion is next to the oppositely charged end of the dipole when the electrostatic attraction is at its maximum. As the dipoles are only slightly charged, the strength of the ion-dipole interactions is usually less than that of ionic bonding interactions. When an ion is placed near a non-polar molecule, the charge of the ion can temporarily induce an uneven distribution of electrons on the molecule. This temporary dipole could attract the ion and form a weak ion-induced dipole interaction.

2.3.2.6 Van der Waals forces

Van der Waals force is a distance-dependent interaction among atoms. Compared with chemical bonds in solids, van der Waals force forces are weak interactions and easily disturbed. This is the reason why gas hydrogen must be cooled down so much to become liquid or solid. Van der Waals forces are normally regarded as interactions that originate from the uneven or temporarily uneven distribution of electrons. Based on different types of involved particles, van der Waals forces include interactions of dipole-dipole, dipole-induced dipole, and induced dipole-induced dipole [177]. Coulomb's law can describe the first two interactions, which arise from electrostatic forces among polarized particles. Interactions between dipoles are normally weak, but when two dipoles, such as $O^{\delta-}$–$H^{\delta+}$, $N^{\delta-}$–$H^{\delta+}$, and $F^{\delta-}$–$H^{\delta+}$, meet, strong interactions can be formed, which can explain the H-bonds in some materials. The induced dipole-induced dipole interactions, also called London forces, which dominate the attractions between non-polar molecules, have a different mechanism. In fact, London forces will not exist if atoms are perfectly spherically symmetrical. However, Heisenberg's uncertainty principles determine the uncertain distribution of electron. In a short period, the charge distribution of atoms can be polar and induce the electrostatic attraction between atoms, implying the quantum mechanical nature of London forces.

2.3.3 Descriptions of atomic interactions

Figure 2-10 depicts the simulation approaches across length scales. Apparently, the first-principles method, which is based on quantum mechanical theory, dominates the simulation of manufacturing at sub-10 nm and atomic scale, while MD, smoothed particle hydrodynamics, and finite element simulation, which are based on classical theory, dominate the manufacturing from hundreds of nanometres to millimetres.

Between first-principles (or *ab initio*) and empirical MD simulation methods, there are two intermediate options, the DFTB method and the ReaxFF MD simulation method, which are capable of describing interactions at atomic and sub-10 nm scales.

2.3.3.1 Classical description

Classical physics uses Newton's second law to establish the relationship between force, position, and time. The state of a particle is governed by causality, i.e., given a certain condition, the state of a particle is predictable. The interaction between atoms can be described by potential functions. An example of Lennard-Jones (LJ) potential is shown in Figure 2-12. The curve expresses the function of interaction potential to the distance of two neutral or non-polar molecules. Considering van der Waals forces and the repulsion caused by the Pauli repulsion [178] and Coulomb force, an intermolecular pair Lennard-Jones potential is given as [179]:

$$U(r) = 4\varepsilon\left\{\left(\frac{\sigma\prime}{r}\right)^{12} - \left(\frac{\sigma\prime}{r}\right)^{6}\right\} \tag{2-3}$$

In the equation, σ' is the equilibrium separation, where $U(r) = 0$. Here, σ' is also called van der Waals radius. The minimum energy $-\varepsilon$ is at a distance of $r_e = 2^{1/6} \times \sigma'$.

In order to describe the interactions between atoms or molecules, various empirical potential energy functions can be used for different purposes. Some of these functions are suitable for bulk or surface properties, while others may be better suited for cluster and/or molecular properties. MD simulation based on these potential functions has been widely used in theoretical studies ranging from several nanometres to micrometres in manufacturing scales. However, this method is generally inadequate in accurately describing interactions at the atomic scale and sub-10 nm manufacturing

systems, where quantum mechanical effects such as covalent bonding, Pauli repulsion, and electronic transfer are more prominent. Therefore, a quantum mechanics-based method is required for the description of these interactions.

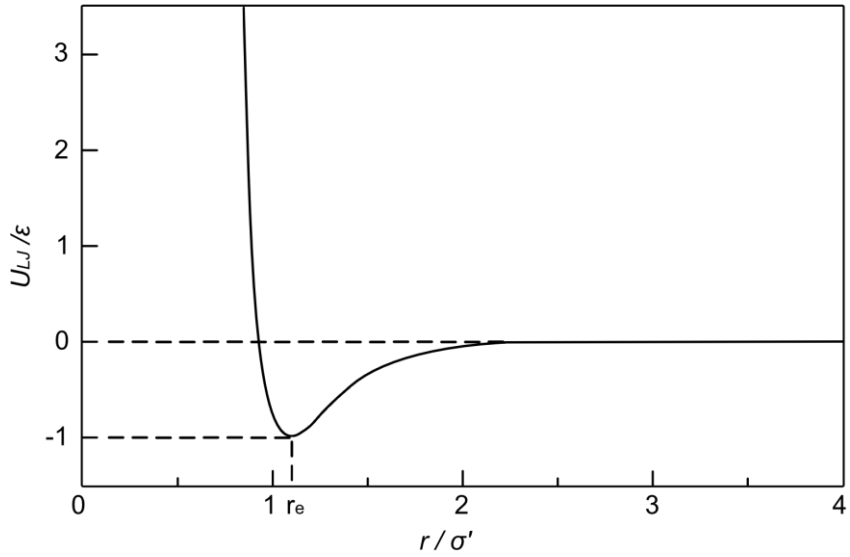

Figure 2-12. Particle interaction energy (U_{LJ}) as a function of interparticle distance (r).

2.3.3.2 Quantum mechanics description

To gain an understanding of the quantum mechanical description of interactions, it is necessary to first clarify the atomic model. In quantum mechanics, the location of the electron in an atom is expressed in terms of a probability distribution. It is determined by a wave function Ψ which describes the probability of finding an electron in an atom. The wave function is also called atomic orbitals. Depending on the type of atoms, atomic orbitals can look like a sphere, dumbbell, or clover. However, each orbital has its own specialty represented by a unique set of quantum numbers, i.e., principal quantum number n, angular quantum number l, and magnetic quantum number ml. As a fermion, the electron also has a spin angular momentum of $\frac{1}{2}\hbar$ or $-\frac{1}{2}\hbar$ in a given direction. This determines two consequences under quantum mechanics. First, each

orbital can only have two electrons, one has $\frac{1}{2}\hbar$ and the other has $-\frac{1}{2}\hbar$. This restriction is known as Pauli repulsion. In addition, electrons tend to occupy orbitals with the same spin before they pair up, following a principle called Hund's rules.

The vector of state Ψ is not directly related to any properties that are based on classical mechanics but is a complex function of selected state variables of coordinates and time, which can be described as $\Psi(\boldsymbol{r}, t_i)$. For instance, in solid bodies, the value $\Psi^2(\boldsymbol{r}, t_i)$ represents the electron probability density in a certain position at a certain time. To describe the evolution of the wave function over time t_i, the Schrödinger equation can be used, and the general equation can be expressed as [180]:

$$i\hbar \frac{\partial \Psi(\boldsymbol{r}, t_i)}{\partial t} = \hat{\mathrm{H}}(\boldsymbol{r}, t_i)\Psi(\boldsymbol{r}, t_i) \tag{2-4}$$

where i is the imaginary unity, and $\hbar$ is the reduced Planck's constant; $\hat{\mathrm{H}}(\boldsymbol{r}, t_i)$ is the Hamiltonian operator and represents the system's total energy, including kinetic and potential energy; it is also a Hermitian operator, and its eigenvalues are real. The role of $\hat{\mathrm{H}}(\boldsymbol{r}, t_i)$ in equation (2-2) is like the force in Newton's second law because it is determined by the physical system. The precise solution of the Schrödinger equation only exists for very simple models, like a hydrogen atom. However, but for more complex multi-electron systems, the inclusion of electron-electron interactions in the equation renders it mathematically intractable to find an exact solution.

First-principles methods can accurately describe the interactions for atomic-scale systems by calculating the electron structure at every time step [34]. In principle, the basic method is to solve the Schrödinger equations for nuclei and electrons in the whole system. To describe the interactions among particles, the first-principles

simulation usually applies a simpler form of the Schrödinger equation, which is the time-independent equation with the expression given as follow [180]:

$$\hat{\mathrm{H}}\Psi = E\Psi \tag{2-5}$$

E is the energy of the system. However, an intact system normally includes very complex interparticle interactions, which are impossible to solve. The calculation is usually based on a series of approximations, of which DFT is the most popular one used in computational physics, quantum chemistry, and materials science. DFT uses the functional, which is a real-valued function on functions, to determine the electronic energy. DFT considers that the electron wave functions, which yield the lowest total energy of the system, are the correct ones [181]. The Hamiltonians in DFT contain the electrons, electron-electron interactions, electron-ion interactions, and electron exchange and correlation energies. In general, the exact functionals of electron exchange and correlation are unknown, but there are approximation methods to assist this calculation, including local density approximation (LDA), generalized gradient approximation (GGA), meta-GGA, and hybrid functionals. Following the approximations, the DFT method can obtain the electronic structure of an atomic-scale system that yields the lowest energy.

2.3.3.3 DFTB method

DFTB is a semi-empirical method that is not as accurate as a first-principles method but can significantly reduce the computational cost. In the DFTB method, energy is still calculated by solving the Schrödinger equation for electrons, but the Hamiltonian matrix is not calculated by first-principles methods but parametrised based on DFT calculations or experimental results. Compared with the DFT calculation, the DFTB method reduces the computational cost by orders of magnitude while preserving the

quantum mechanical nature of chemical bonding, thus allowing the calculation for relatively large systems.

2.3.3.4 Reactive force field

ReaxFF is a reactive force field applied to MD simulation that can describe chemical reactions in addition to molecular interactions. To model chemical reactions (bonds breaking and forming), ReaxFF includes connection-dependent terms through a bond-order formalism (including both short-range and long-range interactions), where bond order is empirically calculated from interatomic distances, yielding a reactive force field. In addition, the ReaxFF parameters can be fitted and optimised against an extensive database of quantum mechanics calculations and experimental data. Altogether, ReaxFF allows the simulation of large-scale chemical reaction systems. Since the electronic interactions in chemical bonding are implicitly treated in ReaxFF methods, no explicit first-principles calculations are required, allowing for significantly improved computational efficiency compared to DFT or DFTB method. Although the incorporation of bond order makes ReaxFF almost two orders of magnitude more computationally expensive than simpler force fields, it can produce highly accurate results for many applications, including combustion, catalysis, and surface chemistry, at a fraction of the computational cost of first-principles methods [128].

Specifically, ReaxFF models many-body potential terms using semi-empirical parameters trained against a first-principles training set. The total interaction energy of a ReaxFF-described system is expressed through the following equation [182]:

$$E_{total} = E_{bond} + E_{val} + E_{tors} + E_{over} + E_{under} + E_{lp} + E_{H-bond} + E_{vdW} + E_{Coul} \quad (2\text{-}6)$$

where, E_{bond}, E_{val}, E_{tors}, E_{over}, E_{under} and E_{lp} correspond to the bond order energy, valence angle energy, torsion angle energy, over-coordination penalty energy, undercoordination penalty energy, and long-pair energy, respectively. These energy terms are based on the bond order (BO_{ij}) between two atoms i and j, which primarily depends on their interatomic distances and local chemical environment. BO_{ij} is typically calculated by [182]:

$$BO_{ij} = exp\left[p_{bo1}\left(r_{ij}/r_0^{\sigma}\right)^{p_{bo2}}\right] + exp\left[p_{bo3}\left(r_{ij}/r_0^{\pi}\right)^{p_{bo4}}\right] + exp\left[p_{bo5}\left(r_{ij}/r_0^{\pi\pi}\right)^{p_{bo6}}\right] \quad (2\text{-}7)$$

where r_{ij} is the interatom distance between atoms of i and j. Herein, semi-empirical parameters including p_{bo1}, p_{bo2}, r_0^{σ}, p_{bo3}, p_{bo4}, r_0^{π}, p_{bo5}, p_{bo6} and $r_0^{\pi\pi}$ are used for different bond types, including sigma bonds, π bonds, and double π bonds.

Non-bonding interactions are described through E_{vdW} and E_{Coul}, representing the van der Waals and Coulomb interactions between all atoms in the ReaxFF-described system. For a system with water, H-bonds were described using the term of E_{H-bond}. Each of the energy terms mentioned above corresponds to an analytic function whose parameters are determined through training against quantum chemical results. This approach ensures the accuracy of the chemical reactions and allows for the simulation of larger systems over longer time scales [128], demonstrating significant advantages over DFTB or DFT methods. A more detailed description of these energy terms can be found in Ref [183].

2.3.4 Energy beam-matter interactions and their descriptions

As reviewed in the previous section, photon, electron, and ion beams are popular manufacturing tools that provide external energy sources in nanomanufacturing. These processes involve different types of interactions. Compared with pure mechanical

tools, these energy beams can deliver a larger density of energy to physically and/or chemically interact with material surfaces, opening the possibility for processing strong bonding materials with high efficiency. The relevant nanomanufacturing processes include photolithography, EBL, FEBE/FEBD, and FIB lithography. Due to the weak penetration and scattering features of these energy beams in materials, the energy beam-matter interactions usually exist among a limited number of atoms or in several surface layers where atomic-scale effects become critical. As a result, quantum mechanics is also crucial in describing the interactions between energy beams and substrate atoms in energy beam-based nanomanufacturing processes.

2.3.4.1 Photo-matter interactions

Photo-matter interactions can lead to observable changes in both light and matter; either matter induces changes to light, such as phonon emission, absorption, and scattering, or light induces changes to matter, such as photochemical reaction, thermal effect, ionization, and momentum transfer. In fact, changes in both light and matter occur simultaneously, which complicates the processes.

Photo-matter interaction can be divided into absorption, transmission, and reflection. For non-transparent materials, light only interacts with a few layers of atoms on the surface. The absorption in these layers thus dominates the photo-matter interaction. Because of the electromagnetic feature of light, photo-matter interactions at the atomic or electronic scale are recognised as resonant interactions between oscillating electromagnetic fields and charged particles (normally electrons in atoms). To describe the time-dependent features in this process, a TD-DFT method is required to provide an unbiased view of photo-matter interactions. For example, the state of an electron in

a hydrogen atom can be described by the Schrödinger equation. Under the Coulomb interaction of the nucleus, the Hamiltonian is expressed as [184]:

$$\hat{\mathrm{H}}(\boldsymbol{r}, t_i) = \frac{1}{2m}\boldsymbol{p}^2 + V(\boldsymbol{r}) \tag{2-8}$$

where $V(\boldsymbol{r})$ is the Coulomb potential, m and $\boldsymbol{p}$ are the mass and momentum of the electron. If the electron meets a light beam, the interaction between the electron and the electromagnetic field needs to be added to the Hamiltonian. The electromagnetic field can be described by scalar potential $\Phi(\boldsymbol{r}, t_i)$ and vector potential $\boldsymbol{A_v}(\boldsymbol{r}, t_i)$, then the equation is shown as [184]:

$$\hat{\mathrm{H}}(\boldsymbol{r}, t_i) = \frac{1}{2m}\left(\boldsymbol{p} + e\boldsymbol{A_v}(\boldsymbol{r}, t_i)\right)^2 - e\Phi(\boldsymbol{r}, t_i) + V(\boldsymbol{r}) \tag{2-9}$$

as time evolves, the wave function will change, and the electron can escape from its eigenstate of the atom. Under the interaction with light, if the electron is in the bound state, then the electron may just be excited and return to the eigenstate after releasing energy; if the electron is in the continuous state, then the atom is ionized. Therefore, by solving the time-dependent Schrödinger equation, the probability that an atom is excited or ionized can be calculated. However, no analytical solution exists for this equation. Even with the help of a high-performance computer, numerical solutions could be calculated but only for some simple systems.

2.3.4.2 Electron-matter interactions

When an electron beam dwells on a material surface, transmitted electrons can behave differently, leading to various changes in the material. Some electrons pass through the material without experiencing any energy loss, becoming unscattered electrons. On the other hand, scattered electrons can be divided into two types: elastic scattering electrons and inelastic scattering electrons.

Elastic scattering electrons will interact with an atom without energy loss in total but may transfer energy and momentum to nuclei or electrons. If an electron beam impinges on an electron in an atom, the elastic scattering will create a secondary electron and ionize the atom; if on the nucleus, the momentum delivered may cause knock-on damage when electrons are accelerated by a high voltage. The energy delivered to an atom can be given as [185]:

$$\Delta E = \frac{2(E+2E_0)E}{Mc^2}\ sin^2\frac{\theta}{2} \tag{2-10}$$

where E is the kinetic energy of the electron, $E_0 = m_0c^2$, m_0 is the rest mass of the electron, M is the mass of the atom, θ is the scattering angle during the interaction. When ΔE is larger than the knock-on threshold, the atom will be moved out of its lattice site.

Inelastic scattering happens more frequently, which is associated with energy loss while passing through the substrate. This process can lead to the emission of X-rays, cathodoluminescence, secondary electrons, Auger electrons, and visible light. At the same time, the energy delivered may change the matter with the excitation (one of its electrons goes to an excited orbital) or ionization (one of its electrons leaves the atom and becomes the secondary electron) of the atom. If excitation or ionization occurs on the bonding atoms, the chemical bonds may break and lead to structural changes.

Fundamentally, the inelastic scattering depends on the energy of the incident electrons and the properties of materials, the description of which is rather complicated and requires the time-dependent Schrödinger equation. The expression for a simple two-body 1D electron-hydrogen system is as follow [186]:

$$i\hbar\frac{\partial\Psi(x_1,x_2,t)}{\partial t} = \hat{\mathrm{H}}(x_1,x_2)\Psi(x_1,x_2,t) \tag{2-11}$$

where x_1, x_2 are the positions of two electrons. The Hamiltonian of a two-electron system is expressed as [186]:

$$\hat{\mathrm{H}}(x_1, x_2) = -\frac{1}{2}\frac{\partial^2}{\partial {x_1}^2} - \frac{1}{2}\frac{\partial^2}{\partial {x_2}^2} + v_{ext}(x_1) + v_{ext}(x_2) + w_{ee}(x_1, x_2) \quad (2\text{-}12)$$

The Coulomb interactions between electrons and between electron and hydrogen nucleus (at x_H) are described by soft-Coulomb interactions [187]:

$$w_{ee}(x_1, x_2) = \frac{1}{\sqrt{(x_1 - x_2)^2 + 1}} \quad (2\text{-}13)$$

$$v_{ext}(x) = -\frac{1}{\sqrt{(x - x_H)^2 + 1}} \quad (2\text{-}14)$$

Through the numerical solution, the real inelastic scattering will be better understood, and energy transfer can be calculated.

2.3.4.3 Ion-matter interactions

As a beam of incident ions bombards the surface of a solid sample, complex physical phenomena occur at, above, and below the solid surface. Among these, the ion-solid scattering process is the most pronounced interaction. Fundamentally, the scattering processes include two types: elastic scattering and inelastic scattering. In elastic scattering, incident ions collide with atomic nuclei, transferring a portion of their kinetic energy to the target atoms. On the other hand, in inelastic scattering, incident ions interact with the electrons surrounding an atomic nucleus. These scatterings result in different by-products, consequently leading to different applications.

For elastic scattering, kinetic energy and momentum are conserved during the collision process. The energy transferred from the incident ion to the target particle can be described as [188]:

$$T_k = \frac{4m_1 m_2}{(m_1 + m_2)} E sin^2\left(\frac{\vartheta}{2}\right) \quad (2\text{-}15)$$

where m_1 and m_2 are the masses of the incident ion and the target particle, respectively; E and T_k are the kinetic energies of the incident ion and the target atom; ϑ is the scattering angle in the centre of the mass coordinate system. The relationship between the energy transfer ratio and mass ratio of the binary collision system is shown in Figure 2-13. It indicates that the main parameters that govern the energy transfer rate from the incident ion to the target particle depend on the mass ratio of the incident ion to the target particle (m_1/m_2) and the scattering angle. For surface atoms with a T greater than the surface binding energy, they will receive enough energy from the incident ions and escape from the sample surface, resulting in a void (or a structure that accumulates a lot of voids).

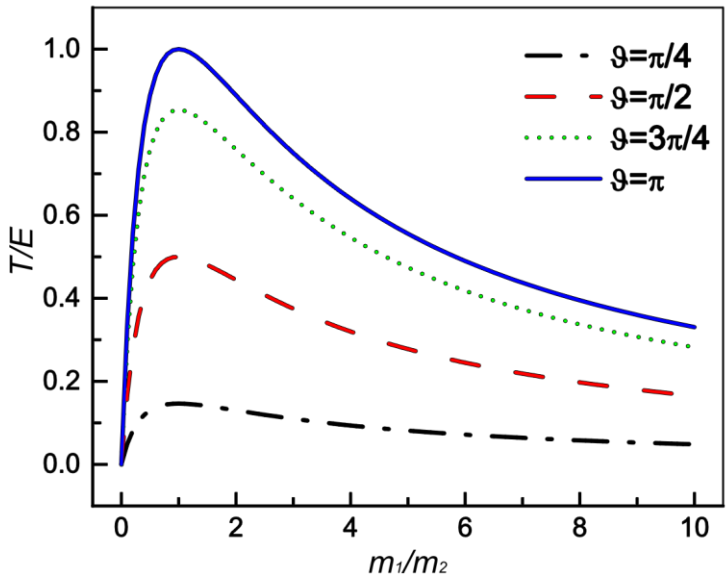

Figure 2-13. Kinetic energy transfer rate from the incident ions to the target particles in an elastic scattering process.

When an ion beam interacts with electrons in an atom, the kinetic energy could be transferred to electrons through elastic scattering or converted to other energies and absorbed by electrons or nuclei by inelastic scattering. Both processes can cause

excitation and ionization to incident and target atoms. After excitation, surface atoms can emit electrons, X-rays, and photons [189]. The inelastic process is more complicated compared with that in the electron-matter interaction because of the multiple particles and multi-step reactions involved.

2.4 Comparison and discussion

Table 2-1 shows the comparison of the aforementioned atomic scale and sub-10 nm manufacturing techniques. SPM tip-based atom manipulation has an atomic-scale patterning ability through angstrom-level control over the atomically sharp tips. The ALE and ALD depend on the chemical self-limiting characteristics of materials to obtain the etching or deposition with atomic layer resolution. LAO nanolithography can obtain sub-5 nm patterns through localising chemical reactions within a nanoscale cell through the use of probes with nanoscale-sharp tips and pulsed voltages with short widths. EUVL and focused electron/ion beam-based lithography can achieve the minimum feature sizes at around several nanometres when the energy beam-matter interaction region is well controlled; particularly, the STEM-based electron beam can serve as a special tool with abilities to operate atoms like SPM tip-based methods and realise the atom manipulation.

For AFM tip-based atom manipulation, ALE and ALD processes, the key mechanisms that determine the atomic-scale patterning ability are the atomic interactions, including chemical bonding, van der Waals forces, and Pauli repulsion. For the STM tip-based method and LAO nanolithography, the dominant interactions also involve the interaction with the tunnelling current or ions. The atomic interactions still play important roles in the energy beam-based processes, but the energy beam-matter interaction would directly determine the patterning resolution.

Table 2-1 Comparison of advanced manufacturing techniques with sub-10 nm and atomic resolutions.

Items	SPM tip-based Atom manipulation	ALE/ALD	LAO	Laser-based process	Focused electron/ion beam lithography
Minimum feature	Atomic	Atomic layer	4 nm [99]	Sub-10 nm [135]	Sub-5 nm [190]
Principle	Chemical bonding, van der Waals forces, Pauli repulsion, electronic excitations	Chemical bonding	Chemical bonding	Photochemical or photothermal reaction	Excitation, ionisation, knock-on damage
Simulation tools	DFT, DFTB, KMC [25,33,35]	DFT, ReaxFF MD, KMC [124,129,131]	ReaxFF MD [93]	TD-DFT [137]	DFT, TD-DFT, KMC [160,161,163,165]
Machining capability	-	-	2D, 3D	2D, 3D	2D, 3D
Environmental conditions	Ultra-high vacuum	Vacuum or inert gas	Ambient	High vacuum	Vacuum
Start-up cost ($)	100,000–100,000	35,000–100,000	25,000–100,000	>400,000,000 (EUVL)	>1,000,000

As manufacturing approaches sub-10 nm or atomic scale, physical challenges become increasingly significant compared to those encountered in micromanufacturing. A reliable modelling method is thus in demand to address these challenges. To reveal the underlying mechanisms at this scale, the simulation approaches need to resort to quantum mechanics-based simulation tools, which provide more reliable descriptions than the empirical simulation methods. The DFT/DFTB, TD-DFT, and ReaxFF MD methods are represented tools contributing to the mechanism study and process optimisation for different atomic scale and sub-10 nm manufacturing processes. Through descriptions of atomic structures, interaction energy, minimum energy path, and the possibility for atom transfer, the DFT/DFTB and ReaxFF MD methods can reveal the underlying mechanisms of SPM tip-based atom manipulation, LAO, ALE/ALD, and atomic interactions in energy beam-based processes. The TD-DFT methods can describe the time-dependent features of light-matter and particle beam-matter interactions. These methods provide an unbiased insight into light absorption, photochemical reactions, light excitations for light-based processes, and the electronic stopping and excitations for particle beam-based processes. This summary indicates that first-principles simulation has not only contributed to the understanding of atomic-scale interactions in nanomanufacturing processes but also assisted in materials selection, phenomena prediction, and experimental protocol. However, due to the limitation of current computational apparatuses, the first-principles methods, even for DFTB, are restricted to the number of atoms and time scale that can be employed in the simulation. As a result, this limitation has hampered their wide applications. For the TD-DFT method, the calculation provides a comprehensive description of the electronic and optical excitations, which means it is rather time-consuming. Simulating

all possible excitations of atomic transfer during an energy beam-based process remains beyond current capabilities. To conduct the simulation with larger scales in volume and time, the ReaxFF MD and KMC approaches are more suitable but require a reliable parameterisation to accurately reflect bonding interactions.

As for the 3D nanofabrication capabilities, LAO nanolithography can obtain flexible control of oxidation growth through adjusting tip-sample bias, multi-step oxidation, and hybrid approaches with a combination of oxidation and etching. Laser-based 3D nanolithography, on the other hand, may include multiple approaches, including laser direct-write lithography, two-photon polymerization, and two-photon-induced precipitation. Focused electron/ion beam lithography has also been reported in 3D nanofabrication, and the main approaches include EBL, FEBD, FEBE, FIB milling, and HIB induced deposition or modification. Detailed introduction of these laser-based and focused electron/ion beam-based 3D nanofabrication methods can be found in Ref [191,192].

The different nanolithography methods have various environmental requirements and start-up costs. SPM tip-based atom manipulation requires an ultra-high vacuum to isolate the environmental noise and high-resolution SPM facilities to detect the atomic forces. Laser-based or focused electron/ion beam-based processes normally require a vacuum environment, expensive optical or electro-magnetic system, high-quality motion stages, materials and accessories. For ALE and ALD, a typical equipment setup includes a closed chamber for gas handling, a vacuum system for controlling pressure, and a plasma source for generating reactive species. The start-up cost may vary, but normally less than the aforementioned processes. In contrast, LAO nanolithography can operate under ambient conditions and has normal performance requirements of the

AFM. This makes it a promising candidate for prototyping nanoproducts in the laboratory with lower start-up cost and environmental requirements in comparison with other 3D nanofabrication techniques.

2.5 Summary

This chapter provides a review of atomic scale and sub-10 nm manufacturing processes in terms of mechanisms, dominant interactions, and simulation research. The fundamentals of interactions in these manufacturing processes were summarised with a focus on atom-atom and energy beam-matter interactions based on underlying quantum mechanics. These processes were compared in terms of resolution, dominant interactions, simulation tools, machining capability, environmental requirement, and start-up cost.

The literature review suggests that a flexible, cost-effective, and efficient sub-10 nm 3D nanofabrication approach is still lacking, particularly for the in-lab prototyping of novel nanoproducts with small features and complex geometries. LAO nanolithography is a promising candidate to address this need due to its sub-10 nm resolution, low development cost, and environmental requirements. However, knowledge gaps exist in understanding the reaction process and modelling the oxidation growth with respect to control parameters. Challenges also persist in achieving flexible and deterministic control over oxidation growth, impeding further development. The following chapters in this thesis will focus on the theoretical simulation of the reaction mechanism and the development of a new 3D LAO nanolithography approach to address these challenges.

Chapter 3 Theoretical simulation study of LAO process

3.1 Introduction

LAO nanolithography relies on the controlled and localised bias-induced chemical reaction, which happens instantaneously and makes it difficult to observe in experiments. As concluded in Chapter 2, ReaxFF MD simulation has been identified as an ideal method to study the intricate reaction mechanism in chemical reaction-based manufacturing systems. Therefore, this chapter will employ this method to uncover the underlying mechanism of the LAO nanolithography processes. Despite previous attempts in ReaxFF MD simulation work to uncover the bias-induced oxidation process [93,94], it is worth noting that these simulations did not consider the existence of a surface passivation layer. The presence of the passivation layer is attributed to the boundary dangling bonds on the pure semiconductor surface, which has high reactivity, leading to the formation of a passivation layer as soon as it contacts with water. Moreover, the analysis of particles, bonds, and atomic charges was not entirely performed and might have failed to observe critical reaction phenomena in the LAO process. Therefore, a systematic and comprehensive analysis of the bias-induced oxidation is required to evaluate the physical-chemical reactions, which is currently a significant knowledge gap in the literature towards atomistic understanding of the LAO process.

This chapter will first introduce the method used for the simulation and then present the analysis of simulation results of surface passivation and bias-induced oxidation, aiming to reveal the true reaction mechanisms in LAO. Then, parametric studies will be performed to study the effects of different electric fields and humidity levels on bias-induced oxidation results and their influencing mechanisms.

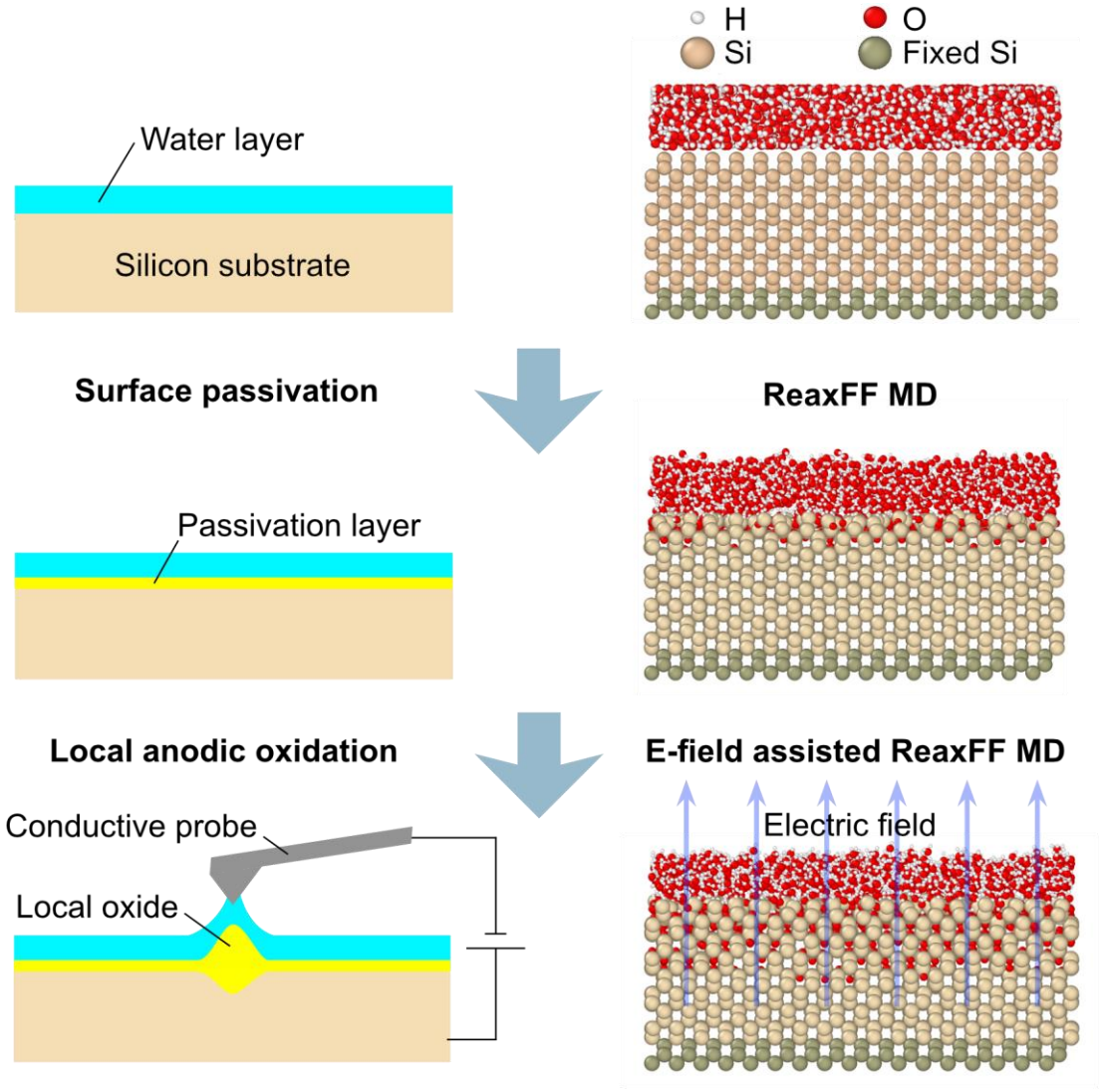

Figure 3-1. Simulation procedure for surface passivation and bias-induced oxidation.

3.2 Methods

3.2.1 Simulation procedure

In order to address the above-mentioned knowledge gaps, in this thesis, the water passivation and subsequent bias-induced oxidation processes of silicon (1 0 0) surface are investigated sequentially through ReaxFF MD simulation. Figure 3-1 shows the simulation procedure. Firstly, a passivation oxide layer on the silicon surface was created by the spontaneous reaction between silicon surfaces and water molecules

without the application of an electric field. Further, an electric field is introduced to simulate the subsequent bias-induced oxidation on the passivated silicon substrate, aiming to uncover the effect of a passivation layer on the oxidation process. To gain an in-depth understanding of the reaction process, a comprehensive analysis will be performed on the particles and bonds and their perspective roles through the processing of dump files generated during the simulation.

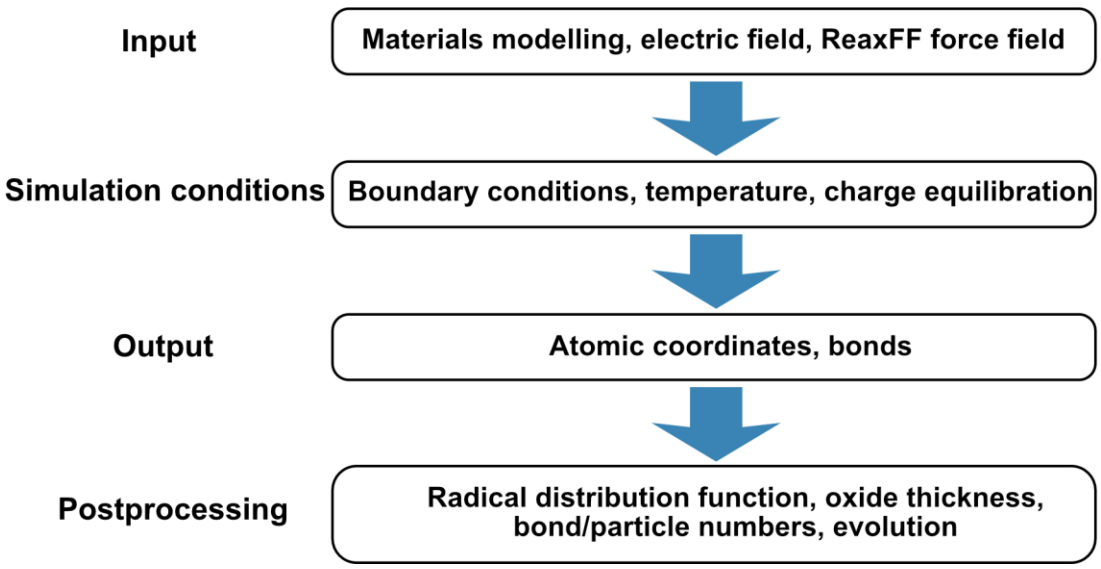

Figure 3-2. ReaxFF MD simulation process for surface passivation and bias-induced oxidation.

3.2.2 ReaxFF MD simulation setup

A detailed ReaxFF MD simulation setup is demonstrated in Figure 3-2. To simulate the surface passivation, the initial models of water and silicon substrate are first defined. This process can be achieved through Large-scale Atomic/Molecular Massively Parallel Simulator (LAMMPS) [193] for the crystalline silicon substrate and PACKMOL [194] for the randomly distributed water molecules. Their dimensions and positional relationship can be defined by adjusting input parameters. In this chapter, the initial silicon-water model was constructed with a silicon (1 0 0) substrate

and a water layer which has a density of 1g/cm^3 and consists of randomly distributed H_2O molecules. The silicon substrate has a size of 63.8305 × 63.8305 × 23.895 Å and the water layers have the same lateral dimension as silicon but with a thickness of 10 Å. Figure 3-3 shows the schematic of initial silicon-water models, in which silicon, hydrogen, and oxygen atoms are coloured with wheat, white, and red, accordingly. The lattice constant of silicon was set at 5.31 Å, which was proven to produce minimum energy in convergence simulation tests. To simulate the bias-induced oxidation, the initial model was prepared based on the passivation results with a passivated oxide layer on the silicon surface.

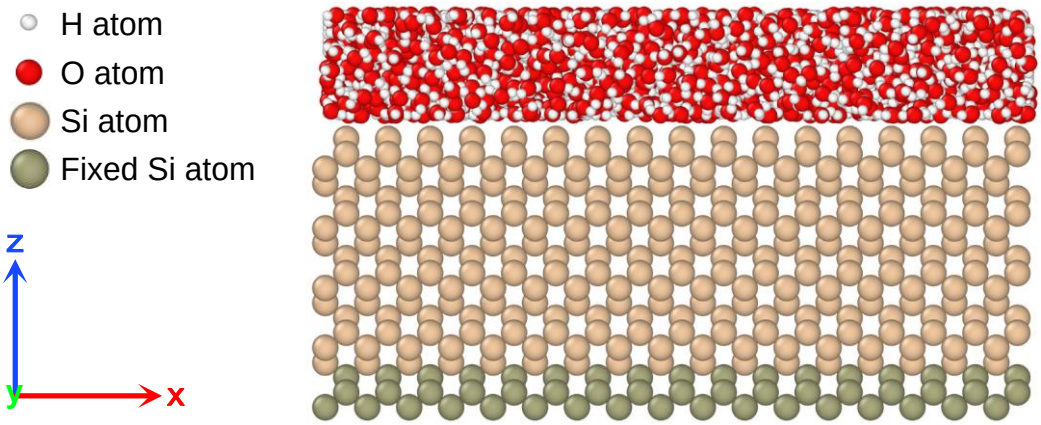

Figure 3-3. Side views of the silicon-water simulation model.

The interactions between atoms need to be defined by selecting proper force fields. This thesis chose the ReaxFF force field developed by Wen et al. [84], by combining Si/Ge/H force field [195] and water force field [196]. This force field has been extensively validated in previous studies of the water–silicon interactions [84], chemical mechanical polishing of silicon [197], and tribochemical wear at Si/SiO_2 interface in an aqueous environment [75]. In addition, the force field validation was also performed by Hasan [198]. He performed a validation by comparing the cohesive

energy and surface energy obtained from the ReaxFF MD simulation with those obtained from other potentials, DFT, and experiments. The results showed good agreements, which further confirms the reliability of the force field.

In the ReaxFF MD simulation, the charge equilibration (QEq) model was used to equilibrate the charge of simulation models at each time step [199]. The QEq model is an advantageous method for resolving challenges associated with excluding Coulomb interactions for dynamically bonded atoms so that the charge state for each atom depends on its environment. The model achieves this by incorporating finite atom sizes, which mitigate Coulomb interactions at short distances. Furthermore, the method applies short-distance shielding to the van der Waals term, similar to Coulomb interactions, providing a convenient solution [182].

To consider the influence of external electrical field in the simulations, this thesis used a modified LAMMPS code [193] proposed by Assowe et al. [79] through adding Coulomb energy in the ReaxFF potential. The modification was based on the formula proposed by Chen and Martinez [200], which takes into account atom polarisation, charge conservation, and electronegativity differences using the charge-fluctuation model. By integrating the electric field into the Coulomb energy, it becomes possible to calculate electrostatic properties, such as multipolar moments and polarizability.

For the geometric model, periodic boundary conditions were introduced in x and y directions to reduce the boundary effects. Along the z-axis, a fixed condition was applied with a reflective wall placed on the top of the water layer to prevent atom loss; the bottom three layers of atoms were fixed to prevent the overall movement, which facilitated further particle/bond distribution and trajectory analysis. The temperature

was set at 300 K, controlled by an NVT ensemble with a damping constant of 10 fs, and the Verlet algorithm was adopted to integrate the atom trajectories.

Finally, postprocessing was performed for the output files generated from the simulation, through which particle/bond type and number, atomic charge, and their distributions were counted and analysed using self-developed Python programs. The visualisation of simulation results was assisted with OVITO [201] and the Python Matplotlib library.

3.3 Results and discussions

Two simulation steps are introduced in this section to simulate the surface passivation and bias-induced oxidation processes. Specifically, the ReaxFF MD simulation was performed for the model in Figure 3-3 for 2000 ps, during which no electric field was applied during the initial 1000 ps, and then an electric field of 3.5 V/nm was applied from 1000 to 2000 ps.

3.3.1 Surface passivation

The MD simulation result at 1000 ps is shown in Figure 3-5 (a), which indicates the adsorption of a number of O and H atoms on the silicon surface, and the penetration of some O atoms into the silicon substrate. Together, they form a passivated oxide layer. In this work, the oxide film is defined as the region between the bottom oxygen atom and the top silicon atom along the *z* direction. To reveal the chemical composition and structure of the passivation layer, the partial radial distribution functions (RDF) of the oxide film are calculated and shown in Figure 3-4. The peak of the Si–H bond length is located at about 1.37 Å, which is close to the value of 1.48 Å reported in Ref [202]. Si–Si bonds have a peak length of 2.35 Å, and Si–O bond length shows two peaks at 1.58 and 2.25 Å, which agree with the experimental values well [203–206].

After that, several peaks of Si–O length appear between 3 to 7 Å, indicating amorphous structures within the oxide film.

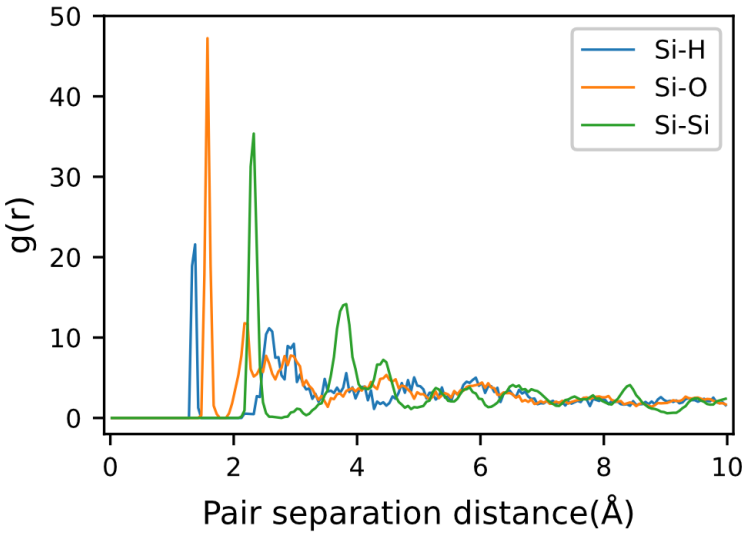

Figure 3-4. RDF curves for Si–H, Si–O, and Si–Si in oxide film created by surface passivation.

A combined analysis of simulation results in Figure 3-5 (a) and their RDF in Figure 3-4 shows that new bonds and particles including Si–O–H, Si–H, Si–H_2, H_2O–Si, Si–O–Si, and H_3O^+ (hydronium) were created during the surface passivation process. The distribution of these bonds/particles was summed based on the bond lengths in Figure 3-4 and plotted in Figure 3-5 (b). The passivated silicon surface was found to be a mixture of Si–O–Si, Si–O–H, Si–H, Si–H_2, and H_2O–Si bonds, which is consistent with experimental findings [207–209]. The numbers of these bonds show that the silicon surface is dominated by H-termination (Si–H or Si–H_2 bonds), which is responsible for the surface hydrophobicity observed in the experiment [210]. Si–O–Si bonds exist throughout the oxide film and determine the oxide depth. In addition, the

resultant water layer contains a large amount of H_3O^+, which, together with the remaining H_2O, forms the resultant water layer.

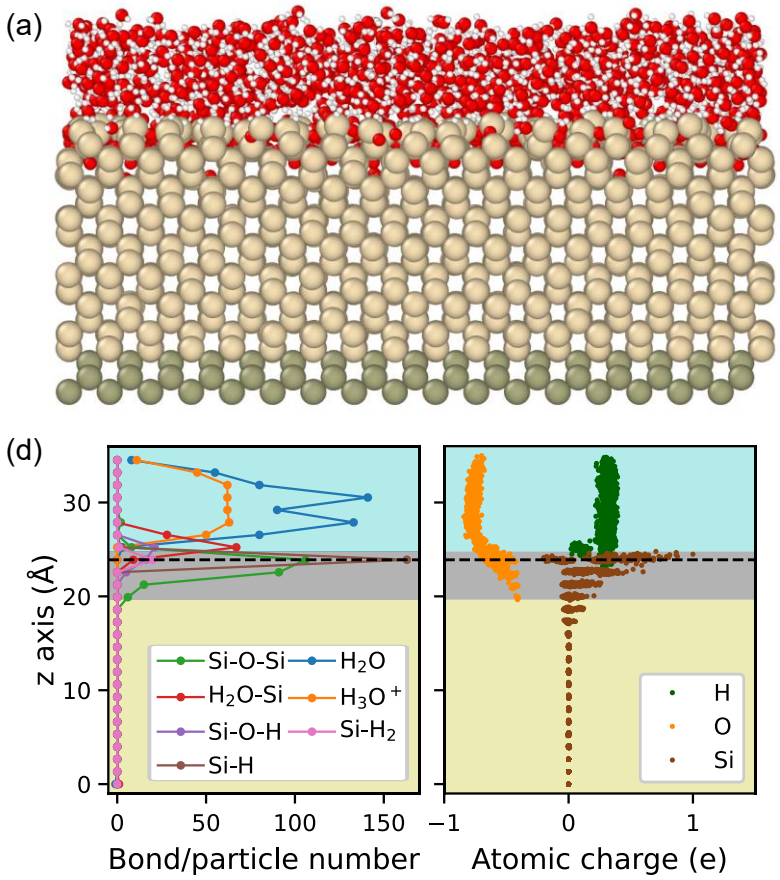

Figure 3-5. Simulation results for surface passivation. (a) Side view. (b) Distribution of bond/particle numbers and atomic charges along the *z*-axis, in which shaded regions coloured with wheat, grey, and cyan represent silicon, oxide layer, and water, respectively. The horizontal dashed line indicates the first atom layer in the initial model.

Figure 3-5 (b) shows the charge distribution of H, O, and Si atoms in the passivation result. O and Si atoms in the oxide film occupy different amounts of charge in comparison to these in water and silicon substrates. In the water film and silicon, O and Si atoms show -0.77 and 0 e, respectively. However, oxidised silicon shows a

positive charge, and the maximum value appears at 1.1 e at the silicon-water interface. This indicates the occurrence of charge transfer between O and Si atoms during the creation of the oxide layer, providing further evidence for the occurrence of an oxidation process. In addition, O atoms in the oxide film have less charge than that in water, ranging from -0.71 to -0.42 e, which is due to the different polarities in Si–O and H–O bonds.

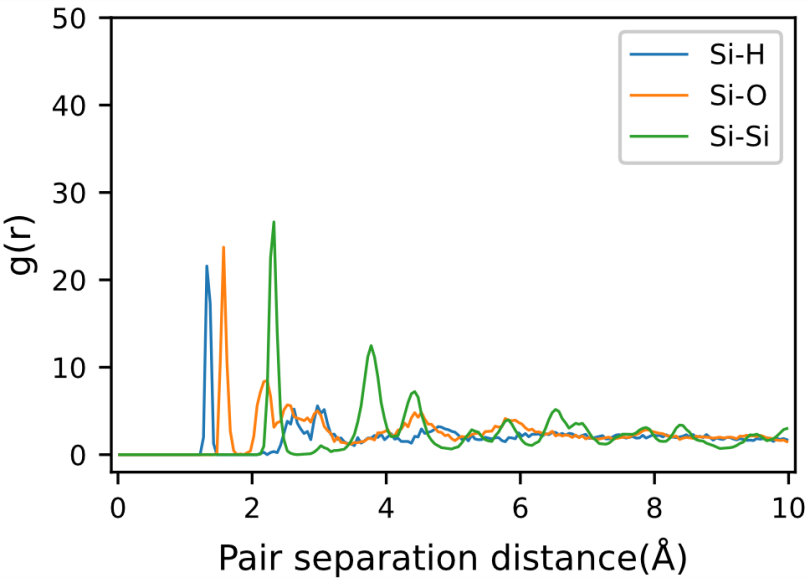

Figure 3-6. RDF curves for Si–H, Si–O, and Si–Si in oxide film created by bias-induced oxidation.

3.3.2 Bias-induced oxidation

The ReaxFF simulation result at 2000 ps is shown in Figure 3-7 (a). Apparently, more O atoms penetrated the silicon surface, resulting in an increased oxide thickness. Similarly, the RDF of the oxide film is plotted in Figure 3-6, and the bonds/particles distribution in the oxide film is plotted in Figure 3-7 (b). Through the comparison with passivation results in Figure 3-4 and Figure 3-5 (b), good similarities were found in both RDF of the oxide film and bonds/particles distribution at the oxidised silicon

surface. This demonstrates the application of the electric field did not apparently modify the chemical structures within the oxide film and surface composition, while leading to the generation of more Si–O–Si bonds under the oxide surface and the increase of oxide thickness.

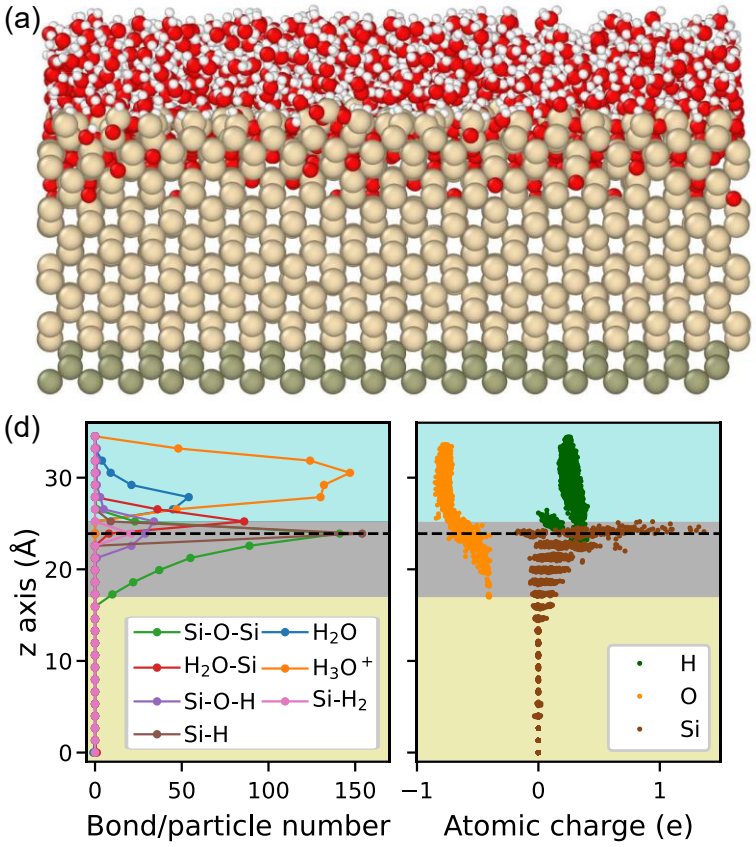

Figure 3-7. Bias-induced oxidation result. (a) Side view. (b) Distribution of bond/particle numbers and atomic charges along the *z*-axis, in which shaded regions coloured with wheat, grey, and cyan represent silicon, oxide layer, and water, respectively. The horizontal dashed line represents the first atomic layer in the initial model.

In addition, Si–O–Si bonds are found to be mostly concentrated near the surface, and their number gradually decreases layer by layer throughout the oxide film. The atomic

charge distribution in Figure 3-7 (b) shows that the application of an electric field increased the degree of oxidation on the silicon substrate, evidenced by more electropositive Si atoms in the results. Despite the increased O atoms near the surface, a number of Si atoms within the oxide layer remain unoxidized, as indicated by the Si atoms with nearly 0 charge in Figure 3-7 (b). This clearly indicates a mixture of Si and SiO_2 within the oxide film. Overall, the oxide film is found with a complex chemical structure consisting of amorphous SiO_2, adsorbed water, silicon, and silicon hydrates, which is consistent with previous simulations and experimental results [64,75].

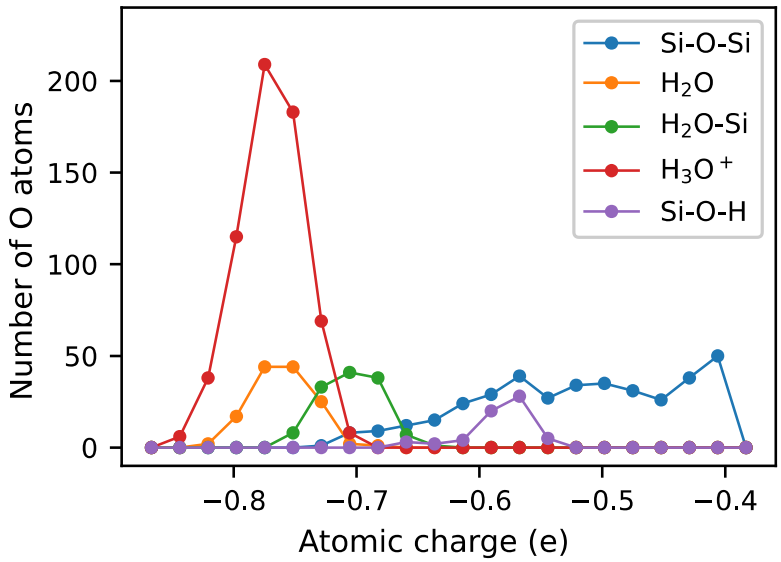

Figure 3-8. Distribution of bond/particle number at different atomic charges.

From the atomic charge distribution in Figure 3-7 (b), the application of an electric field enhances the oxidation on the silicon substrate, evidenced by the increased number of O atoms in the silicon substrate and more Si atoms with electropositive charges. To reveal the atomic charges of O atoms in different bonds/particles, the distribution of bond/particle numbers at different atomic charges is plotted in Figure 3-8. Apparently, O atoms in H_2O–Si and Si–O–H at the surface occupy different

atomic charges with peaks at -0.52 and -0.61, respectively. O atoms in Si–O–Si bonds occupy charges ranging from -0.68 to -0.37 e. These results indicate that the amount of charge transfer from the O atom varies depending on the specific bond types formed during the passivation process. Typically, the amount of charge transfer of O atoms in H_2O–Si is lower than that in Si–O–H. As for O atoms in Si–O–Si, the atomic charge varies depending on its *z*-axis position and neighbour charge states, as shown in Figure 3-7 (b).

3.3.3 Reaction process

To reveal the in-process details during surface passivation and bias-induced oxidation, the evolution of the number of bonds/particles and oxide thickness is depicted in Figure 3-9, which were counted based on dump files created every 10 ps. In the passivation stage, water was consumed and turned into oxide, represented by a reduced number of H_2O and increased numbers of Si–O–H and Si–O–Si bonds. In addition, hydrogen atoms from water decomposition were either attached to surface silicon atoms and formed Si–H/Si–H_2 bonds or combined with water molecules and formed H_3O^+. The evolution curves show that water reacted with silicon rapidly at the beginning of the simulation. A majority of Si–O–H, Si–H, Si–H_2, and H_2O–Si bonds were created in the first 40 ps and maintained at almost constant amounts in the following reaction up to 1000 ps. From 40 to 1000 ps, the oxide thickness increased from 4 to 5.1 Å. Simultaneously, there was a gradual consumption of H_2O, leading to the formation of more Si–O–Si bonds and H_3O^+, but at a relatively slow rate.

In the bias-induced oxidation stage, an electric field of 3.5 V/nm was applied during 1000–2000 ps. The evolution curves in Figure 3-9 show the amounts of Si–O–H, Si–H, Si–H_2, and H_2O–Si have not changed significantly, which further demonstrates that

the action of the electric field did not apparently modify the surface composition. However, from 1000 to 2000 ps, the oxide thickness increased from 5.1 to 8.2 Å, the number of H_2O decreased by 472, and the numbers of Si–O–Si and H_3O^+ increased by 149 and 282. The number changes of H_2O, Si–O–Si, and H_3O^+ roughly follow 3: 1: 2. Since the numbers of other bonds/particles did not vary significantly during the reaction, this suggests the bias-induced oxidation mainly induced the following reaction:

$$(\mathrm{Si-Si}) + 3\,\mathrm{H_2O} \xrightarrow{\text{bias}} (\mathrm{Si-O-Si})^{2-} + 2\,\mathrm{H_3O^+} \qquad (3\text{-}1)$$

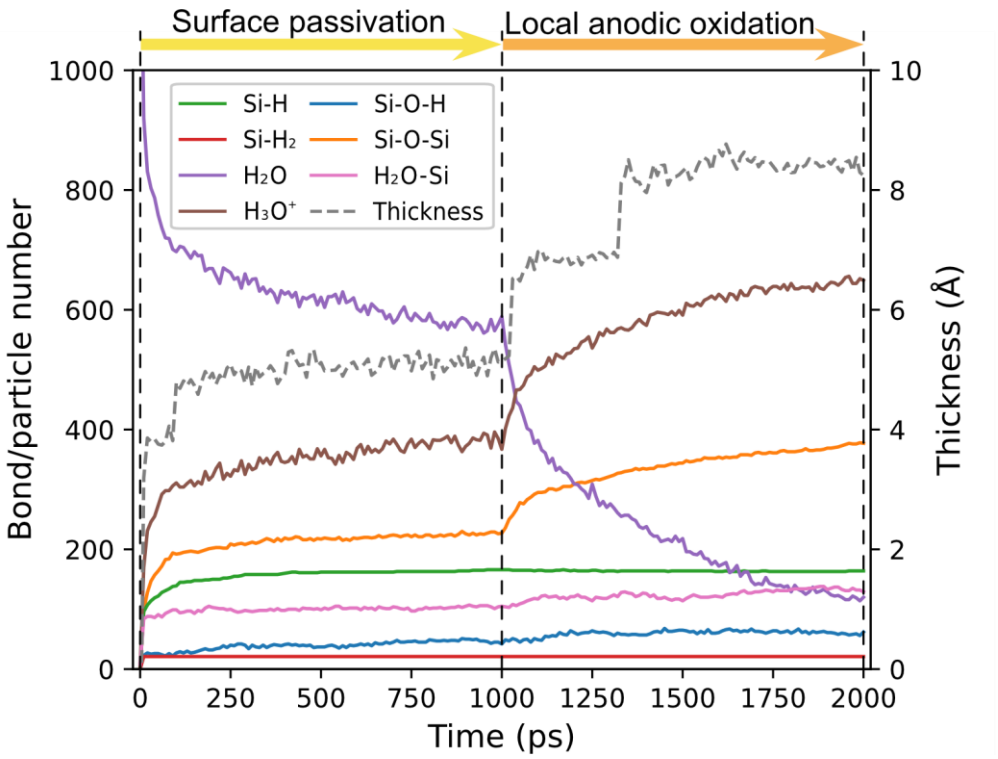

Figure 3-9. Time evolution of oxide thickness and bond/particle number during the reaction between silicon (1 0 0) substrate and a 10 Å thick layer of water. Surface passivation: 0–1000 ps; LAO: 1000–2000 ps.

To uncover the reaction process, this work tracked all the O atoms in Si–O–Si, Si–O–H, H_2O–Si, and H_2O/H_3O^+ at 2000 ps, and summarised the bonds/particles they belong

to at 1000 ps, the results of which are shown in Figure 3-10. O atoms in Si–O–Si may come from all the bonds/particles that have O atoms. The number of Si–O–Si bonds at 1000 ps (see Figure 3-9) indicates all the O atoms in Si–O–Si at 1000 ps remained within the Si–O–Si bonds in the bias-induced oxidation process. In addition, O atoms in Si–O–H only come from Si–O–H, H_2O–Si, and H_2O/H_3O^+; and O atoms in H_2O–Si only come from H_2O–Si and H_2O/H_3O^+. On the basis of the above findings, it appears that Si–O–H and H_2O–Si act as intermediate products at the surface during bias-induced oxidation.

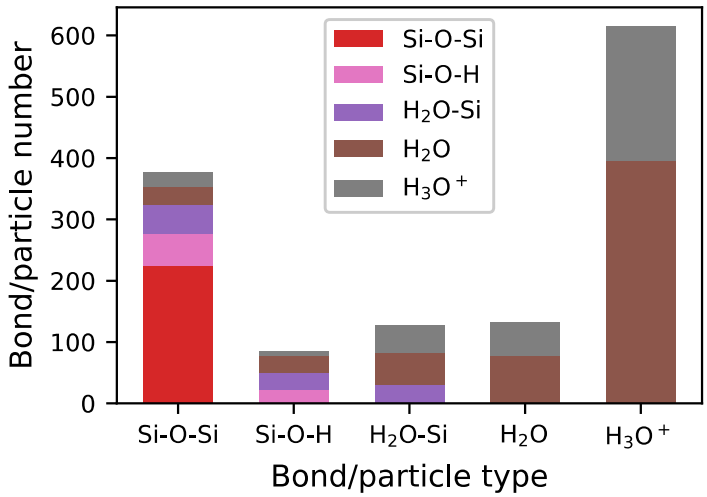

Figure 3-10. Bar chart showing the bond/particle number of Si–O–Si, Si–O–H, H_2O–Si, H_2O, and H_3O^+ of simulation result at 2000 ps. The bars are colour-coded to represent O atoms in each bond/particle type at 1000 ps.

Specifically, three reactions during the bias-induced oxidation were demonstrated. First, H_2O adsorbed to the silicon surface, forming an H_2O–Si bond (molecular adsorption):

$$Si + H_2O \rightarrow H_2O - Si \tag{3-2}$$

Next, the H_2O–Si bond dissolved into Si–O–H bond, and the released H atom combined with H_2O to form H_3O^+:

$$H_2O - Si + H_2O \rightarrow Si - O - H + H_3O^+ \quad (3\text{-}3)$$

Then, Si–O–H reacted with one of the surrounding Si atoms to form a Si–O–Si bond, and the released H atom combined with H_2O again to form H_3O^+:

$$Si + Si - O - H + H_2O \rightarrow Si - O - Si + H_3O^+ \quad (3\text{-}4)$$

Therefore, H_2O molecules were consumed step by step and eventually formed the Si–O–Si bonds. However, these results did not suggest any O atoms moving from Si–O–Si to Si–O–H and then to H_2O–Si, indicating that the reaction cannot proceed in the reverse direction.

3.4 Effect of electric field strength

3.4.1 Method

The dependence of different electric field strengths on bias-induced oxidation was examined through eight simulation groups. Each group utilised the same initial model containing a passivated layer on the surface as depicted in Figure 3-5 (a) but applied different electric fields with varying strengths ranging from 0 to 7 V/nm. In the first group of simulations, no electric field was applied to demonstrate the effect of ongoing surface passivation. Similarly, a thorough analysis of bonds/particles will be performed on the simulation results, aiming to reveal the influencing mechanisms.

3.4.2 Analysis of simulation results

After simulating the bias-induced oxidation for 1000 ps, the results in all groups are shown in Figure 3-11, which indicate a noticeable increase in the penetration of O atoms into the silicon substrate when using electric fields with higher strengths.

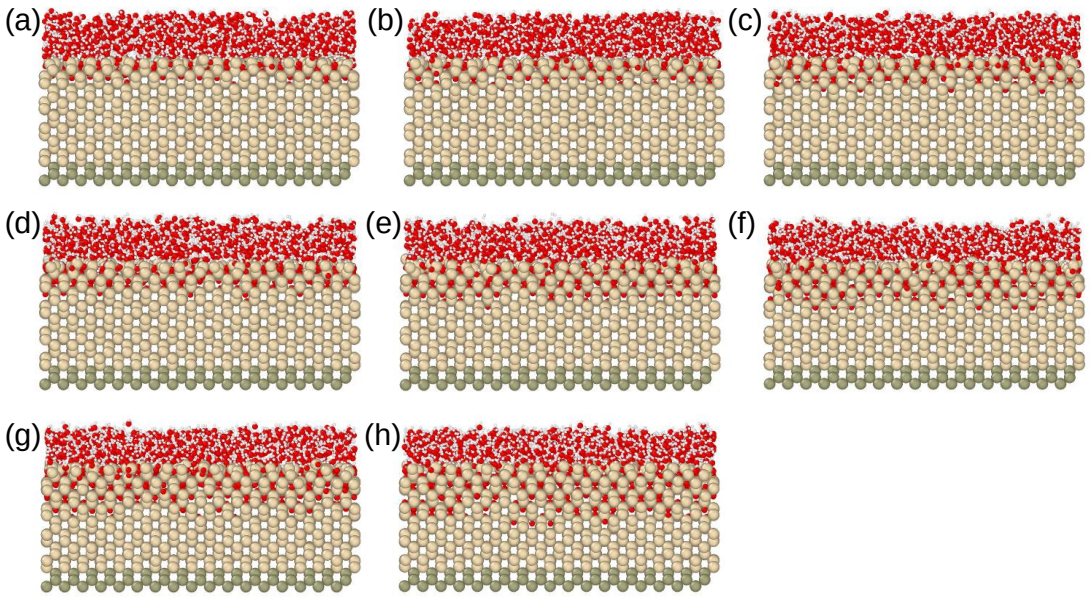

Figure 3-11. Sides views of simulation results with the application of electric fields with the strengths of (a) 0, (b) 1, (c) 2, (d) 3, (e) 4, (f) 5, (g) 6, and (h) 7 V/nm.

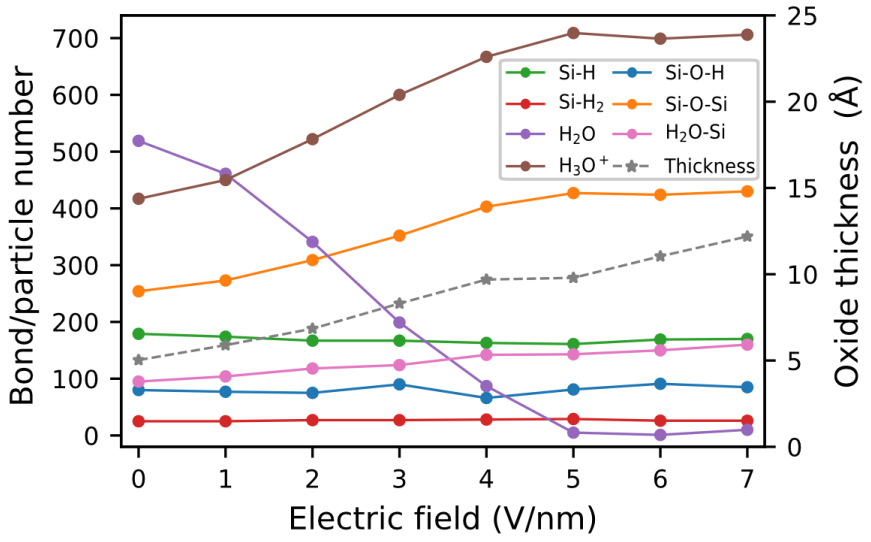

Figure 3-12. The numbers of particles/bonds and oxide thickness of simulation results at different electric fields.

Figure 3-12 illustrates the number of bonds/particles in simulation results to determine the influence of different electric fields on the chemical composition. Similar to the

conclusion in Section 3.3.2, the numbers of surface bonds, including Si–O–H, H_2O–Si, Si–H, and Si–H_2, were not drastically affected by different electric fields, while the consumption of H_2O and the creation of Si–O–Si bonds and H_3O^+ were apparently enhanced, particularly when the electric field increased from 0 to 5 V/nm. Through a calculation of the number changes of H_2O, H_3O^+, and Si–O–Si during each simulation group, it was found they also approximately follow 3: 2: 1, as demonstrated in Table 3-1. These results further prove that the reaction (3-1) dominates the bias-induced oxidation.

Table 3-1. The ratio of number changes of H_2O, H_3O^+, and Si–O–Si during the simulation processes of bias-induced oxidation at different electric fields

Electric field strength (V/nm)	Ratio of number changes of H_2O, H_3O^+, and Si–O–Si
0	2.6: 1.9: 1
1	2.8: 1.8: 1
2	3.0: 1.9: 1
3	3.1: 1.9: 1
4	2.9: 1.7: 1
5	2.9: 1.7: 1
6	3.0: 1.7: 1
7	2.9: 1.7: 1

Figure 3-13 plots the distributions of the number of Si–O–Si bonds along the *z*-axis for the simulation results. It can be observed that an increase in the electric field strength results in more Si–O–Si bonds being formed at deeper positions, indicating that more O atoms in Si–O–Si diffused below the surface under the enhanced electric

field strength. However, a significant percentage of Si–O–Si bonds still exists at the silicon-water interface.

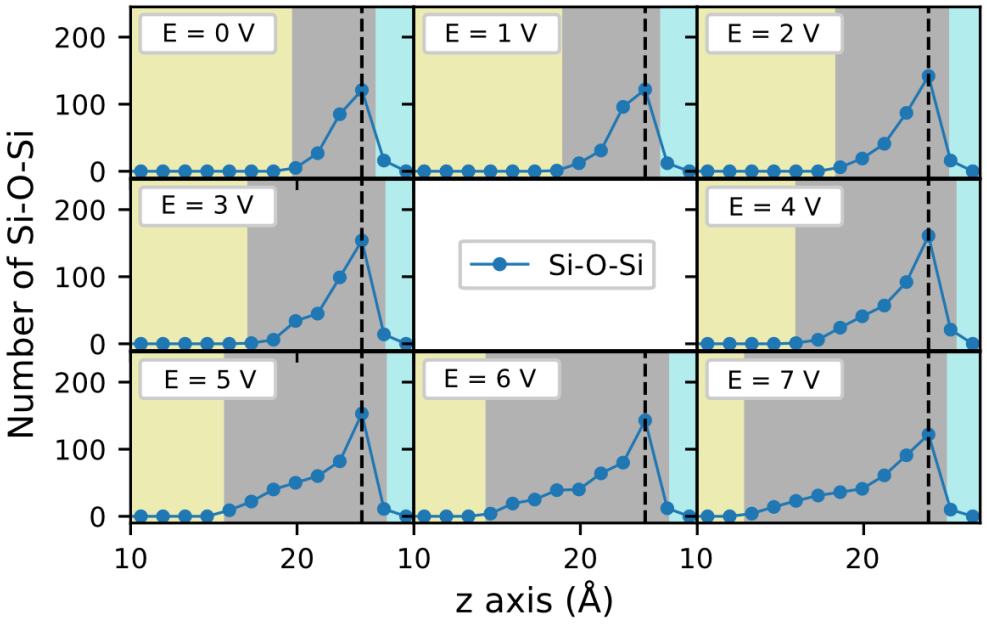

Figure 3-13. Distributions of the numbers of Si–O–Si bonds along the *z*-axis for simulation results at different electric fields with the strength ranging from 0–7 V/nm.

3.4.3 Analysis of the reaction process

To reveal the details of the reaction process, the evolution of the number of Si–O–Si bonds and H_2O in the water layer was calculated and depicted in Figure 3-15 (a) and (b). These curves suggest that the rate of reaction (3-1) increased with increasing electric field strength, as the enhanced electric field clearly accelerated the production rate of Si–O–Si bonds and consumption rate of H_2O, particularly in the first 100 ps. In addition, the reaction rate was found to be correlated with the amount of H_2O in the water layer, as indicated by the reduced generation rate of Si–O–Si at a decreased amount of H_2O remaining in the water layer. According to the simulation results shown in Figure 3-12, the numbers of Si–O–Si bonds reached approximately 430 at electric fields higher than 5 V/nm and did not increase further. In addition, Figure 3-13 further

indicates that the reaction ceased when the H_2O in the reaction system was nearly depleted. In the actual LAO experiments, water depletion should be more difficult to occur than that in the simulation with limited length scales. This is due to the presence of water on the tool and substrate surfaces and in the atmosphere, which allows for the continuous diffusion of water molecules to replenish any depletion during the LAO process. As a result, the oxidation can continue, with its reaction rate and duration determined by the diffusion rate of water [69].

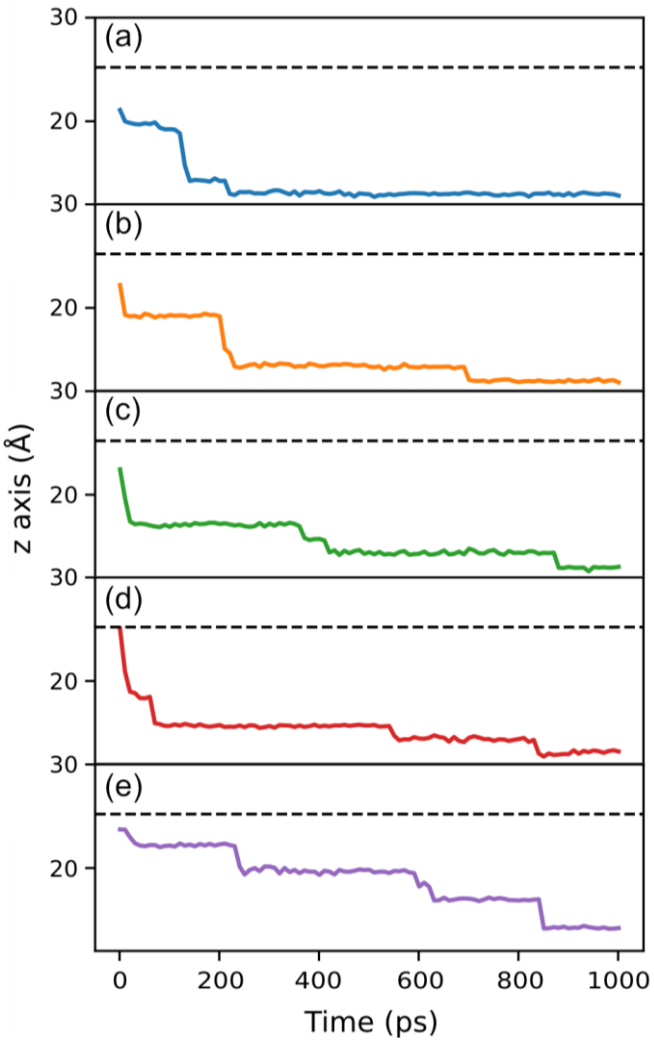

Figure 3-14. The evolution of *z* positions of the bottom five O atoms (a–e) in the oxide film in Figure 3-11 (h). The horizontal dashed line represents the surface atomic layer in the initial model.

As the strength of electric field exceeds 5 V/nm, the oxide thickness increases by one layer of silicon atoms even in the absence of an increase in the number of Si–O–Si bonds. Figure 3-14 depicts the evolution of the *z* positions of 5 bottom O atoms in Figure 3-11 (h). Between 300 to 1000 ps, no additional Si–O–Si bonds were created, as demonstrated in Figure 3-12 (c), but the existing negatively charged O atoms in Si–O–Si were found to diffuse into the silicon substrate in response to the electric field, which is similar to the interface diffusion mechanism between silicon and silicon dioxide as observed in the experiment [211]. This indicates that electric field-induced directional movement of O atoms can contribute to the oxidation growth, which, together with reaction (4-1), constitutes the oxidation growth mechanism in the bias-induced oxidation process. Therefore, it can be concluded that the electric field can induce the diffusion O atoms in Si–O–Si bonds below the surface. As a result, assisting the formation of more Si–O–Si bonds by creating more vacancies on the surface.

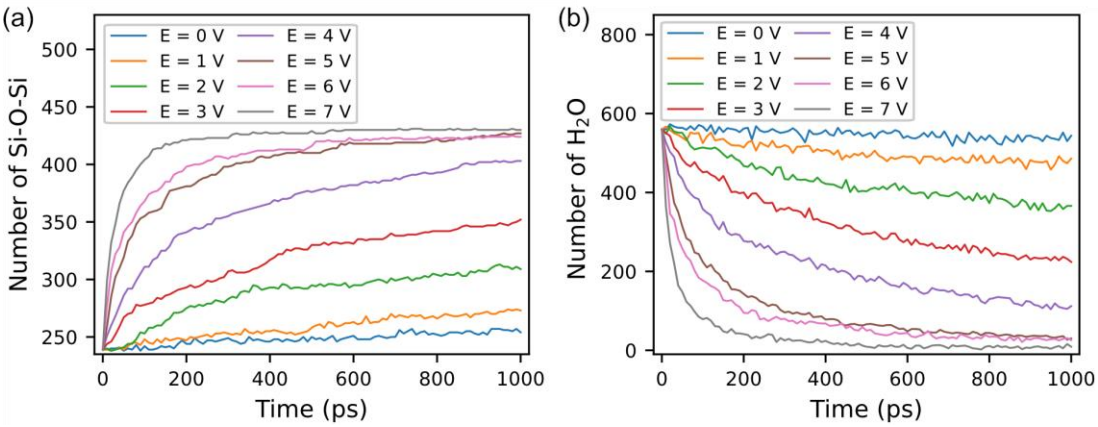

Figure 3-15. Evolution of (a) Si–O–Si bonds and (b) H_2O at electric fields with strength ranging from 0–7 V/nm during the LAO process.

As for the evolution of oxide thickness, Figure 3-12 indicates that the oxide thickness of the simulation results increased in a linear-like fashion with respect to the electric

field strength, and Figure 3-16 demonstrates that the oxide thickness increased layer by layer during the progression in each group of simulation. Both findings are consistent with results in previous experimental and simulation research [94,103,212].

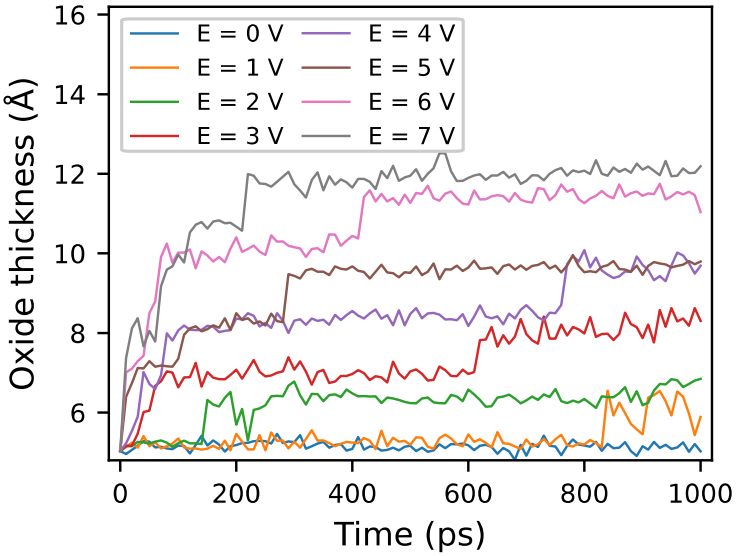

Figure 3-16. Evolution of oxide thickness at electric fields with strength ranging from 0–7 V/nm.

3.5 Effect of humidity

3.5.1 Method

To study the effect of humidity on surface passivation and electric field induced oxidation, the silicon-water reactions were simulated under different relative humidity levels. Asay and Kim [213] investigated the surface adsorption of water and established a correlation between the thickness of water layers and relative humidity (RH), as depicted in Figure 3-17. Based on this relationship, initial models with varying water layer thicknesses were constructed, as shown in Figure 3-18 (a–d), to qualitatively express reaction models at different humidity levels. Specifically, water layer thicknesses at 7, 10, 13, and 17 Å correspond to relative humidity levels of approximately 20%, 40%, 70%, and 90%, respectively. The initial silicon-water model

was constructed with the same silicon (1 0 0) substrate as in previous sections and a water layer that has a density of 1g/cm^3 and consists of randomly distributed H_2O molecules. Similar to previous simulation settings, an electric field (4 V/nm) was only applied from 1000 to 2000 ps.

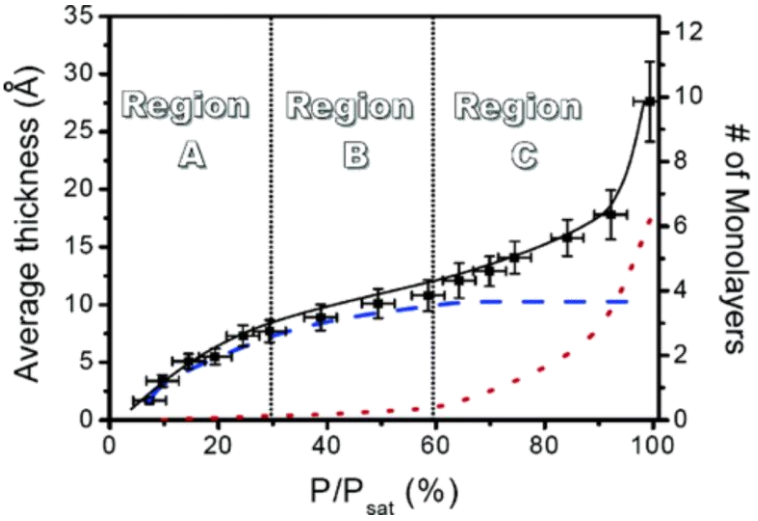

Figure 3-17. Adsorption isotherm of adsorbed water on the silicon oxide surface. Square symbols are the total thickness of the adsorbed water layer calculated from the intensity of the H–O–H bending vibration peak. Reprinted with permission from Ref [213]. Copyright (2005) American Chemical Society.

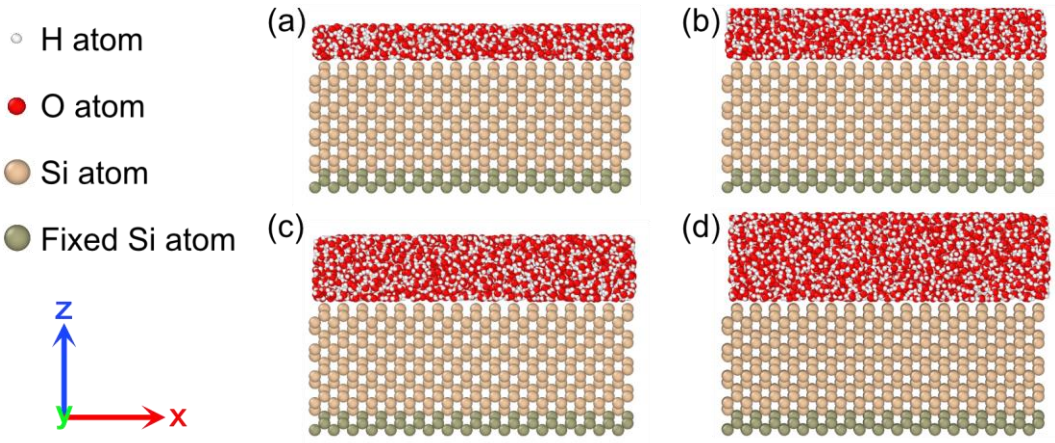

Figure 3-18. Sides views of silicon-water simulation models at the humidity levels of (a) 20%, (b) 40%, (c) 70%, and (d) 90%.

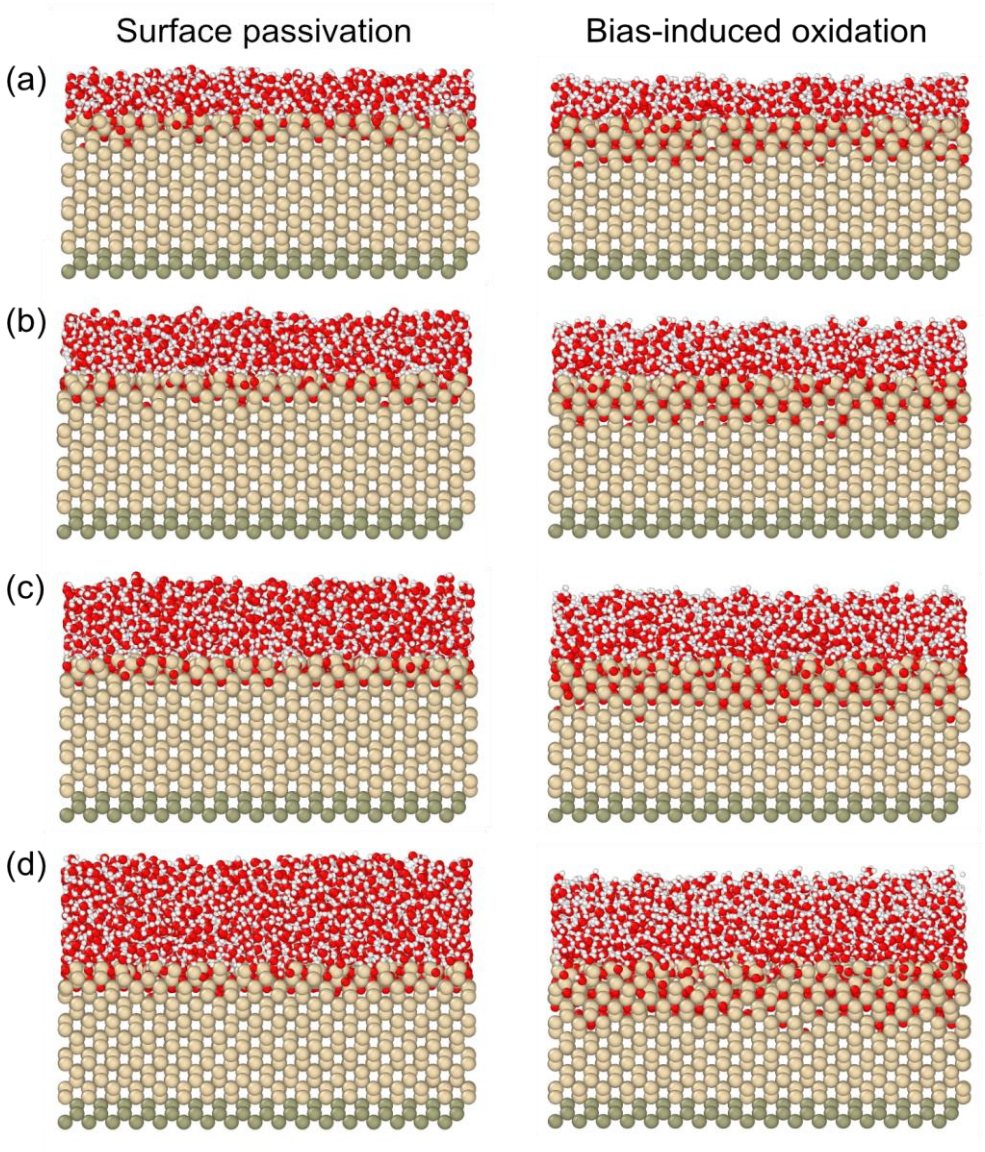

Figure 3-19. Side views of simulation results of surface passivation and bias-induced oxidation at relative humidity levels of (a) 20%, (b) 40%, (c) 70%, and (d) 90%.

3.5.2 Analysis of simulation results

Figure 3-19 shows the simulation results at 1000 and 2000 ps, which represent the reaction results of surface passivation and bias-induced oxidation at different humidity levels. It seems that the increased humidity can increase the penetration of O atoms into the silicon substrate, particularly for results of bias-induced oxidation processes.

In addition, as the bias-induced oxidation proceeded, the thickness of the water layer was observed to decrease, indicating the consumption of water.

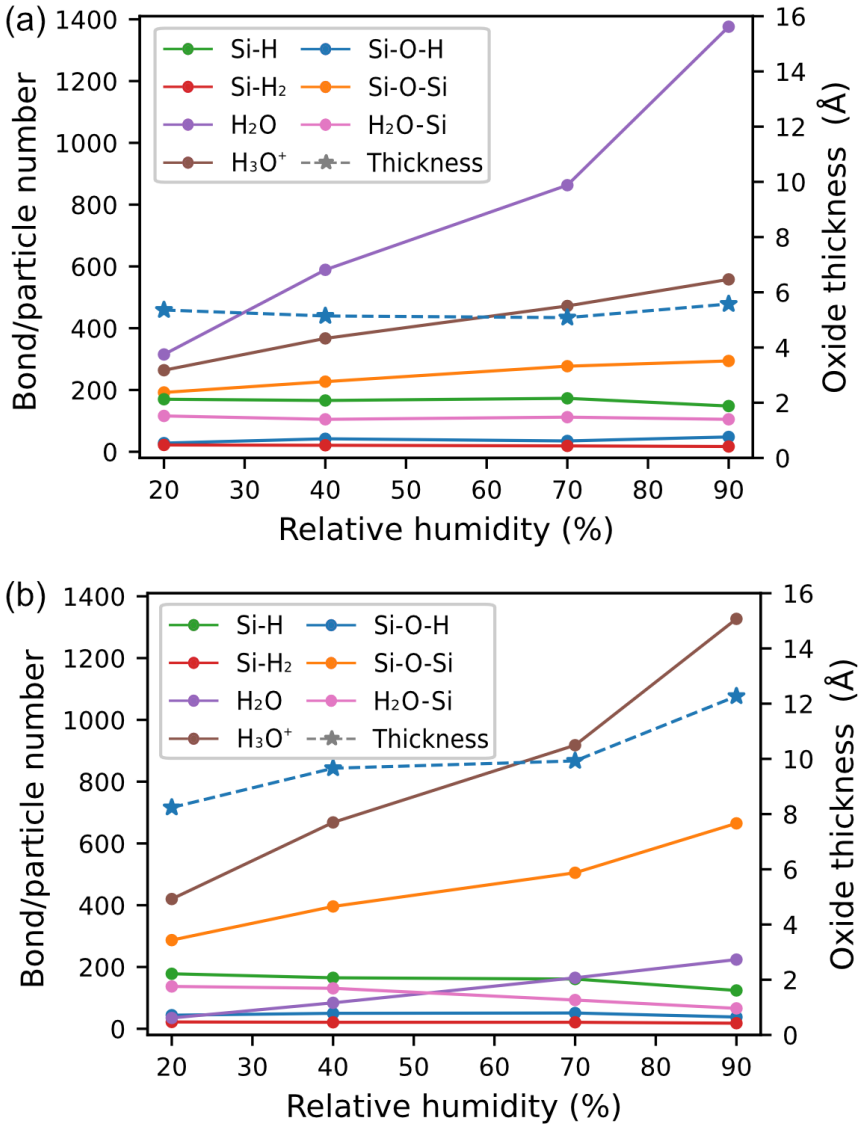

Figure 3-20. The number of bonds/particles and oxide thickness of (a) passivation results and (b) bias-induced oxidation results at different humidity levels.

Figure 3-20 (a) and (b) plot the bonds/particles number and oxide thickness of surface passivation and bias-induced oxidation results at the different humidity levels. The number of bonds that only exist at the surface does not appear to be affected by

humidity in both passivation and bias-induced oxidation results. However, the numbers of Si–O–Si bonds in both results increase with increasing humidity, and the increase is more pronounced in the bias-induced oxidation results.

As the humidity increases from 20% to 90%, the number of Si–O–Si bonds increases from 287 to 665, and the oxide thickness increases from 8.24 to 12.27 Å. These results show that higher humidity can enhance the degree of oxidation for both surface passivation and bias-induced oxidation processes, which aligns with and may provide a reaction-based interpretation of experimental observations [108].

3.5.3 Analysis of the reaction process

Figure 3-21 (a) and (b) show the evolution of the number of Si–O–Si bonds and oxide thickness. These results further indicated that a higher humidity could enhance the oxidation, as evidenced by the increased number of Si–O–Si bonds and oxide thicknesses in simulation results under higher humidity. The influencing mechanism should be related to the increased number of H_2O within the water layer, which facilitates the reaction (3-1).

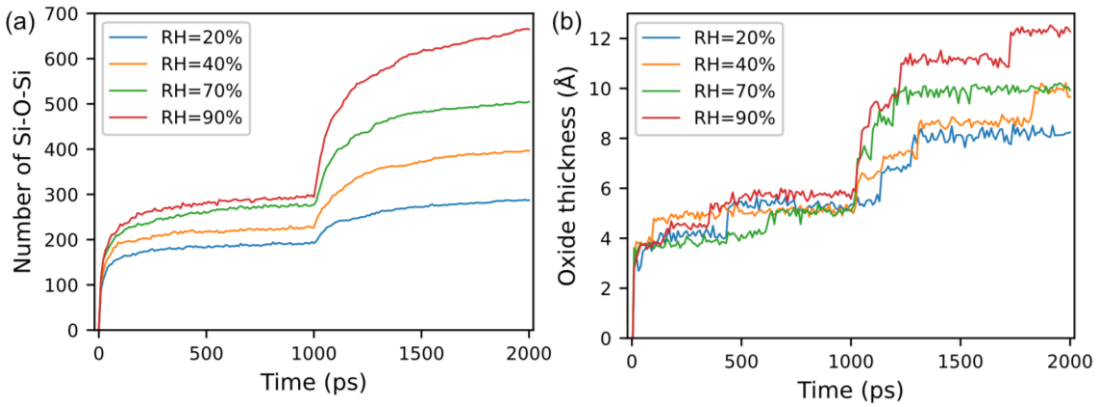

Figure 3-21. Time evolution of (a) the number of Si–O–Si bonds and (b) oxide thickness during passivation and bias-induced oxidation at different humidity levels. An electric field with a strength of 4 V/nm was applied at 1000 ps during the simulation.

Figure 3-22 (a–d) plot the distribution of Si–O–Si bonds of the simulation results during the bias-induced oxidation processes to reveal their chemical structures. These bond/particle distributions along the *z* axis indicate that an increase in humidity levels leads to an increase in the number of Si–O–Si bonds near the silicon-water interface, and the increase is more pronounced in the bias-induced oxidation results.

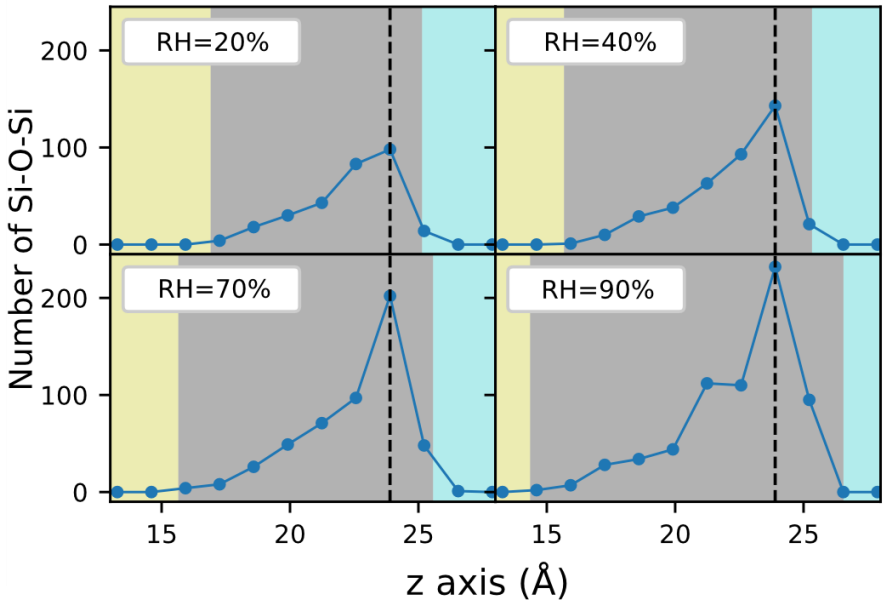

Figure 3-22. Distribution of Si–O–Si bonds (along *z*-axis) of simulation results of bias-induced oxidation at different humidity levels, in which shaded regions coloured with wheat, grey, and cyan represent silicon, oxide layer, and water, respectively. The vertical dashed line represents the first atomic layer in the initial model.

These findings contrast with the observations made under higher electric field strengths, where an increase in the electric field strength resulted in a more Si–O–Si bonds being formed at deeper positions under the surface. These results suggest that bias-induced oxidation under higher humidity and higher electric field strength involves different mechanisms in enhancing bias-induced oxidation. Under higher humidity, more H_2O exists in the water layer, which facilitates the reaction (3-1). Since

the dominant reaction mainly happens at the surface, this enhanced oxidation created more Si–O–Si bonds at the silicon surface.

3.6 Summary

In this chapter, ReaxFF MD simulations were performed to study the initial passivation and subsequent bias-induced oxidation on Si (1 0 0) surface in order to gain atomistic insight into the reaction mechanism of the LAO process. The chemical bonds, particles, and molecules involved in the reaction were analysed in detail. Through plotting their numbers, distributions, and evolution, this work presented a full characterisation of the composition of the oxide film and the reaction mechanism inherent in the reaction process. The surface passivation resulted in the creation of an oxide layer with a surface composition of Si–O–Si, H_2O–Si, Si–O–H, Si–H, and Si–H_2, while the oxidation component beneath the surface was dominated by Si–O–Si bonds. Subsequently, the application of an electric field facilitated a series of reactions, where O atoms moved from the water layer (H_2O/H_3O^+) to the oxide surface (H_2O–Si and Si–O–H) and then deep in the oxide film (Si–O–Si). The H_2O–Si and Si–O–H bonds on the surface acted as intermediate products, but their numbers were not apparently altered during the bias-induced oxidation. Overall, the bias-induced oxidation mainly consumed H_2O within the water layer and resulted in the formation of Si–O–Si bonds beneath the oxide surface.

The study also investigated effects of different electric field strengths and humidity levels on bias-induced oxidation processes. By analysing the numbers and distribution of particles/bonds in the system, the study demonstrated the mechanisms of oxidation enhancement in detail. The main reaction studied in Chapter 3 was found to be notably enhanced by increasing electric field strength and humidity, but through different

mechanisms. The enhanced electric field strength mainly promoted the diffusion of Si–O–Si bonds beneath the surface, while the enhanced humidity accelerated the reaction at the surface, resulting in different structures of the oxide film. These findings provide an atomistic understanding of the parametric effects of the LAO process. This knowledge can be useful in developing novel process-control strategies for LAO at the nano- and atomic scales.

Chapter 4 Method and feasibility study of pulse-modulated LAO nanolithography

4.1 Introduction

As demonstrated in Chapter 3, oxidation growth varies at different electric field strengths and durations during short exposure times. Consequently, voltage modulation emerges as an ideal oxidation-tuning approach for the LAO process. This implies that by modulating the pulse amplitude or duration, the LAO process can be flexibly adjusted, leading to the formation of oxide structures with diverse feature sizes. Since the pulsed voltage can be easily programmed through a pulse generator, this method is possible to achieve flexible and one-step nanofabrication of various nanostructures. In addition, by optimising AFM setups to minimise local oxide, as reviewed in Chapter 2, the LAO nanolithography is possible to obtain 3D nanofabrication with sub-10 nm feature sizes.

To validate this idea, this chapter first introduces the method of pulse-modulated LAO in detail, outlines the implementation of LAO using a commercial AFM and a pulse generator, and then performs the feasibility test for several simple nanostructures.

4.2 Pulse-modulated LAO approach

Figure 4-1 (a) illustrates a 2D schematic of the proposed pulse-modulated LAO nanolithography approach. By connecting the pulse generator to the AFM tip and substrate, the application of pulsed waveform can induce the local oxidation between the scanning probe and substrate. When pulses with varying widths or amplitudes are applied, nanodots with different widths and heights can be created. Furthermore, the pitch distance between nanodots is determined by the pulse period, tip scanning

velocity and trajectory, so adjusting the pulse period can control the 2D mapping of nanodots across the tip scan area, as demonstrated in Figure 4-1 (b). Therefore, a combined modulation of pulse amplitude, width, and period makes it possible to achieve the control of oxidation growth and 2D mapping of nanodots simultaneously. Since the pulse parameters can be digitally modulated through a pulse generator, this method is possible to achieve flexible and one-step 3D nanofabrication without resorting to other control systems.

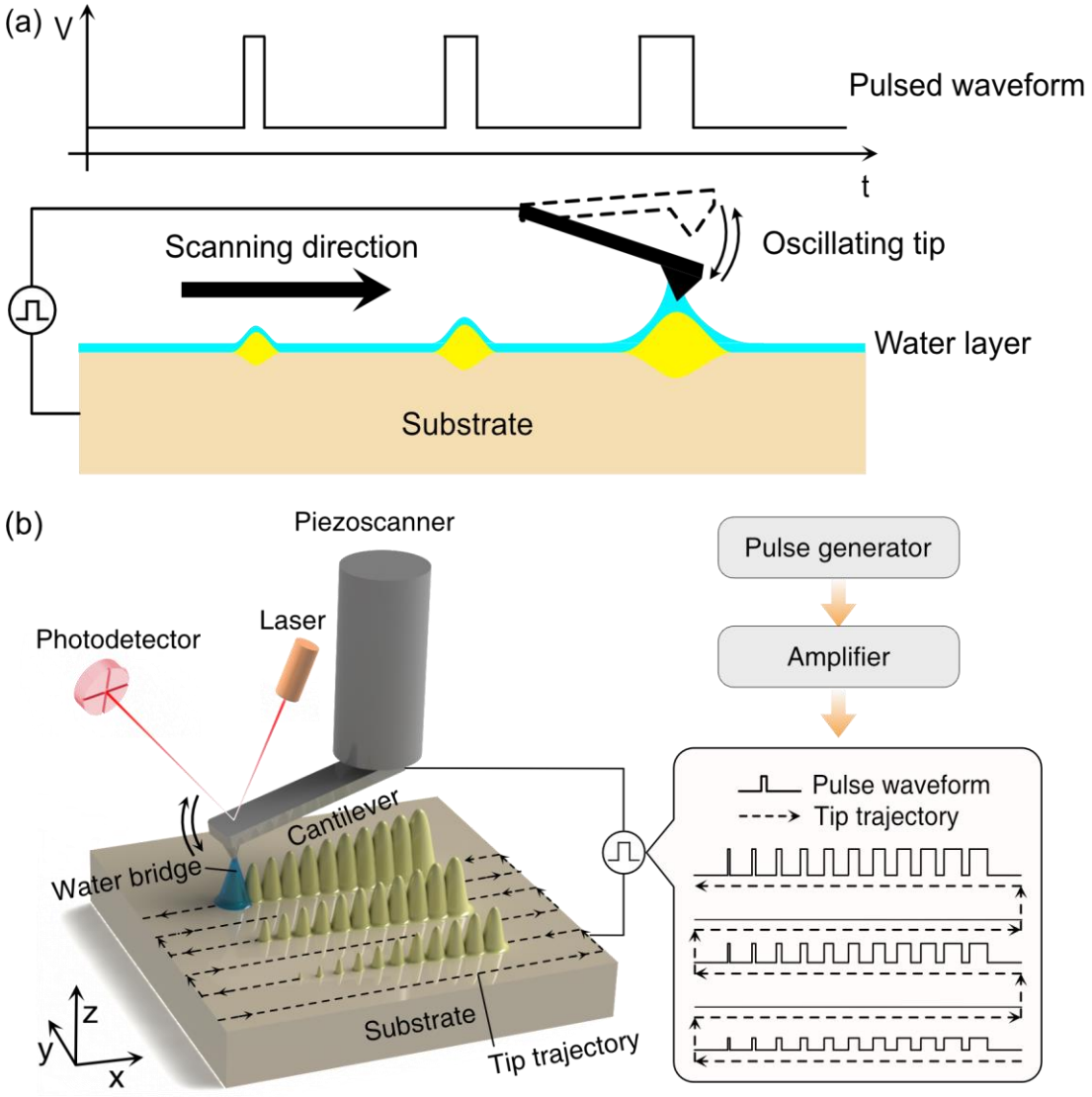

Figure 4-1. (a) 2D and (b) 3D schematics of pulse-modulated LAO nanolithography.

4.3 LAO nanolithography setup

The literature review in Chapter 2 suggests that utilising high-amplitude and short-width pulses in conjunction with tapping mode AFM provides numerous advantages, including enhanced resolution, reliable and reproducible results, precise control, and the ability to achieve continuous LAO nanopatterning. Consequently, this thesis will employ the tapping-mode AFM along with pulses with amplitudes between 13–25 V and widths between 15–300 μs for the LAO nanolithography process. This is because previous reports have suggested that voltages higher than 25 V may induce reactions with different mechanisms [214], while pulses with widths shorter than 15 μs may not result in apparent oxidation, as observed in experiments.

4.3.1 AFM setup

All the LAO experiments in this thesis were carried out using a Bruker (Veeco) Dimension 3100 Atomic Force Microscope, as shown in Figure 4-2. To achieve a high patterning and imaging resolution, the AFM was always operated under the tapping mode using probes with nominal curvature at less than 10 nm. The AFM tip scanner was operated under raster scan mode so that the scan rate, sampling line density, and scan size can be set through the AFM interface. During the LAO nanofabrication, the position feedback loop of the AFM was on to keep the tip-sample distance at a constant value during the individual oxidation and reset stages. This allowed continuous nanofabrication in the tip scan area. To increase the tip-surface contact for the formation of water bridge, the cantilever oscillating amplitude was reduced by setting the setpoint at 15% of that used in imaging [215]. The enlargement of oxide due to tip scan is negligible in this work because of the use of ultra-short pulses and a slow

scanning speed, where the tip displacement during the pulse width is always several orders smaller than the lateral dimension of the nanodot.

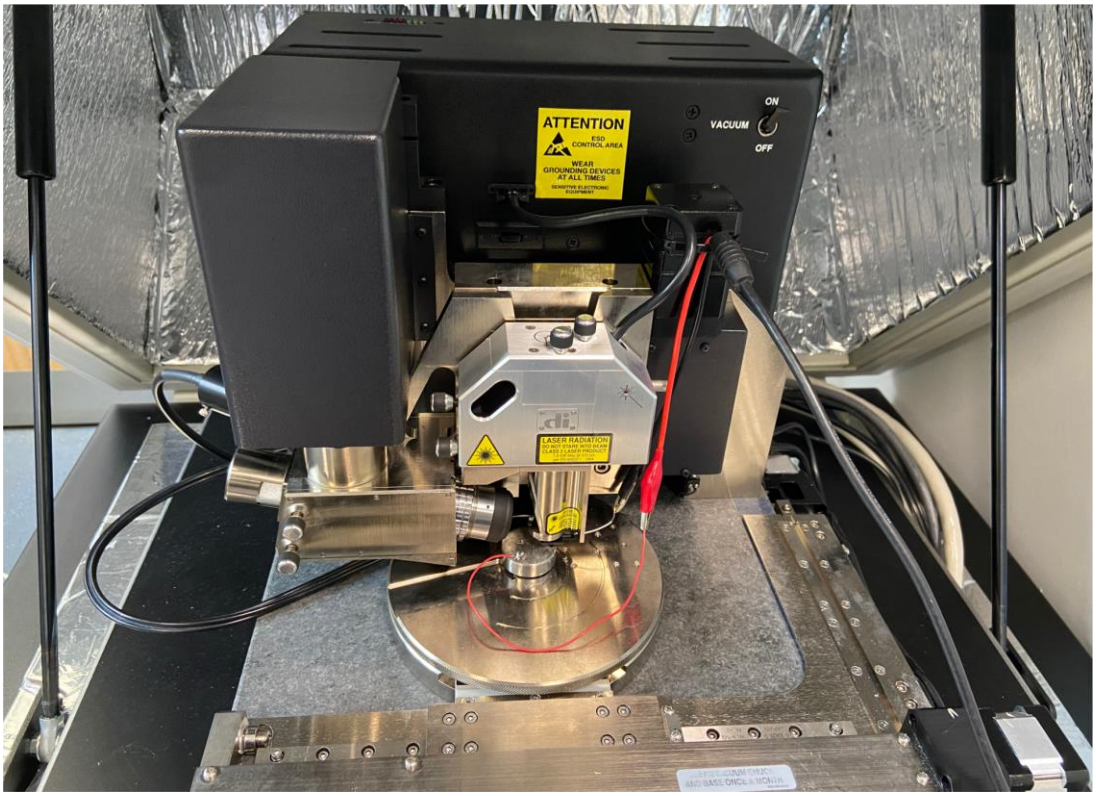

Figure 4-2. Schematic of Bruker Dimension 3100 AFM connected with an external power supply.

Given the significant impact of humidity on the LAO process, the nanofabrication conducted in this thesis was always carried out under atmospheric conditions (20 °C) with relative humidity at 25–30%. To ensure precise humidity control, a hygrometer with an accuracy of ±1% was employed to monitor and maintain the desired humidity levels throughout the experiments. The oxide patterns were imaged right after their creation, and the AFM images were analysed using the Bruker NanoScope Analysis 1.7 software. To compensate for the dilation effect introduced by the tip radius, full

width at half maximum (FWHM) or full diameter at half maximum (FDHM) were used in this work to represent the width of oxide lines and diameter of oxide dots.

4.3.2 Pulse generator

To give a feasibility test, this chapter uses a conventional arbitrary generator (TGF4042, Aim-TTi) to create pulses. The schematic of the pulse generator is shown in Figure A-1. This pulse generator offers signal generation capability up to 240 MHz, the detailed specification of which is shown in Table A-1. To enable program control, an Ethernet interface was utilised by connecting the generator to a laptop. This allowed pulse parameters to be adjusted by sending commands from the laptop using a program.

Since the output voltage of the pulse generator is equal to or less than 10 V, it cannot obtain a sufficiently high electric field between the tip and the sample for the LAO process. Therefore, the modulated pulse signal was amplified by a power amplifier (E01.A2, CoreMorrow) by a factor of 12. The schematic and specification of the power amplifier are shown in Figure B-1 and Table B-1.

4.3.3 Probes and holders

To induce oxidation, a voltage signal was introduced onto the AFM, with the sample substrate at a negative bias to the conductive probe. In this work, conductive AFM probes (model RTESP7) with a nominal tip radius of less than 10 nm were used for the nanofabrication and imaging. A tip radius close to 10 nm was selected as a compromise between the aims of achieving high patterning resolution and minimised tool wear. These probes were made by Phosphorus (n) doped Si to increase the conductivity and with no coatings on the tip. Some probes with metallic coatings have better conductivity, but they normally have large tip curvature radii, thus weakening

the spatial resolution. The stiffness and resonance frequency are typically 40 N/m and 300 kHz, respectively.

Figure 4-3. Schematic of SCM probe holder (model Bruker DSCMSCH).

In order to connect the pulsed voltage to the conductive probe, a scanning capacitance microscopy (SCM) probe holder (model Bruker DSCMSCH) was used in this study. As shown in Figure 4-3, this probe holder is equipped with a short external cable that enables the connection of high-voltage signals through an external circuit. Although a conventional probe holder (model Bruker DAFMCH) also has the capability for the bias connection, the voltage amplitude typically cannot exceed 20 V due to the dependence on a built-in circuit of the AFM.

4.3.4 Sample preparation

This thesis employs silicon wafers as substrates, which were procured from Inseto (UK) Limited. The detailed specifications are listed in Table C-1. The silicon wafer has a diameter of 100 mm and a nominal thickness of 525 μm, with a surface orientation of (1 0 0), which is consistent with the surface used in the simulation study in Chapter 3. The wafer is p-type boron doped with a conductivity range of 1–10 Ω·cm.

The wafer has been double-side polished, resulting in a surface roughness (Ra) of less than 0.3 nm.

Before performing the LAO experiment, the wafers were cleaved into small pieces using a diamond cutter. Then, these small-piece samples were cleaned by sonication in an $NH_4OH/H_2O_2/H_2O$ (1:1:5) solution for 10 mins to remove surface contaminations. Finally, they were rinsed with deionised water and blown with a dry N_2 gas jet.

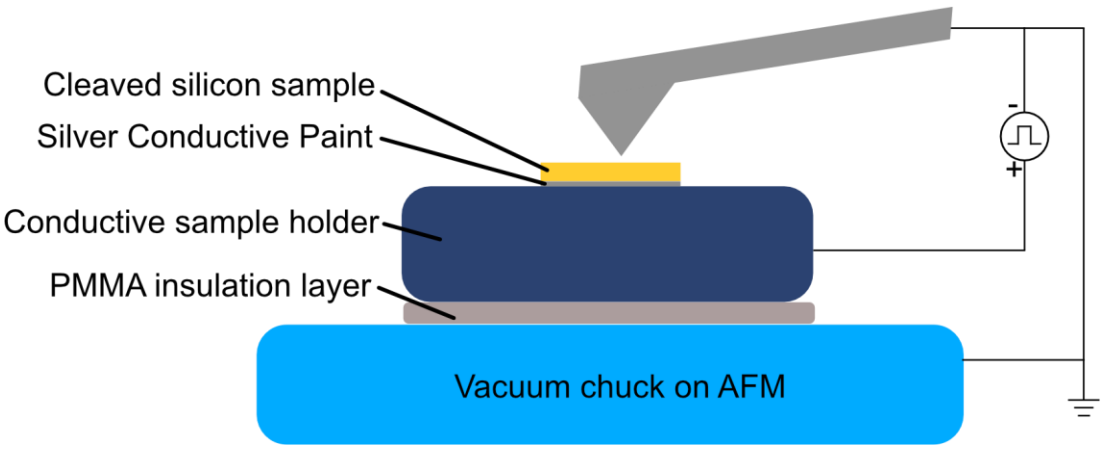

Figure 4-4. Schematic of sample mounting on AFM.

Figure 4-4 shows the schematic of the sample mounting method used in this work. The positive bias from the pulse generator was connected to the sample holder and the ground end was connected to the conductive probe. However, since the conductive vacuum chuck of the AFM was also grounded, an insulation layer is necessary to isolate the conductive sample holder from the vacuum chuck. In this work, a smooth PMMA layer was attached beneath the conductive sample holder to achieve isolation. To ensure the proper connection of the silicon sample to the positive bias, silver conductive paint was used to glue the silicon sample to the sample holder. Before conducting the LAO experiment, conductivity and resistance tests were performed to

ensure that the pulsed voltage could be applied between the conductive probe and the silicon sample.

4.4 Feasibility study

This section will present the fabrication of several nanostructures by varying pulse parameters in order to demonstrate the feasibility of the pulse-modulated LAO nanolithography approach using the testing platform described above. The pulse modulation was achieved by adjusting the settings of the Aim-TTi pulse generator.

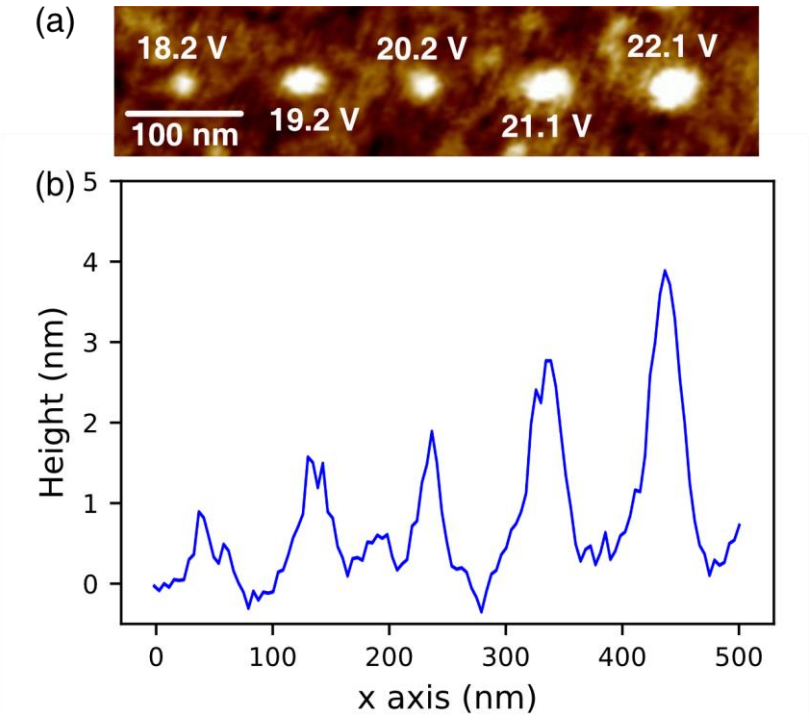

Figure 4-5. Size dependence on pulse amplitudes. (a) AFM image of nanodots created at a fixed pulse duration of 60 μs with amplitudes between 18.2 and 22.1 V; (b) a cross-sectional profile across these nanodots.

4.4.1 Nanodots

To validate the creation of nanodots, a series of pulses with modulated amplitudes or widths were applied to the scanning probe. During the nanopatterning, the scanning size was set at 1 μm, and the scanning frequency was set at 0.25 Hz, resulting in a

scanning speed of 0.5 μm/s. Other parameters, such as tip oscillating amplitude and tip-sample distance, were kept constant so that only the pulse amplitude and width affected the feature size of the oxidation dots. In the first experiment, the pulse period and width were kept constant at 0.2 s and 60 μs, respectively. Linear pulse amplitude modulation was applied to pulses with amplitudes ranging from 18.2 to 22.1 V, and the modulation period was set to 1 s, resulting in the application of five pulses with different amplitudes. The patterning results and their cross-sections are presented in Figure 4-5. The height of oxide dots increased linearly from 0.8 nm to 3.8 nm as the pulse amplitude increased from 18.2 to 22.1 V.

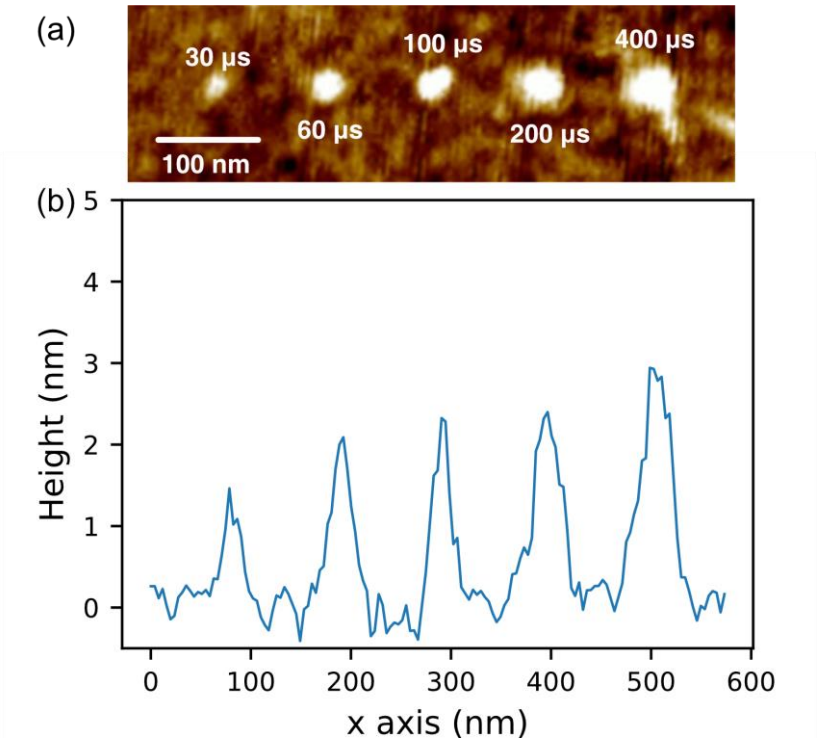

Figure 4-6. (a) AFM image of nanodots created at a fixed pulse amplitude of 19.2 V and pulse duration between 30 and 400 μs; (b) a section view shows the profile of nanodots in (a).

Pulse width is another critical factor that influences the growth of nanodots during the LAO process. The effect of pulse width on the size of oxide dots was investigated

through pulse width modulation (pulse width varying from 30–400 μs) while keeping the pulse period and amplitude constant at 0.2 s and 19.2 V, respectively. After applying these pulses, the resulting oxide dots and their cross-sectional view are shown in Figure 4-6. Apparently, the height of the oxide dots increased with increasing pulse width, which agrees with previous experimental studies [103].

4.4.2 Nanolines

The results above demonstrate that oxide dots can be generated by applying ultra-short pulses to a scanning probe. By varying the intervals between these pulses, nanodots with different spacing can be created. As the pulse intervals further reduce, an array of nanodots will eventually connect to form a nanoline.

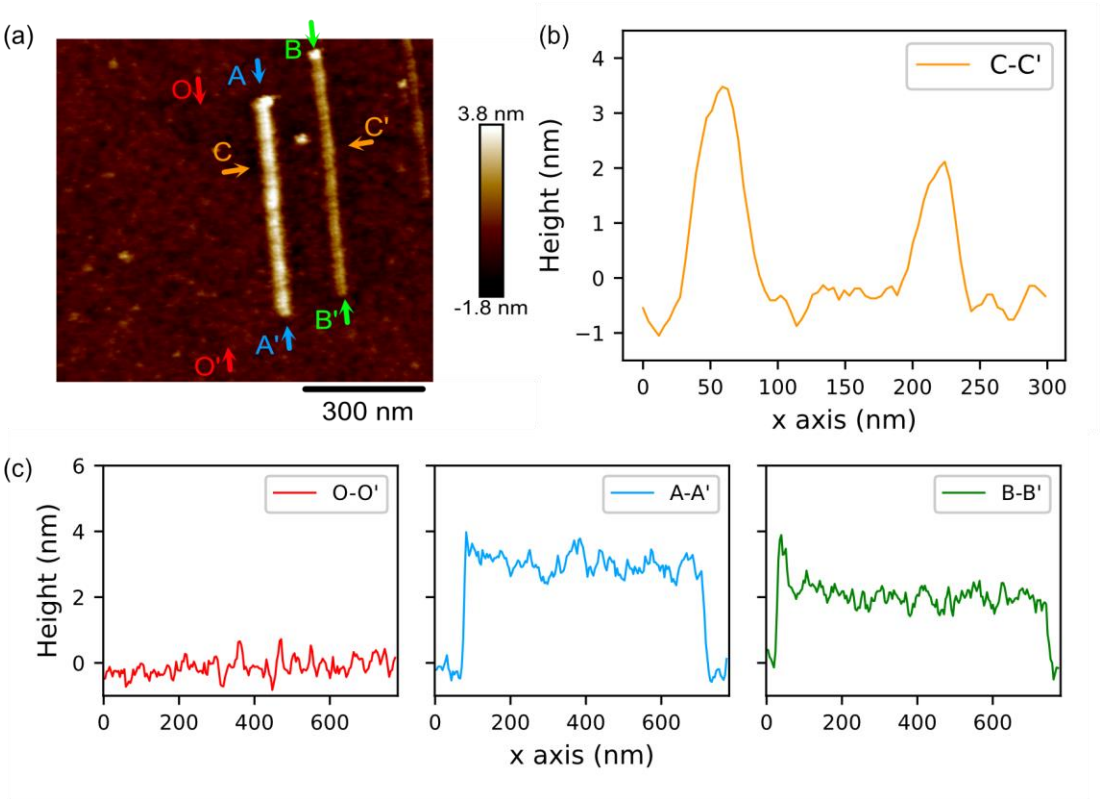

Figure 4-7. Schematic of nanolines created through pulse modulation. (a) 2D image. (b) Cross-sectional profiles along C–C'. (c) Cross-sectional profiles along O–O', A–A', and B–B'.

To verify the nanopatterning of nanolines, two groups of pulses were generated, each consisting of 350 pulses with the same period of 10 ms and amplitude of 19.2 V but with two different widths at 200 and 60 μs, respectively. By applying two groups of pulses to a scanning probe at the velocity of 200 nm/s separately, two continuous nanolines were created, as shown in Figure 4-7 (a) and (c). Due to the difference in pulse widths, these two nanolines have different heights and widths, as indicated in the cross-sectional view in Figure 4-7 (b). The cross sections along the nanolines in Figure 4-7 (c) demonstrate that these nanolines have good continuity in comparison with the unoxidized surface.

4.4.3 2D nanostructure

The above results show that the spacings of nanodots can be determined by using different pulse periods for a linear scanning probe. If we consider the raster scan trajectory of the probe, nanodots could be mapped through the tip scan area. Through synchronising the tip scan with the whole pulse waveform, it is possible to correlate the position of the tip at each application of the ultrashort pulse with the pulse start time T'_i of each pulse by means of tip scan parameters.

Herein, the T'_i can be calculated through the sum of its preceding pulse periods:

$$T'_i = \sum_{j=0}^{i} T_j \tag{4-1}$$

The tip position (x_{ci}, y_{ci}), i.e., the centre coordinate of the nanodot, can be described as:

$$x_{ci}(T'_i) = 2 \times L \times f \times (T'_i \bmod f^{-1}) \tag{4-2}$$

and

$$y_{ci}(T'_i) = d \times \lfloor T'_i \rfloor \tag{4-3}$$

where x and y are along and perpendicular to the tip scanning directions, respectively, as shown in Figure 4-1. f, L, and d are the scan rate, scan size, and spacing between the adjacent scan lines, which can be set through the AFM interface. If T_i follows

$$(n-1) \times f^{-1} \leq T_i \leq (n-0.5) \times f^{-1} \tag{4-4}$$

where n is a positive integer, oxide dots can be created when the tip is in the same scanning direction.

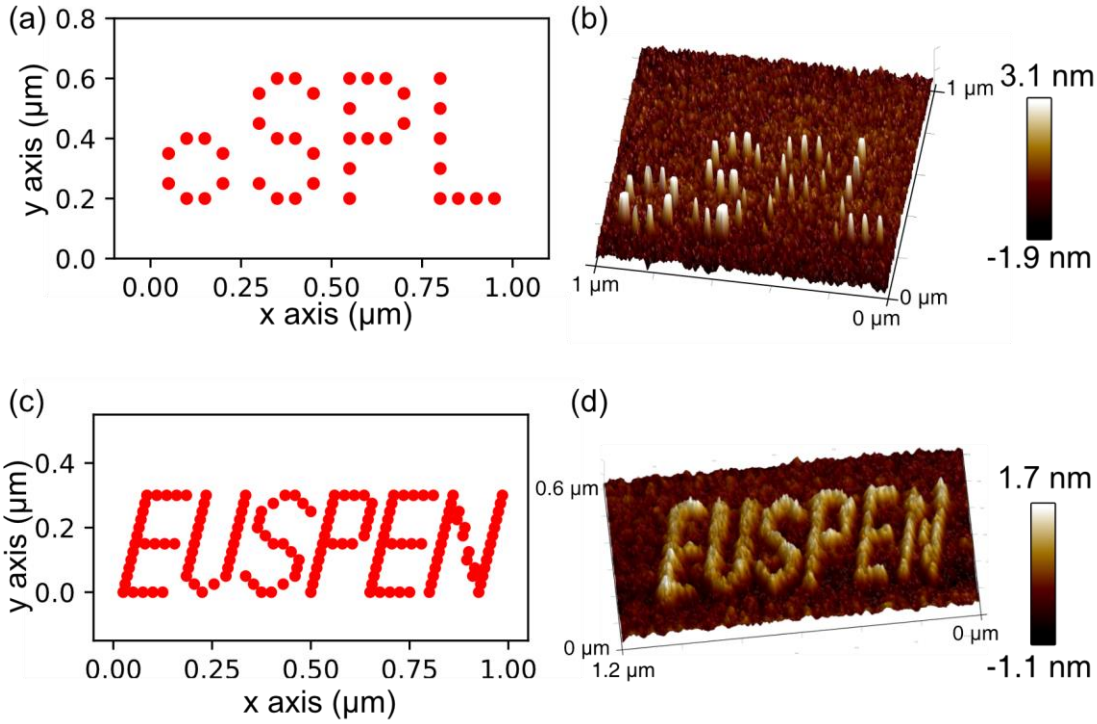

Figure 4-8. Schematics of the design and nanofabrication results of 2D nanostructures showing (a–b) 'oSPL' and (c–d) '*EUSPEN*', created by pulse period modulation.

On the basis of equations (4-1), (4-2), (4-3), and (4-4), nanodots are possible to be created with different spacings and mapped across the scanning area. A simple Python program was developed to convert coordinates into arbitrary pulse waveform files, which can be used to define arbitrary waveforms through the function generator. Using these waveform files, letterings showing 'oSPL' and '*EUSPEN*' were designed and

created separately, as shown in Figure 4-8. During the nanofabrication, pulse amplitudes and widths were kept at 19.2 V and 60 μs.

4.4.4 3D nanostructure

Based on the previous results, it is evident that controlling the pulse amplitude or width can regulate the growth of oxidation for each nanodot, while adjusting the pulse period can modify the position of each nanodot. The combined modulation of these parameters is thus possible to create 3D nanostructures within the tip scan area.

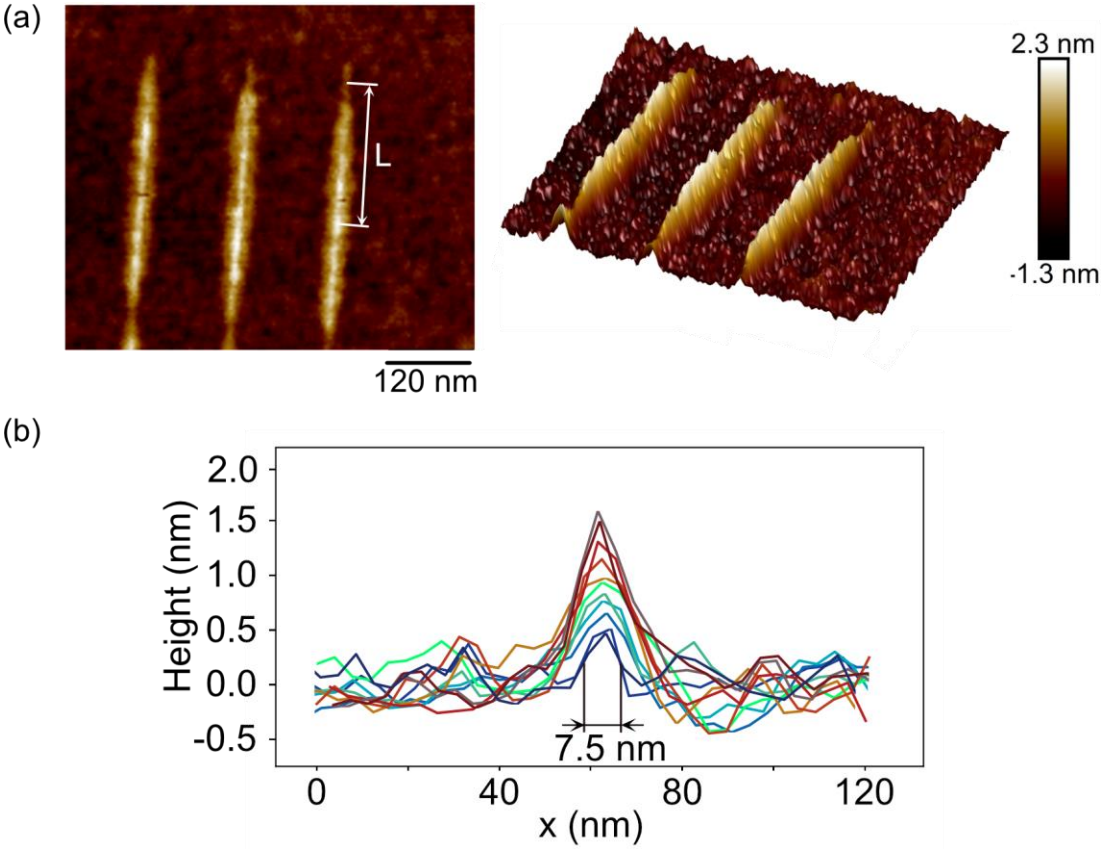

Figure 4-9. (a) Topographical images of gradient nanolines; (b) eleven cross-sectional profiles taken perpendicular to the L in (a).

First, the feasibility of the creation of gradient nanolines was tested. The pulse widths were modulated in a triangle shape from 15 to 300 μs, while the pulse amplitude and period were kept at 19.6 V and 10 ms, respectively. By applying these pulses three

times, three gradient lines were generated, as shown in Figure 4-9 (a). Eleven cross-sections were taken at 20 nm intervals between one segment of the gradient nanoline (L in Figure 4-9 (a)) and plotted in Figure 4-9 (b) to study the profile. An apparent gradient was observed along the scanning direction. When the pulse width increased from 15 to 300 μs, the height increased from 0.4 to 1.6 nm, respectively. At the same time, the width of nanoline increased from 7.5 to 16 nm, and the minimum width appeared to be 7.5 nm when a 15 μs pulse was applied. It is worth noting that the achievable line width or dot diameter strongly depends on the radius of the tip used in nanofabrication and imaging. For the type of probe used in this work, a brand-new probe is necessary to achieve a sub-10 nm feature size in the lateral dimension.

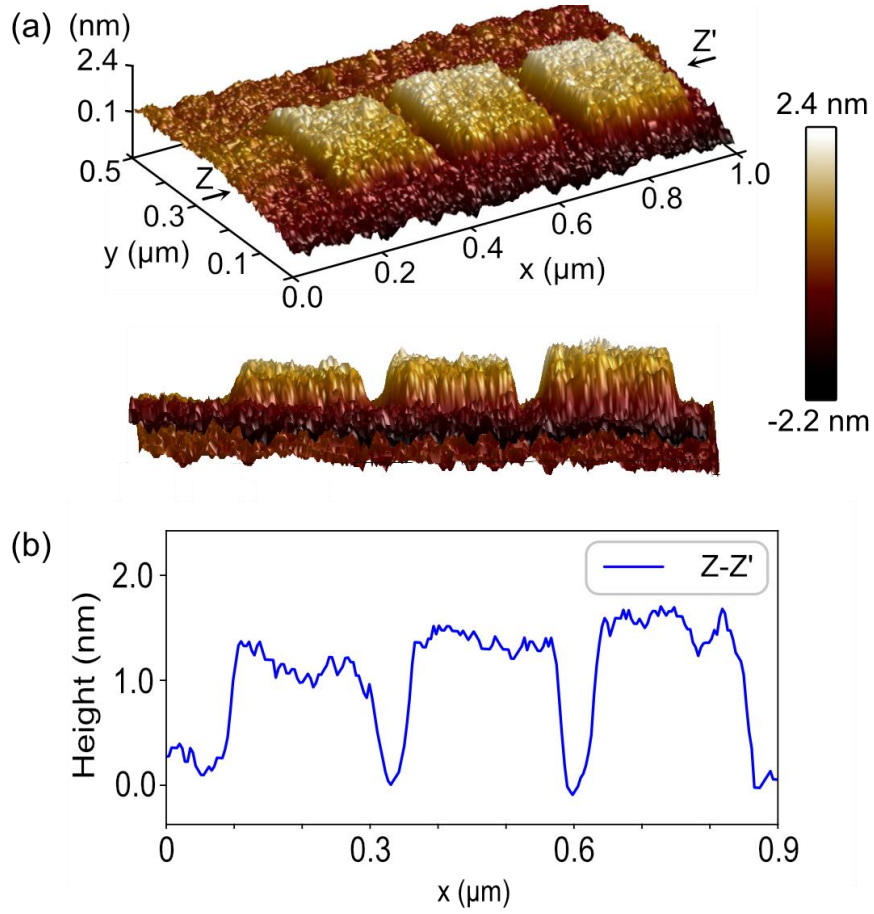

Figure 4-10. (a) Topographical image of resulting 3D nano-square structures; (b) cross-sectional profile along Z–Z’ in (a).

If the pitch between scan lines is reduced, adjacent nanolines can merge with each other to form a continuous square nanostructure. Three groups of pulses were generated with fixed periods of 10 ms to enable nanodots to overlap and form nanolines. The pitch between adjacent scans was adjusted at 12.5 nm to allow for the formation of continuous square structures by overlapping nanolines side by side. The pulse widths in each group varied at 20, 60, and 200 μs, while the pulse amplitude remained constant at 21.1 V. By applying these pulses during tip scanning, 3D nanostructures were created, as shown in Figure 4-10 (a). The 3D image and cross-sections in Figure 4-10 show an apparent gradient in height for each nano-square structure.

4.5 Limitations

On the basis of the above feasibility tests, the effectiveness of the pulse-modulated LAO for the fabrication of various nanostructures was demonstrated. Nanostructures, including nanodots, nanolines, 2D and 3D nanostructures, can be created through pulse modulation, and the minimum feature sizes of nanolines appeared to be at sub-10 nm in line width and sub-nm in height. However, the current experimental setups for 3D nanofabrication have several limitations. Firstly, the relationship between the input pulse parameters and the geometry of resulting nanostructures is still unclear, which makes it difficult to achieve digital and flexible geometric control for arbitrary and complex 3D nanostructures with good tunability and precision. Therefore, a systematic modelling method is necessarily required to achieve an in-depth understanding of the pulse-modulated LAO process and to assist in the digital control of the nanofabrication process. In addition, the conventional functional generator used in this work has several limitations in achieving digital programming of pulse parameters due to the

limited capacitance of arbitrary waveforms and delays when receiving commands from PCs. These limitations highlight the requirement for a fully programmable function generator that can modulate the parameters for a large number of pulses in a flexible manner.

4.6 Summary

This chapter introduced the method and experimental setup of a new pulse-modulated LAO nanolithography. Due to the simplicity of pulse programming, this approach is easy to set up using a simple platform. The AFM setups, pulse generator, and sample preparation were described in detail to explain the method used to achieve flexible fabrication of 3D nanostructures with sub-10 nm feature sizes. Then, feasibility tests were performed, which confirmed that various nanostructures were possible to be created by this approach with the minimum line width at sub-10 nm. However, feasibility tests also revealed several limitations, highlighting the need for a systematic process model and a fully programmable pulse generator to achieve precise and accurate control in 3D nanofabrication. The following chapter will present the research works to address these limitations.

Chapter 5 Flexible one-step fabrication of progammable 3D nanostructures

5.1 Introduction

In the ever-evolving field of nano/quantum products and devices, there is a growing demand for nanofabrication techniques that are flexible, maskless, and cost-effective while being able to manufacture nanostructures with various shapes on different materials. However, the current semiconductor manufacturing processes are either expensive, slow or suffer from high defect rates due to multi-step operations. This chapter aims to investigate and validate a pulse-modulated LAO nanolithography technique for fabricating arbitrary and complex 3D nanostructures in a flexible and one-step process. The simplicity of pulse programming is utilised to achieve geometric control of 3D nanostructures based on the process model. Consequently, this approach offers 3D nanofabrication without the need for complex operations and control systems.

In this chapter, the dependencies of oxidation growth on pulse periods, amplitudes, and widths are first explored, which presents the relationship between the oxide feature sizes and pulse parameters. Then, based on these results, a process model for pulse-modulated LAO nanolithography is developed, through which the geometry of expected 3D nanostructures can be modelled based on the parameters of pulses and tip scans. Furthermore, a fully programmable pulse generator is developed and validated, through which a large number of pulses can be flexibly and digitally modulated, allowing the nanofabrication of complex 3D nanostructures. Finally, flexible and one-step nanofabrication is performed to validate the capability, precision, and accuracy in

fabricating complex 3D nanostructures through the pulse-modulated LAO nanolithography approach.

5.2 Parametric study

In this section, the effects of pulse periods, amplitudes, and widths on oxide growth are first investigated through a series of parametric studies. The pulses were created and modulated using the function generator described in Figure A-1. During the nanopatterning, the tip was raster scanning across a 1 × 1 μm area at the velocity of 200 nm/s. Other conditions, including temperature, humidity, and tip-sample distance, were always kept at the same values as described in Chapter 4.

5.2.1 Dependence of pulse periods

As the pulse period directly determines the overlapping of nanodots, this section first investigates the effect of pulse periods on the generation of nanolines, which can be regarded as an ordered assembly of nanodots [103]. Herein, pulses were created with the same amplitude of 19.6 V and width of 60 μs but with different periods.

Through the program control of the function generator, ten groups of pulses were applied separately, and each had the same total time length of 4 s, during which the tip was scanned over each equal-length line segment. Since the pulse periods in each group varies from 0.1 to 100 ms (corresponding to pulse duties from 60% to 0.06%), different number of nanodots from 40000 to 40 were applied, respectively. The resulting oxide lines and their cross-sections are shown in Figure 5-1. When the pulse period decreased from 100 to 40 ms, discreet nanodots gradually formed a continuous oxide line, as shown in Figure 5-1 (c). With a further decrease of pulse period to 4 ms, the oxide lines kept continuous, but the height of nanoline increased, as demonstrated in Figure 5-1 (b).

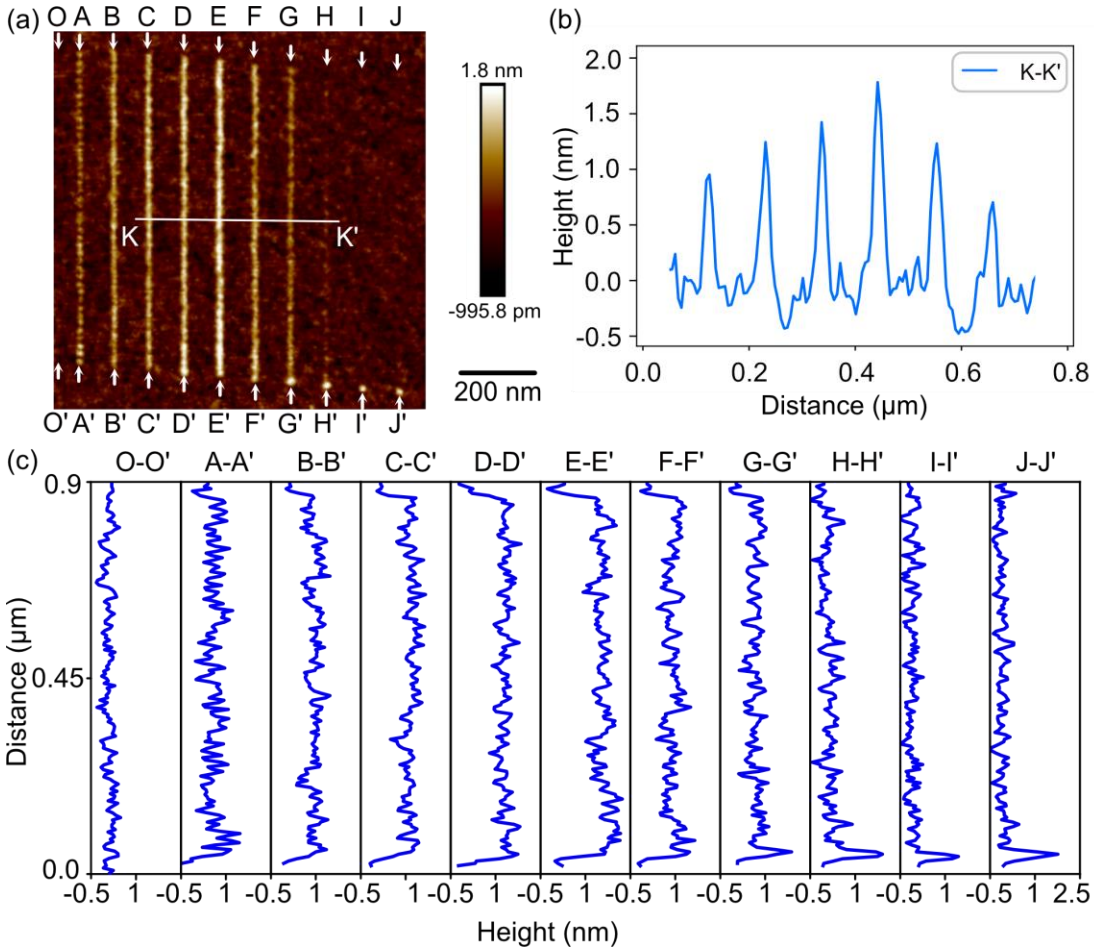

Figure 5-1. (a) Schematic of nanodot arrays created by different pulse periods. Pulse periods from A–A' to J–J': 100, 40, 20, 10, 4, 2, 1, 0.4, 0.2, and 0.1 ms; (b) a cross-sectional profile of nanolines; and (c) cross-sectional profiles across each nanodot array. O–O' represented the unoxidized surface.

However, when the pulse period is less than 4 ms, no more continuous oxide line was found. Oxidation growth was only apparent at the start point, leaving the oxide line incomplete. When the pulse periods were at 200 and 100 μs (pulse duty at 15 and 30%), the pulses could only create one nanodot at the start point. As reported in previous research work [215], the underlying cause could be the break of the water meniscus caused by an enlarged tip-sample distance. Each pulse induced oxidation while at the same time leading to the electrostatic attraction between the tip and sample. Since the

feedback loop kept on during the process, the tip could be pulled away from the surface to sustain a certain degree of tip-sample interaction; and when the pulse ends, the tip will return to the previous height to the surface under the feedback [97]. In this case, the damping time under the feedback control is critical for the creation of continuous oxide lines. When the pulse period is longer than the damping time, each oxidation occurs at basically the same tip-sample distance, which facilitates the formation of uniformly sized oxides. However, with the decrease in pulse period, the tip might not have enough time to return to its previous scanning position during the nanopatterning, which could increase the tip-sample distance when the next oxidation occurred. This could break the water bridge and form discontinuous oxidation when the pulse period is less than 4 ms.

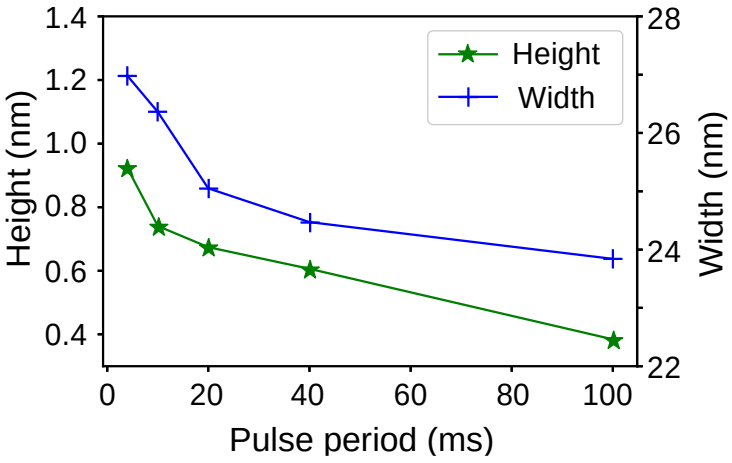

Figure 5-2. Dependence of oxide height and width on the pulse periods ranging from 4–40 ms at the pulse amplitude of 19.6 V and width of 60 μs.

In combination with the above findings, pulses with periods ranging from 4 to 40 ms can generate nanolines with decent continuity in comparison with the unoxidized surface (see O–O') in Figure 5-1 (c). The dependence of mean oxide height and width on the pulse period (between 4 to 40 ms) is shown in Figure 5-2. Both the height and

width of oxide lines increased with the decrease in pulse period, indicating that smaller pulse periods enlarge both the horizontal and vertical dimensions of the resulting nanolines. This is because reducing the pulse period can increase the number of equal-width pulses applied in the same scan distance, resulting in enhanced current flow during the oxidation process. It is important to note that the effects of pulse periods may be influenced by a combination of factors, such as oxide overlap, tip-sample distance, and surface charge distribution at different pulse periods. Consequently, there exists a range of pulse periods that can generate continuous nanolines, and the relationship between pulse periods and oxide feature sizes can be represented by a function that can be determined through experimental tests.

5.2.2 Dependence of pulse amplitude and width

To determine the effect of pulse amplitudes and widths on oxidation growth, pulses were modulated in both amplitude and width under the same period of 10 ms. Figure 5-3 (a) shows an array of gradient nanolines created through the modulation of pulse amplitudes and widths. In the *x* direction (along the tip scanning), pulses with the same amplitude were used while pulse widths varied from 15 to 300 μs in the shape of a logarithmic curve, aiming to create gradient nanolines. In the *y* direction (perpendicular to the tip scanning), the pulses were programmed to have different amplitudes, ranging linearly from 15.6 to 24 V, aiming to achieve gradience between nanolines. As a result, these nanolines show a 3D feature. The mean height and width of the nanolines were obtained by measuring the average values of 5-equal distances taken from each nanoline. Figure 5-3 (b) and (c) show their dependence on pulse amplitude and width. It can be seen that the oxide size increased linearly with pulse

amplitude but logarithmically with pulse width. The power-of-time dependence can be explained by charge-dependence kinetics [216].

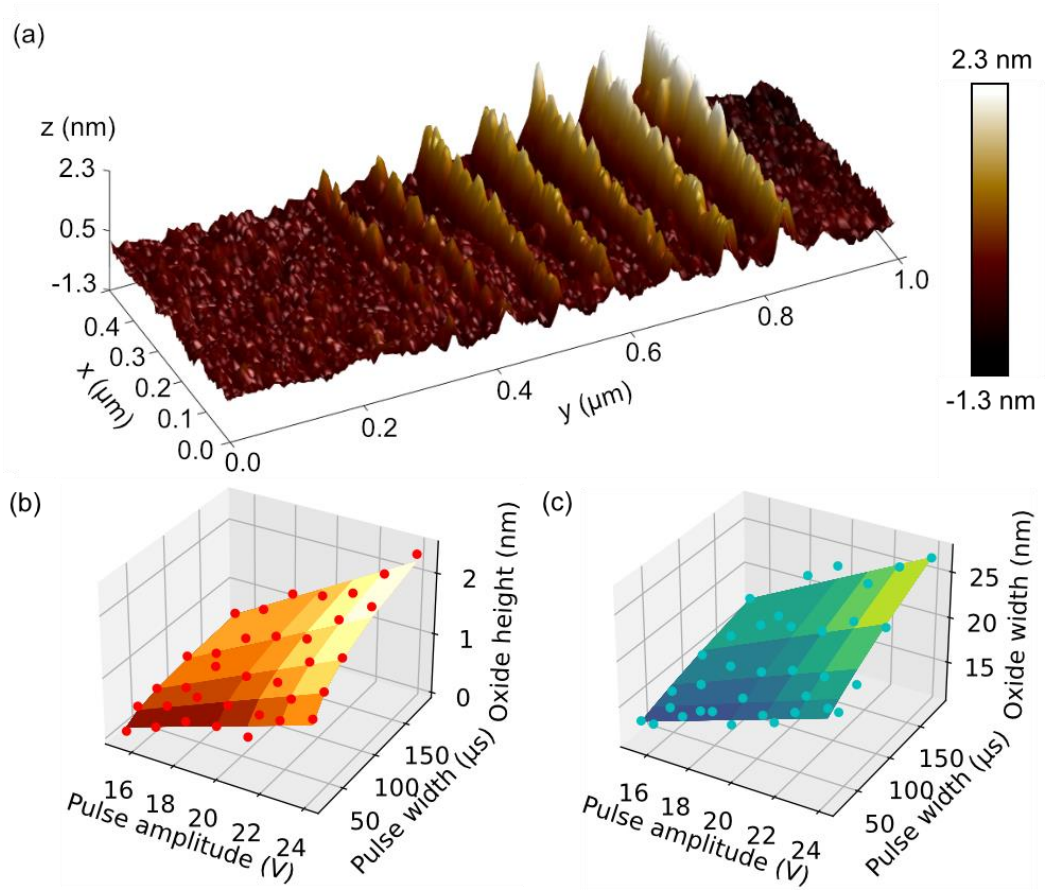

Figure 5-3 (a) Schematic of a gradient nanoline array created through the modulation of pulse amplitude and width; scatter and fitting surface plots of the oxide (b) height and (c) width as functions of pulse amplitude and width.

The dependencies of oxide feature sizes on pulse amplitude and width can be described as:

$$h_o(A,t) = h_1(A) + h_2(A)\ln(\mathrm{t}) \tag{5-1}$$

and

$$h_o(A,t) = w_1(A) + w_2(A)\ln(t) \tag{5-2}$$

where $h_o(A,t)$ and $w_o(A,t)$ are the height and width of oxide lines as functions of pulse amplitude A and width t when the pulse period T is held constant. Here $h_1(A) = -0.021A - 0.083$, $h_2(A) = 0.043A - 0.476$, $w_1(A) = 0.173A - 0.083$ and $w_2(A) = 0.180A - 0.890$. The lengths, pulse amplitudes and widths are in the units of nm, volts, and μs. On the basis of these results, it is demonstrated that the modulation of pulse amplitude and width provides feasible methods to achieve the feature size tuning of oxidation results.

5.3 Analytical process model

The above results described the dependence of oxide feature size on the pulse parameters, where the geometry of the oxide structure can be correlated to the pulse amplitude, width, and period by a function. Therefore, for a nanostructure consisting of multiple nanodots, its geometry is possible to be linked to the parameters of a series of pulses. However, little research has explored the whole picture of the relationship between pulse parameters and the geometry of expected oxidation patterns. This relationship is important for a better understanding of the nanofabrication process and achieving deterministic and high-precision control of oxidation results.

5.3.1 Single oxide dot

This work uses ultra-short pulses with a width between 15–300 μs and slow tip velocities at 200–3200 nm/s for the LAO nanofabrication. The tip displacement during the pulse width is negligible in comparison with the lateral dimension of the oxide dot. Therefore, the application of each pulse can create one nanodot and the shape of which can be assumed to be a Gaussian surface, as demonstrated in Chapter 4 and previous studies [217]. Mathematically, the profile p of a Gaussian can be described as:

$$p(\boldsymbol{r}, C, \sigma) = \frac{C}{\sigma\sqrt{2\pi}} \exp\left[-\left(\frac{\boldsymbol{r}}{\sqrt{2}\sigma}\right)^2\right] \tag{5-3}$$

where $\boldsymbol{r}$ is the polar coordinate of the oxide dot centre, C is a proportional constant and σ is the standard deviation of the Gaussian function. To reflect the oxide height h_o and diameter (FDHM) d_f, the following equations can be obtained:

$$\frac{C}{\sigma\sqrt{2\pi}} = h_o \tag{5-4}$$

$$\sqrt{2}\sigma = \frac{d_f}{2\sqrt{\ln 2}} \tag{5-5}$$

As a result, the shape of a nanodot can be expressed as a profile p as a function of oxide dot height h_o and diameter d_f:

$$p(\boldsymbol{r}, h_o, d_f) = h_o \exp\left\{-\left(\frac{\boldsymbol{r}}{0.6d_f}\right)^2\right\} \tag{5-6}$$

If we define the x axis as the tip scanning direction, and *y* is the direction perpendicular to the x direction as shown in Figure 4-1 (b), the profile p of a Gaussian surface can be expressed as:

$$p(x, y, h_o, d_f) = h_o \exp\left\{-\left(\frac{x^2+y^2}{0.36{d_f}^2}\right)\right\} \tag{5-7}$$

Based on the parametric effects, the oxide width and height can be correlated with pulse amplitude A width t, and period T. Also, the centre coordinate (x_{ci}, y_{ci}) of each nanodot can be correlated with the previous pulse periods as described in equations (4-2) and (4-3). Therefore, the profile of an oxide dot can be expressed as:

$$p(x, y, \mathrm{A}, t, T) = h_o(\mathrm{A}, t, T) \exp\left\{-\frac{\left[x - x_{ci}\left(\sum_{j=0}^{i} T_j\right)\right]^2 + \left[y - y_{ci}\left(\sum_{j=0}^{i} T_j\right)\right]^2}{0.36[w(\mathrm{A}, t, T)]^2}\right\} \tag{5-8}$$

On the basis of parameters in section 5.2, the profile of a single nanodot at (0, 0) can be modelled using Python's Matplotlib library as shown in Figure 5-4 based on the pulse amplitude of 19.2 V and width of 60 μs.

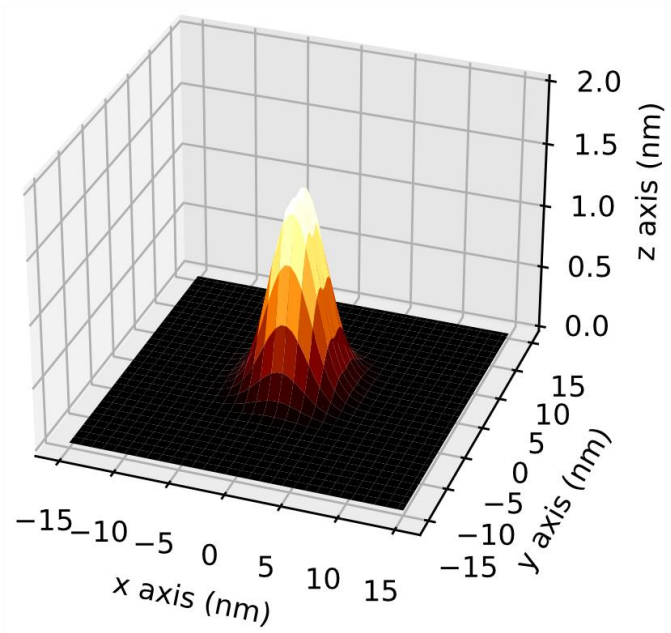

Figure 5-4. 3D profile of a single nanodot created by pulse-modulated LAO.

5.3.2 Nanostructures with multiple nanodots

For nanostructures consisting of multiple nanodots, their profiles can be deduced by the geometric assembly of multiple nanodot profiles. The profile P for a 3D nanostructure with $n+1$ nanodots can be described as:

$$P(x, y, \boldsymbol{A}, \boldsymbol{t}, \boldsymbol{T}) = \max[p_0(x, y, A_0, t_0, T_0), p_1(x, y, A_1, t_1, T_1), \dots, p_n(x, y, A_n, t_n, T_n)] \tag{5-9}$$

where p_i follows the equation (5-8); $\boldsymbol{A}, \boldsymbol{t}$, and $\boldsymbol{T}$ are the arrays of amplitudes, widths, and periods of $n+1$ pulses:

$$\boldsymbol{A} = [A_0, A_1, \dots, A_n] \tag{5-10}$$

$$\boldsymbol{t} = [t_0, t_1, \dots, t_n] \tag{5-11}$$

$$\boldsymbol{T} = [T_0, T_1, \dots, T_n] \tag{5-12}$$

(x_{ci}, y_{ci}) is the 2D centre coordinate of each oxide dot, which can be determined through the sum of the preceding pulse periods and tip scan parameters following equations (4-2) and (4-3).

In combination with the above equations, nanodot-based 3D nanostructures with profile P can be tuned through the modulation of arrays of amplitude $\boldsymbol{A}$, width $\boldsymbol{t}$, and period $\boldsymbol{T}$ of a series of pulses. It should be noted that the current process model did not consider the impact of nanodot overlapping in the y-direction on the final oxide feature sizes. Nevertheless, our experimental observations have found that this effect is negligible when the pitches along the y-axis are within the range of 5 to 50 nm, which is also the case in this thesis.

5.4 Programmable pulse generator

To achieve flexible and digital pulse modulation, this section introduces a low-cost programmable self-developed pulse generator to address the limitations of conventional functional generator. This pulse generator is based on a DOIT Arduino ESP32 DevKitV1 board, which can be programmed using the PC-based Arduino 1.8.19 IDE software. The details of the specifications can be found in Table D-1. Unlike conventional function generators, which have limited capacity for waveform files and can experience delays when receiving commands from PCs, the Arduino board can create pulses using C/C++ "Arduino programming language" and has storage of 8 KB for program files, allowing the flexible and digital modulation of a large number of pulse parameters.

The pulsed voltage signal was acquired from the DAC port (GPIO25 or GPIO26) and GND port, as shown in Figure D-1 to obtain modulated pulse amplitudes. To achieve precise modulation of the pulse period, this work employed the hardware timer *millis()* counter, which has a unit of ms and a time resolution of 8 μs, which can accurately determine the period between pulses. To comply with the requirements of a millisecond counter, the Arduino program will use an array of pulse start time T',

which can be calculated from the preceding pulse periods T through the equation (4-1).

Given that the analog reference voltage V_{ref} for ESP32 is 3.3 V, the output amplitude can swing from 0 to 3.3 V by adjusting the digital DAC output V_{dac} in the range of 0 to 255. The output voltage V_{out} can be calculated by the following equation:

$$V_{out} = \frac{V_{ref}}{255} \times V_{dac} \tag{5-13}$$

To reduce the delay caused by program update rate, the application programming interface (API) of *dac_output_voltage(DAC_CH1, Val)* was used to determine the pulse amplitude, which has an update rate of 5 μs, providing more accurate pulse waveforms than *dacWrite(DAC_CH1, Val)*. It should be noted that a minor deviation in the output voltage, typically less than 0.1 V, may occur. However, this effect should have limited influence on nanofabrication results.

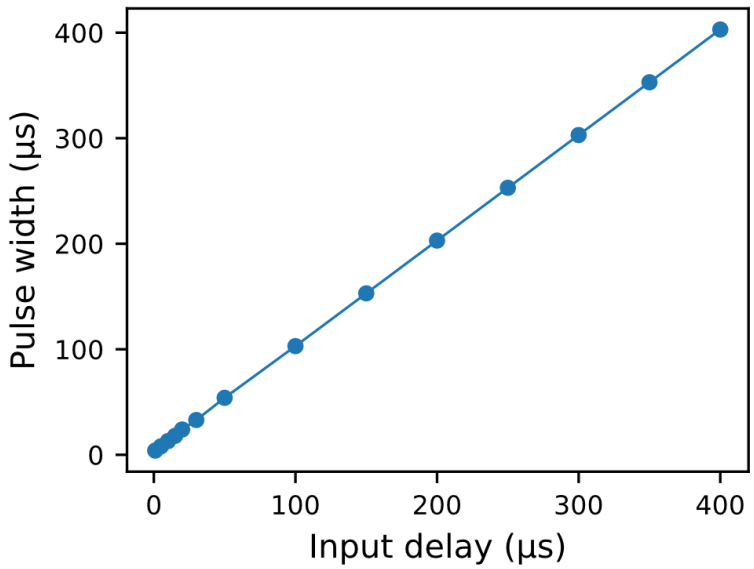

Figure 5-5. Relationship between input delay and output pulse width.

This work uses the API of *delayMicroseconds(Val)* to tune the pulse width at microseconds, Since the update rate is also at the range of microseconds, calibration

is required. The input delay and output pulse width were measured and plotted in Figure 5-5, which indicates the expected pulse width can be deduced by following equation:

$$t = t_{delay} + 3 \tag{5-14}$$

the 3 μs difference is caused by the program update rate. More details related to the Arduino program can be found in Figure D-2. With this code, it is possible to program a large number of pulses simply through the digital tuning of amplitudes, widths, and periods.

To validate the accuracy of the pulsed waveform, a digital oscilloscope (model FLUKE 192B SCOPEMETER), with up to 200 MHz bandwidth and 2.5 GS/s real-time sampling, was used to monitor the pulsed waveforms.

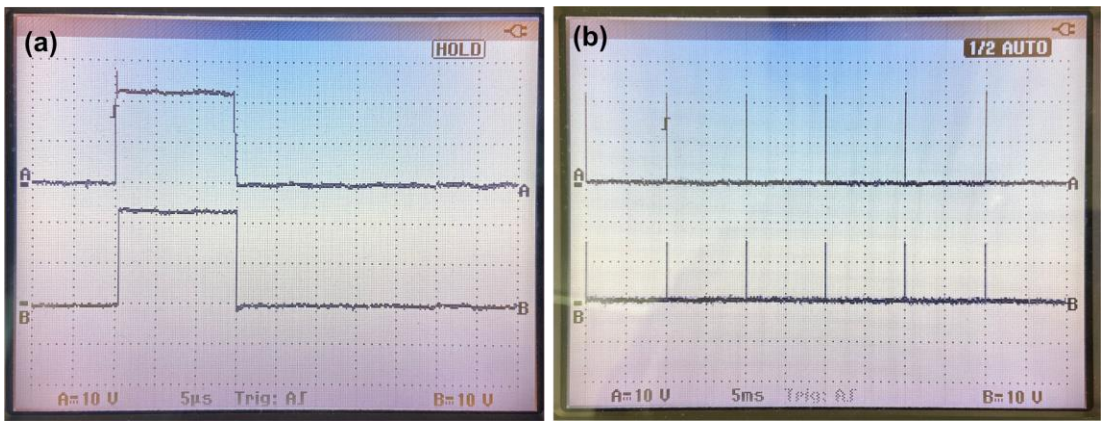

Figure 5-6. Comparisons of the pulse waveforms between the pulses generated by Arduino (channel A) and those from the Aim-TTi functional generator (channel B) in the time units of (a) 5 μs and (b) 5ms.

Through setting the same parameters on Arduino and Aim-TTi function generator with a pulse period of 10 ms, an amplitude of 1.6 V, and a width of 4 μs, resulting waveforms were monitored and shown in Figure 5-6, where channel A was connected to the Arduino and channel B was connected to the Aim-TTi functional generator.

Good agreements in amplitude, width, and period were observed between the two waveforms. Even though the pulses generated by the Arduino may have lower accuracy in achieving sharp rising and descending, their impacts became negligible after amplification by the amplifier, as demonstrated in Figure 5-7. In addition, the comparison of amplified pulses in Figure 5-7 (a) and (b) shows a good agreement in the shape of the pulsed waveform.

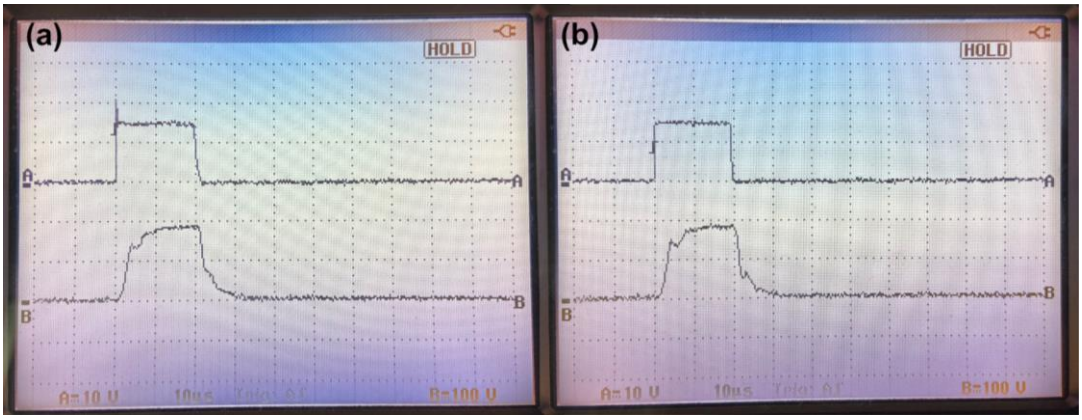

Figure 5-7. Comparison of pulsed waveforms (19 μs) before (channel A) and after (channel B) amplification for (a) pulses from Arduino and (b) pulses from Aim-TTi functional generator.

Therefore, through the program in Figure D-2, the Arduino-based pulse generator can provide the accurate output of pulsed waveforms based on the input of pulse parameters. These pulsed waveforms consisting of multiple pulses can be digitally and accurately modulated simply through programming the input parameters of pulse period $\boldsymbol{T}$, amplitude $\boldsymbol{A}$, and width $\boldsymbol{t}$, as defined in equations (5-10), (5-11), and (5-12). Through this program, the process model developed in the previous section can be digitally implemented in pulse-modulated LAO nanolithography for the fabrication of complex 3D nanostructures.

5.5 3D nanofabrication

Through the combination of the process model and programmable pulse generator, numerous pulse parameters can be modulated and utilised in the LAO nanolithography of 3D nanostructures consisting of nanodots with different heights. In this section, the evaluation of the process model will be first presented through the fabrication of gradient nanoline structures along and perpendicular to the tip scanning direction. Subsequently, the nanofabrication capability for complex 3D nanostructures will be examined by modulating a large number of pulse parameters.

5.5.1 Evaluation of process model

Firstly, the accuracy of the analytical process model was evaluated through the pulse-modulated LAO experiment. A series of pulses with modulated widths were generated and applied to the scanning tip. In both experiments, the tip was set to scanning at the speed of 200 nm/s.

A number of nanolines with different heights were fabricated in the first experiment. A schematic of the modulated pulses and tip scan route is shown in Figure 5-9. Three different pulse widths of 20, 60, and 200 μs were used when keeping pulse periods and amplitudes at 10 ms and 19.6 V, respectively. These pulses were divided into nine groups and the time intervals among them were set at 10 s by adjusting the period of the first pulse in each group. Therefore, the total period of each group of pulses equals the AFM tip scan period, allowing the creation of nanolines side by side. The pitch between sampling lines was set at 50 nm so that nanolines could be separated for measurement.

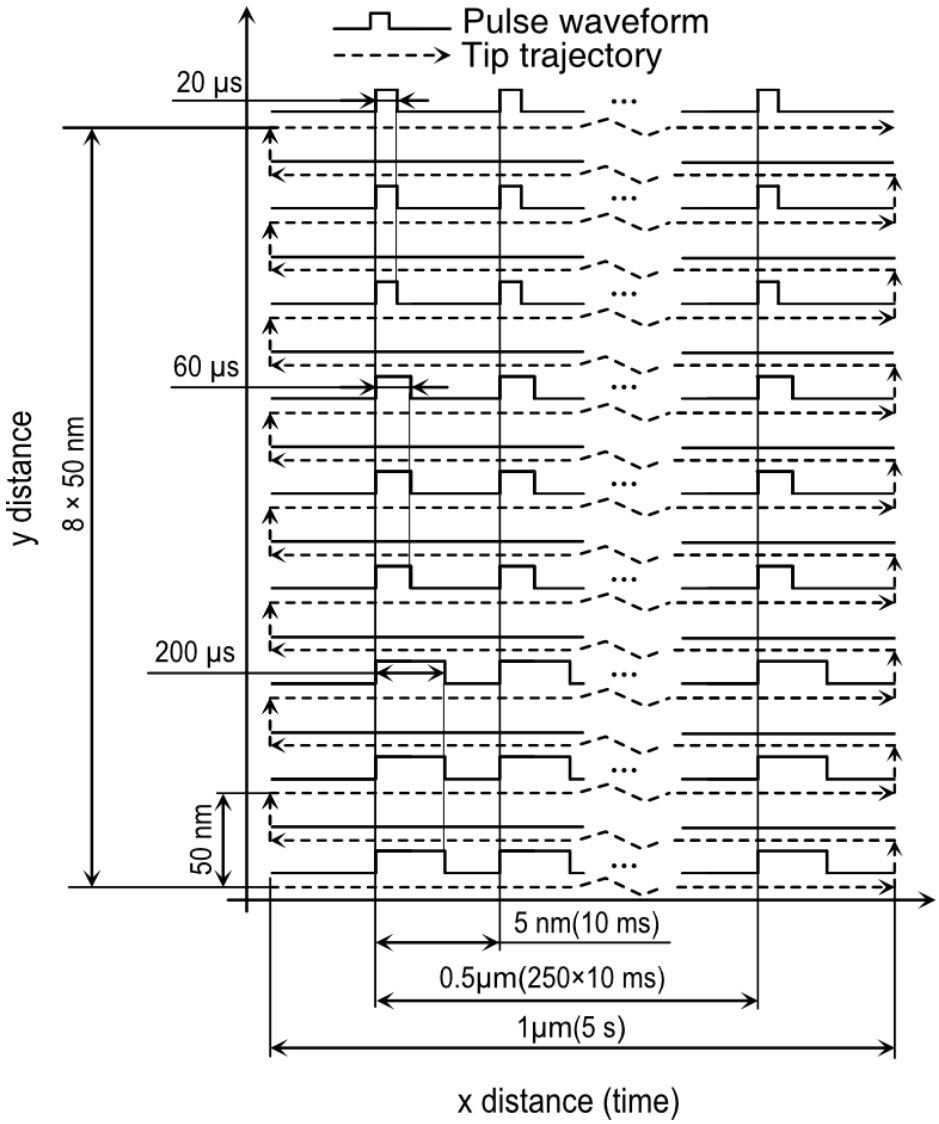

Figure 5-8. Schematic of modulated pulses and tip scanning trajectory, where solid lines represent the pulse waveform and dashed lines with arrows show the tip scan trajectory.

Figure 5-9 (a) and (b) show the predicted and fabricated nanolines. Comparisons of cross sections, heights, and widths were viewed in Figure 5-9 (c) and (d). The oxide feature sizes of fabricated nanolines suggest good agreement with the predicted nanolines with an average accuracy of 1.3 nm in line width and 0.08 nm in height, respectively, which demonstrates an accurate prediction of nanofabrication results

based on the process model. A minimum line width and height of 9.5 nm and 0.5 nm were achieved when the 20 μs pulse was used. These nanolines fabricated by pulse-modulated LAO were also demonstrated with precisions better than 6 nm (lateral) and 0.2 nm (vertical), respectively.

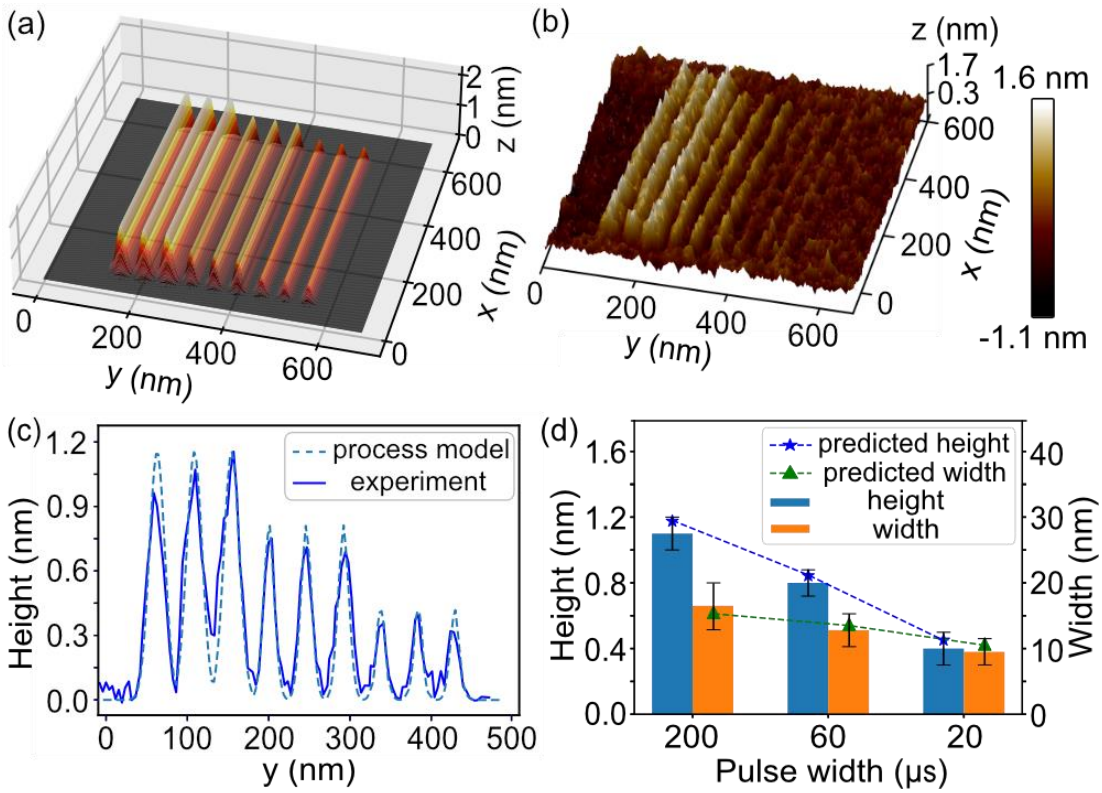

Figure 5-9. (a) Process model and (b) topographical image of nanolines; (c) cross-sectional comparison of fabricated nanolines and predicted result of process model; and (d) line widths and heights of the predicted and fabricated nanolines.

A gradient nanoline (curved surface) was fabricated in the second experiment. Figure 5-10 (a) shows a schematic of the pulses applied during the tip scanning process, where pulse periods and amplitudes were kept at 10 ms and 19.6 V, respectively. The pulse width was modulated in a triangle shape from 15 to 300 μs, as shown in Figure 5-10 (b). Through applying these pulses, a gradient nanoline with a three-dimensional curved surface (see Figure 5-10 (d)) was generated in just 2.5 s.

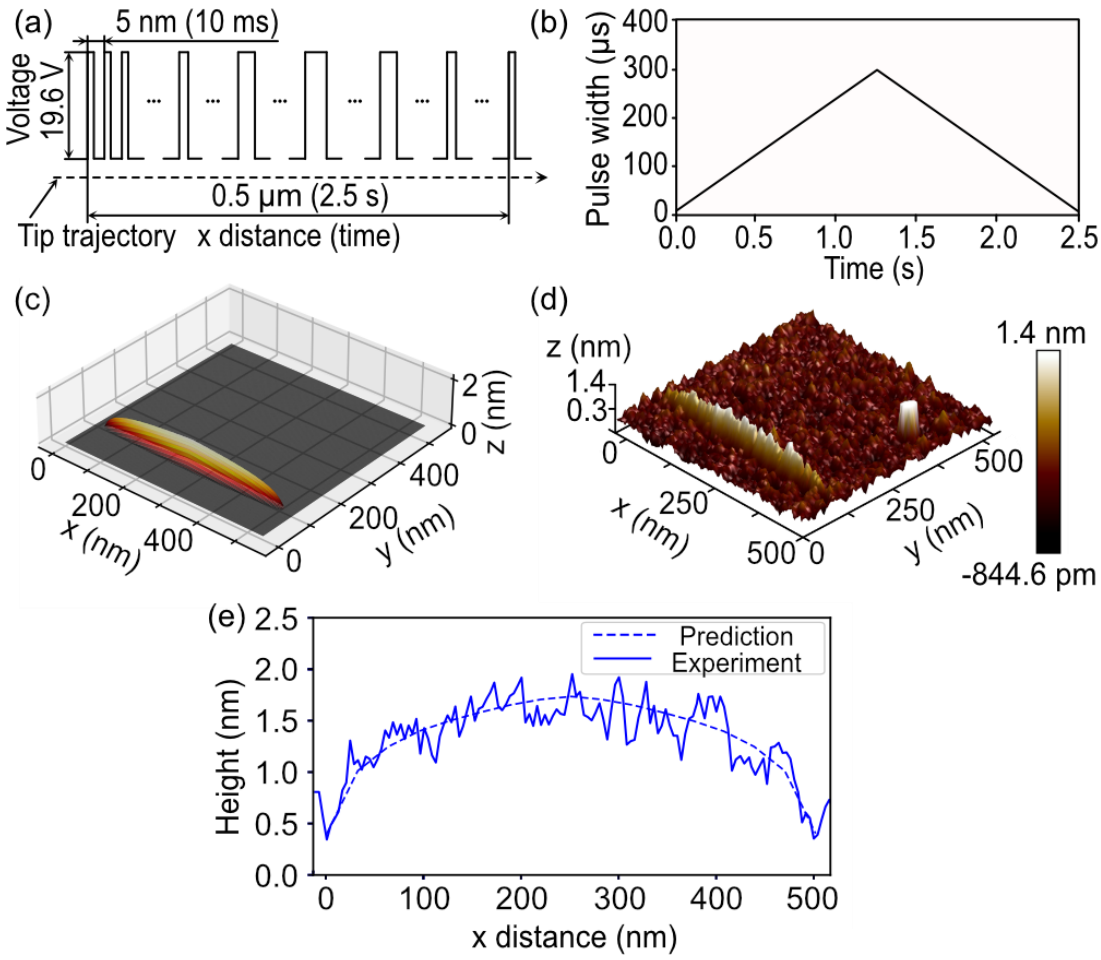

Figure 5-10. (a) Schematic of modulated pulses; (b) modulation curve of the pulse width; (c) analytical model of desired 3D nanostructure; (d) topographical image of resulting gradient lines; and (e) comparison of cross-sectional profiles between analytical process model and measured result along the gradient line.

A comparison with the analytically predicted 3D geometry (see Figure 5-10 (c)) reveals a good agreement. When the pulse width increased from 15 to 300 μs, the height of the fabricated nanostructure increased from 0.3 to 1.6 nm. At the same time, the width of the fabricated nanostructures varied from 7.9 to 21.2 nm, and the minimum width appeared to be 7.9 nm when a 15 μs pulse was applied. The results show that the proposed approach has a fabrication capability with minimum feature sizes of sub-10 nm in the lateral direction and sub-nm in height, which is also aligned

with the prediction from the analytical process model. Figure 5-10 (e) shows the cross-sectional profile along the gradient oxide line. The measured form error (P–P) of the fabricated nanostructures is less than 0.3 nm.

Based on the above results, it is demonstrated that pulse modulation provides an effective approach to control the surface gradient along and perpendicular to the tip scanning directions with nanoscale accuracy and precision for nano-line structures. The achievable minimum line width and height are at sub-10 nm and sub-nm, respectively. As pulse modulation can be easily achieved through the pulse generator independent of the AFM control system, this approach can accomplish 3D nanofabrication across the tip scan area in a single step.

5.5.2 3D nano letterings

To validate the fabrication of arbitrary 3D nanostructures, two groups of pulses were modulated, consisting of 378 and 412 pulses, respectively. The pulses were kept at the same width of 60 μs, but with modulated periods and amplitudes based on the designed positions and heights of these nanodots, aiming to create "Nano" and "p-LAO" lettering structures with different heights for each letter. Figure 5-11 (a) and (b) show the predicted and fabricated 3D nanostructures.

It is evident that the predicted model and imaging results are in good agreement. The three-dimensional features were demonstrated by the different heights for each letter, as shown in the cross-sectional views in Figure 5-11 (e) and (f). Based on the measurement of Figure 5-11 (c), from the letter ‘N’ to ‘o’, the mean heights of the fabricated nano-letters were at 1.95, 1.56, 1.22, and 0.88 nm, respectively, with a deviation of less than 0.08 nm from the predicted heights of 2, 1.6, 1.2, and 0.8 nm. The results presented in this study demonstrate that pulse-modulated LAO is an

effective and precise approach to tuning the three-dimensional shapes of arbitrary nanostructures. This method can simultaneously achieve the mapping of various nanodots across the tip scan area and the adjustment of their heights, thus enabling fully 3D nanofabrication.

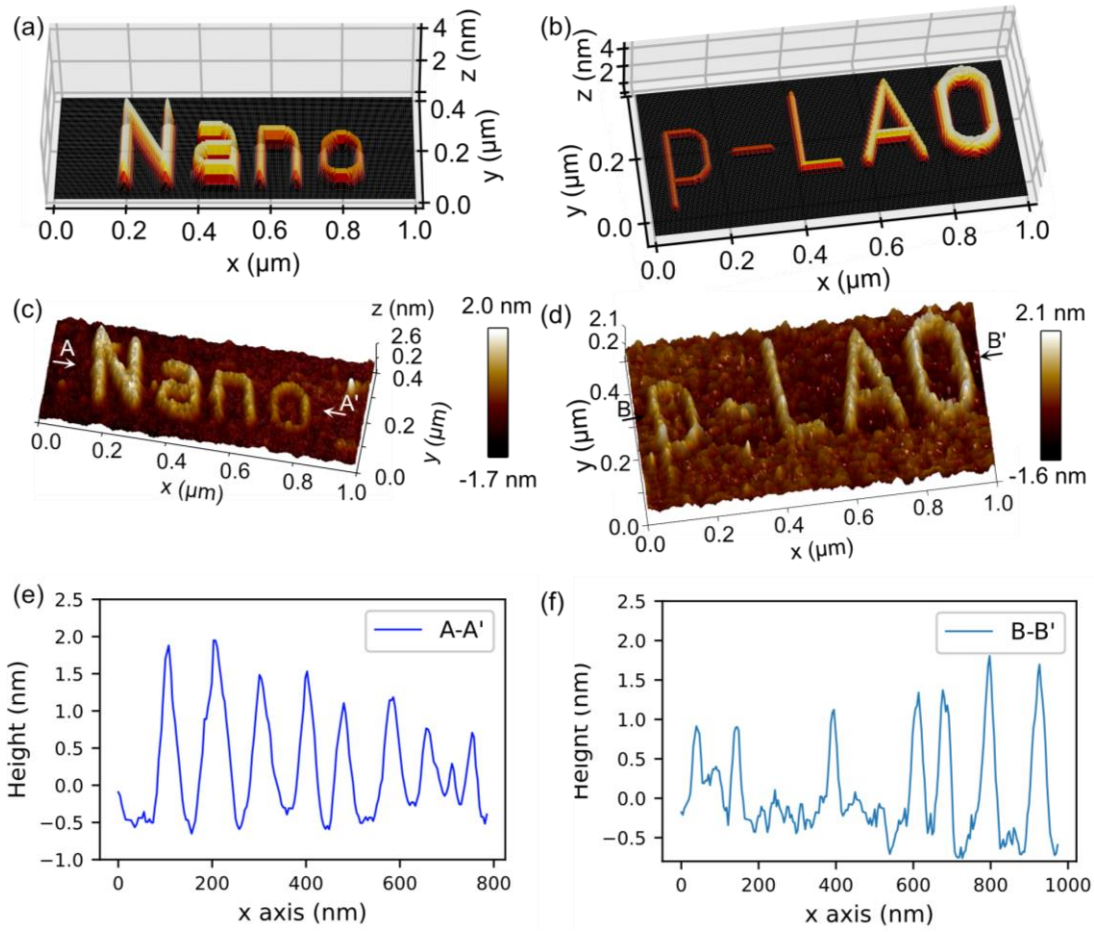

Figure 5-11. Demonstration of 3D nanofabrication results of 'Nano' and 'p-LAO' letterings with different heights for each letter through pulse-modulated LAO; (a–b) predicted geometries based on the analytical model, (c–d) topographical image of fabricated results; (e–f) cross-sectional profiles.

5.5.3 3D lens nanostructures

Nanoscale 3D lens structures have been recognised with good potential in the application of nano-optics, as demonstrated by previous studies [109,218]. To further

demonstrate the 3D nanofabrication capability of pulse-modulated LAO, validations were performed for convex and concave nanoscale lens structures with radii of several microns. During the fabrication of these nanostructures, a higher tip scan speed of 3.2 μm/s was used by setting the scan rate at 1.6 Hz for a 1 μm scan size so that nanodots along each line could be created in 0.31 s. Higher scan speeds were also considered, but experimental results showed that they could cause more pronounced under-oxidation and deviations in the fabricated nanostructures under the current experimental conditions. The pitch between scan lines was set at 5 nm, which made sure the oxide overlapped and formed continuous structures. The pulses were modulated with the same width at 60 μs but with varying amplitudes between 13 and 25 V. Pulse periods were programmed according to the designed positions of nanodots. Prior to the experiments, the parameters in the process model were calibrated through pre-tests to account for any variations of experimental conditions.

The first structure was fabricated with a convex lens shape with a radius of 3 μm. The analytical model and fabricated result are shown in Figure 5-12 (a) and (b), respectively, which were obtained by modulating the parameters of 1488 pulses. Another concave lens structure with a radius of 10 μm was created by a group of 4008 pulses. The predicted geometry and fabricated results are shown in Figure 5-13 (a) and (b), respectively. Cross sections were taken along different angles in fabricated results and plotted in Figure 5-12 (c) and Figure 5-13 (c), which confirm apparent three-dimensional curved surfaces formed by pulse-modulated LAO. The comparison with the expected surfaces (dashed line in Figure 5-12 (c) and Figure 5-13 (c)) shows a good agreement in terms of three-dimensional shapes.

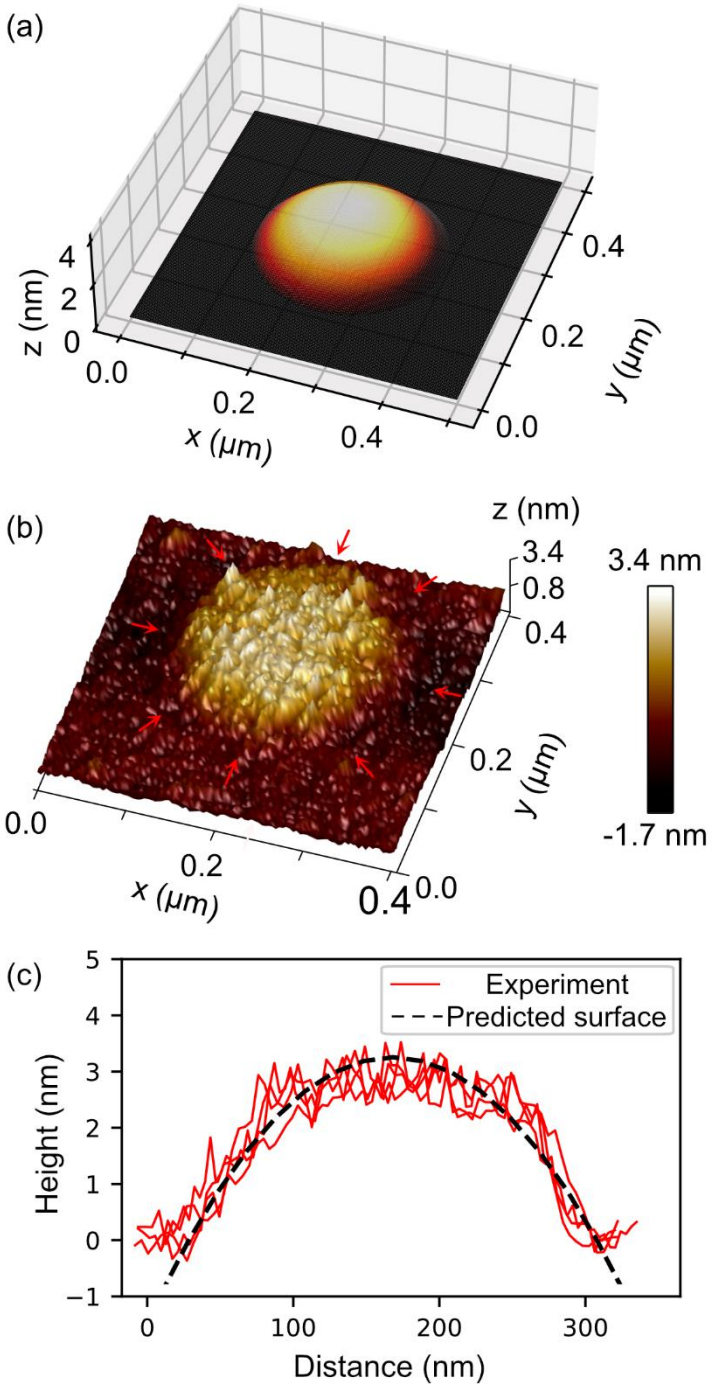

Figure 5-12. Demonstration of 3D nanofabrication results of a convex nanoscale lens structure with a radius of 3 μm through pulse-modulated LAO. (a) Analytical model; (b) topographical image; and (c) cross-sectional profiles with the designed surface represented by the dashed line.

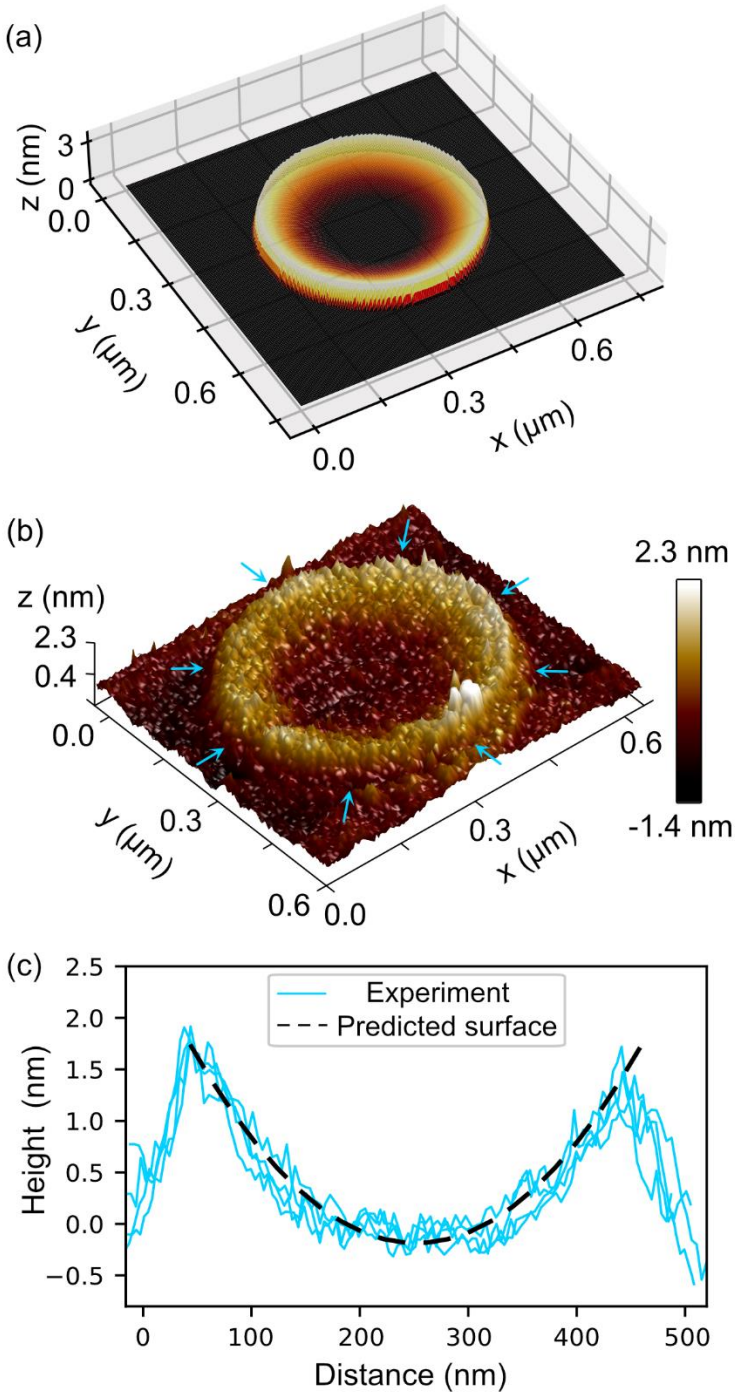

Figure 5-13. Demonstration of 3D nanofabrication results of a concave nanoscale lens structure with a radius of 10 μm through pulse-modulated LAO. (a) Analytical model; (b) topographical image; and (c) cross-sectional profiles with the designed surface represented by the dashed line.

5.5.4 Process evaluation

Pulse-modulated LAO process was further evaluated by the analysis of the nanoscale concave lens structure in Figure 5-13 (b). A detailed examination of the fabricated curved surfaces revealed an average form accuracy (P–P) of 0.4 nm compared to the predicted surface from the process model, and an average fabricated precision of the curved surface was less than 0.2 nm. Due to the use of a tip scan speed of 3.2 μm/s, the concave nanostructure was created in less than 50 s after finishing the raster scanning of 77 scan lines. These results demonstrate that pulse-modulated LAO is an efficient and accurate fabrication approach for 3D nanostructures with high precision. Based on the discussion in Chapter 2, it is concluded that LAO nanolithography has the lowest environmental requirement and start-up cost in comparison with other reviewed approaches. However, due to the inherent nature of the sequential process, current pulse-modulated LAO is still limited in throughput, which increases the cost of achieving nanofabrication on a wafer scale. Further development could focus on the use of multi-tip arrays or large-scale rolling nanoelectrodes to increase the throughput to 1 wafer/h [53]. Assuming a tool cost of $200k and consumables cost $150k/year for five years of operation, the cost of ownership (CoO) of this pulse-modulated LAO approach will be $16/wafer, which makes it very cost-competitive against current EUVL and EBL processes with CoOs of $86/wafer and $18/wafer respectively [219,220].

5.6 Summary

In conclusion, this chapter proposed an analytical process model that links the pulse parameters with the geometry of 3D nanostructures consisting of a series of nanodots. The process model is based on the experiment-observed parametric effects of pulse

period, amplitude, and width. This chapter also described the development of a programmable pulse generator that could accommodate a large number of pulses and the validation of its waveforms against those generated from a conventional pulse generator.

To validate the 3D nanofabrication capability, a series of experiments were performed. Firstly, nano-line structures with gradients along and perpendicular to the tip scanning direction were fabricated, demonstrating nanoscale accuracy and precision in 3D nanofabrication. Next, the fabrication of nanoscale letterings and lens structures validated the 3D nanofabrication capability for complex nanostructures. Topography analysis of these results indicated that pulse-modulated LAO could create nanostructures with apparent three-dimensional features. The comparison between the predicted geometries obtained by the process model and the fabricated structures demonstrated good agreement. The characterisation of the fabricated 3D curved surface, consisting of thousands of nanodots, demonstrated a sub-nm form accuracy and precision. Moreover, the approach was also proven to be highly efficient, with the complex nanostructure being created within 50 s. Therefore, this approach offers effective, accurate, and flexible control of the geometries of complex 3D nanostructures by adjusting the pulse amplitude, width, or period. Since this approach leverages the high programmability of pulse parameters to achieve 3D geometry control without resorting to complex control systems and multi-step operations, it can achieve flexible and one-step nanofabrication. Moreover, by computing the CoO for this approach, it was anticipated that enhancing its throughput would result in a more cost-effective solution for 3D nanofabrication in comparison to other methods like EUVL and EBL.

Chapter 6 Conclusions and recommendations for future work

6.1 Conclusions

This thesis presents the theoretical and experimental studies on a novel 3D nanofabrication approach based on pulse-modulated LAO. Firstly, the underlying reaction mechanisms and parametric effects in LAO were studied using ReaxFF MD simulations. Then, a novel pulse-modulated LAO nanolithography approach was proposed, accompanied by the development of an analytical process model and a testing platform. The proposed approach was then experimentally validated, demonstrating its flexibility, accuracy, precision, and efficiency in fabricating various 3D nanostructures. The main conclusions can be drawn as follows:

- Through the ReaxFF MD simulation, the dominant reaction during the LAO process was found to be the consumption of H_2O and the creation of H_3O^+ in the water layer, and the creation of Si–O–Si bonds under the silicon surface. However, the surface chemical composition did not exhibit significant changes during the LAO process with a mixture of Si–H, Si–H_2, Si–O–H, H_2O–Si, and Si–O–Si bonds, similar to the results obtained from surface passivation. The Si–O–H and H_2O–Si on the silicon surface appeared to serve as intermediate products during the reaction. Compared with the surface passivation process, the application of an electric field could apparently enhance the oxidation rate.

- The reaction rate of LAO can be increased by increasing both the electric field strength and humidity levels. However, the enhanced oxidations were achieved under different mechanisms. Through the analysis of the number and

distribution of Si–O–Si bonds, the diffusion rate of O atoms towards the depth direction increased with the increasing electric field strength, leading to an increased oxidation rate. In the study on the dependence of humidity, it was found that a higher humidity leads to more H_2O available in the water layer, enhancing the oxidation reaction and forming more Si–O–Si bonds near the silicon surface. In both simulation results, it was found that the surface composition of Si–H, Si–H_2, Si–O–H, and H_2O–Si bonds were not apparently affected by different electric fields and humidity.

- A pulse-modulated LAO nanolithography approach was proposed, aiming to achieve flexible, cost-effective, and efficient 3D nanofabrication. To implement this approach, a tapping mode AFM with a sharp probe was used in combination with a function generator and an amplifier. This setup enabled high-precision control of tip scanning, post-imaging analysis, and localized oxidation. The feasibility of this approach was validated through the fabrication of several simple nanostructures, which demonstrated the achievable minimum feature sizes of sub-10 nm (lateral) and sub-nm (vertical).
- An analytical process model was developed to describe the pulse-modulated LAO nanolithography process proposed in this work. The model assumed the nanostructures fabricated through LAO as an assembly of arrays of nanodots. This allowed the geometry of 3D nanostructures to be linked with the input pulse periods, amplitudes and widths. The relevant parameters can be determined through thorough parametric studies.

- A fully programmable functional generator based on an Arduino ESP32 board was developed. Further validation confirmed its effectiveness and accuracy by comparing its waveforms with those of a conventional pulse generator.

- By using the process model and programmable pulse generator, the pulse-modulated LAO was found to be effective in the geometric control of 3D nanostructures with minimum line width at sub-10 nm and height at sub-nm. In addition, this technique was shown to be capable of producing complex nanostructures through the fabrication of arbitrary lettering and nanoscale lens structures for nano-optics applications. These results demonstrated apparent three-dimensional features and were in good agreement with the predicted geometry from the process model. The form accuracy and precision of a fabricated three-dimensional curved surface were further evaluated, demonstrating sub-nm average accuracy and precision. The use of a higher scan rate could increase the nanofabrication efficiency, as demonstrated by the fabrication of nanoscale lens structures consisting of four thousand nanodots within 50 seconds.

6.2 Contribution to knowledge

The contribution to knowledge in this thesis can be summarised as follow:

- Development of a new flexible and one-step pulse-modulated LAO nanolithography approach for 3D nanostructures, with the three-dimensional geometry controlled by programmable pulse modulation. With the support of a validated process model and optimised experimental setups, the new proposed nanofabrication process can obtain minimum features sizes of sub-

10 nm (lateral) and sub-nm (vertical), respectively, enabling the 3D nanofabrication in areas smaller than 1 μm^2.

- Establishment of a test platform for pulse-modulated LAO nanolithography. The use of a fully programmable pulse generator allows the digital programming of parameters of thousands of pulses, which enables the fabrication of complex 3D nanostructures with arbitrary shapes. Since the pulse parameters can be flexibly and precisely programmed, the pulse-modulated LAO can efficiently achieve 3D nanofabrication with high precision.

- An in-depth understanding of reaction mechanisms in the LAO process. The ReaxFF MD simulation results demonstrated that the LAO process is dominated by the consumption of H_2O in the water layer and the creation of Si–O–Si bonds within the oxide film. Moreover, the simulation results revealed that the electric field and humidity can both enhance the reaction. Specifically, the increased electric field promotes the diffusion of Si–O–Si bonds beneath the surface, whereas increased humidity accelerates the main reaction at the surface.

6.3 Recommendation for future work

This thesis introduced the ReaxFF MD simulation for the LAO process, which provided atomistic insights into the underlying reaction mechanisms, and proposed a flexible, cost-effective, and one-step 3D nanofabrication approach that was further validated. However, there are several limitations that hinder the wide application of this approach, such as the lack of understanding on oxidation growth, and the challenges in achieving nanofabrication with higher precision, aspect ratio and scalability. Therefore, the recommendations for future research are:

- The ReaxFF force field used in this thesis has been validated with reasonable accuracy in the description of silicon-water interaction on silicon surfaces. However, its accuracy in describing bulk silicon dioxide properties has not been testified, which may limit the application of this force field to surface oxidation over longer simulation time scales. A new ReaxFF force field could be developed to allow more accurate simulation.

- To enhance precision even further, it is necessary to optimise the experimental conditions, with a particular focus on humidity control. The simulation study conducted in this work has demonstrated the significant influence of humidity on the oxidation process. Therefore, future research should aim to develop a closed chamber that incorporates an AFM system with humidity control inlets. This advancement is expected to enable high-quality patterning and improve overall results.

- To achieve nanostructures with higher aspect ratio, it may be necessary to conduct simulation and experimental research on novel substrate materials and/or anodic solutions that can be used in the LAO process. This could help to find other material-anodic solution combinations that enable higher oxidation growth rates, leading to the creation of nanoproducts with higher performance.

- Faradaic current detection can be added to the pulse-modulated LAO nanolithography approach. Since the Faradaic current directly reflects the oxidation growth, this would allow *in-situ* monitoring of the oxidation process during the LAO process. This detection would enable a deeper understanding of the reaction process, possibly enabling the development of the process

model with higher accuracy. This, in turn, could lead to the development of feedback-controlled LAO processes with improved precision and accuracy.

- In order to extend the range of nanofabrication, a high-precision motion platform must be developed. In addition, the development of multi-tip arrays or nanoelectrode tools can further increase the patterning scale and efficiency of this process.

- The good tunability of the pulsed voltage demonstrated through this thesis makes this method potentially applicable to other bias-induced nanofabrication techniques, such as electrochemical nanomachining [221,222], local electrochemical oxidation [223], bias-induced deposition processes [224], and local crystallisation [225]. Further experimental investigations can be conducted to explore the application of pulse modulation in enhancing the flexibility and efficiency of these nanofabrication techniques.

Appendices

Appendix A Essential specification of Aim-TTi TGF4042 pulse generator

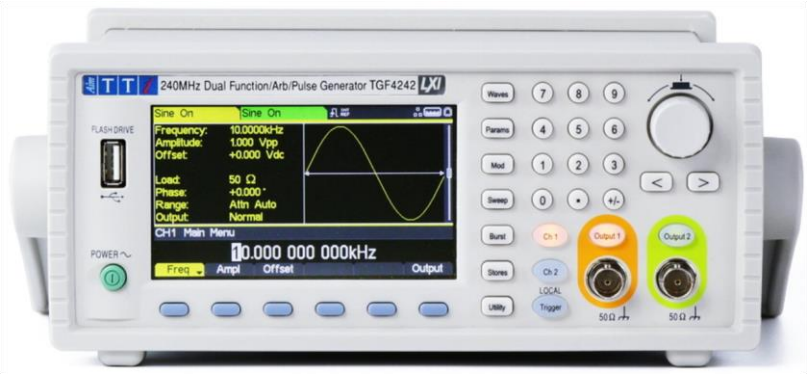

Figure A-1. Schematic of the Aim-TTi TGF4042 pulse generator.

Table A-1. Partial specifications of Aim-TTi TGF4042 pulse generator

Output type	Parameters	Values
Pulse output	Frequency resolution	1 mHz, 11 digits
	Frequency range	1 mHz to 25 MHz
	Vertical bits	Sample rate 14 bits / 400 Msa/s
	Output level, peak to peak (P–P)	10 mV to 10 V
	Width range	20 ns to 999.99999998 s
	Width resolution	100 ps
	Edge speed	3 ns to 800 s
	Rise and fall times	8 ns to 799.999999984 s
	Jitter	< 30 ps (cycle to cycle)
	Waveforms memory size	8192 points
	Sampling rate	400 Msa/s
Arbitrary output	Frequency range	1 μHz to 2 MHz
	Frequency resolution	1 μHz, 14 digits
	Vertical resolution	14 bit

Appendix B Essential specification of CoreMorrow E01.A2 power amplifier

Figure B-1. Schematic of CoreMorrow E01.A2 power amplifier.

Table B-1. Specifications of CoreMorrow E01.A2 power amplifier.

Parameters	Values
Type	E01.A2
Channels	2
Input range (V)	-2.5~7.5
Output voltage (V)	-500~1500
Output ripple	50mVp-p(@1μF)
Stability	<0.1%F.S./8hours
Input impedance (kΩ)	100
Bandwidth (kHz)	3
Small signal bandwidth (kHz)	10

Appendix C Essential specification of silicon wafer

Table C-1. Specifications of the silicon wafer.

Specifications	Values
Diameter	100 ± 0.3 mm
Thickness	525 μm
Type	P
Dopant	Boron
Crystal orientation	100 ± 0.5°
Thickness tolerance	± 20 μm
Resistivity	1–10 Ω·cm
Surface Roughness	Ra: < 0.3 nm
Polish	Double side polish

Appendix D Essential specification of DOIT Arduino ESP32 DevKitV1

Table D-1. Partial specifications of DOIT Arduino ESP32 DevKitV1

Parameters	Values
Processor	Tensilica Xtensa Dual-Core 32-bit LX6 microprocessor
Frequency	240 MHz
SRAM	520 KB
ROM	448 KB
RTC fas SRAM	8 KB

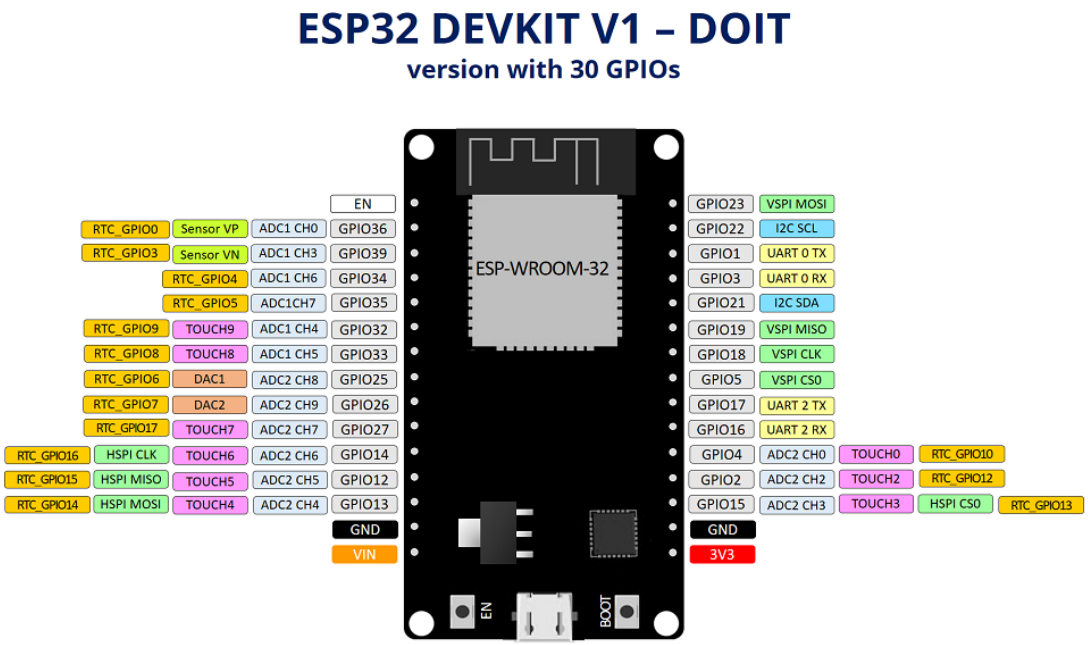

Figure D-1. Pinout of ESP32 DevKit V1.

```
long double per[] = {T'1,T'2,...,T'n};  //in milliseconds
long double amp[] = {A1,A2,...,An};     //in volts
long double wid[] = {t1,t2,...,tn};     //in microseconds

#define DAC_CH1 25
void setup() {
  Serial.begin(9600);
  pinMode(DAC_CH1, OUTPUT);
  dac_output_enable(DAC_CH1);
}
void loop() {
   while (millis()>=per[i]){
    dac_output_voltage(DAC_CH1, int(amp[i]*255/3.3));
    delayMicroseconds(wid[i]-3);
    dac_output_voltage(DAC_CH1, 0);
    i+=1;
    Serial.println(millis());
  }
}
```

Figure D-2. Arduino code for the fully programmable pulse generator.

References

[1] F.Z. Fang, X.D. Zhang, W. Gao, Y.B. Guo, G. Byrne, H.N. Hansen, Nanomanufacturing—Perspective and applications, CIRP Ann. 66 (2017) 683–705. https://doi.org/10.1016/j.cirp.2017.05.004.

[2] B.J. Wiley, D. Qin, Y. Xia, Nanofabrication at High Throughput and Low Cost, ACS Nano. 4 (2010) 3554–3559. https://doi.org/10.1021/nn101472p.

[3] D. Wu, N. S. Rajput, X.C. Luo, Nanoimprint Lithography - the Past, the Present and the Future, Curr. Nanosci. 12 (2016) 712–724. https://doi.org/10.2174/1573413712666160530120432.

[4] F.Z. Fang, N. Zhang, D.M. Guo, K. Ehmann, B. Cheung, K. Liu, K. Yamamura, Towards atomic and close-to-atomic scale manufacturing, Int. J. Extreme Manuf. 1 (2019) 012001. https://doi.org/10.1088/2631-7990/ab0dfc.

[5] R.Md.M. Hasan, X.C. Luo, Promising Lithography Techniques for Next-Generation Logic Devices, Nanomanufacturing Metrol. 1 (2018) 67–81. https://doi.org/10.1007/s41871-018-0016-9.

[6] P.T. Mathew, B.J. Rodriguez, F.Z. Fang, Atomic and Close-to-Atomic Scale Manufacturing: A Review on Atomic Layer Removal Methods Using Atomic Force Microscopy, Nanomanufacturing Metrol. 3 (2020) 167–186. https://doi.org/10.1007/s41871-020-00067-2.

[7] Y.K. Ryu, R. Garcia, Advanced oxidation scanning probe lithography, Nanotechnology. 28 (2017) 142003. https://doi.org/10.1088/1361-6528/aa5651.

[8] Y. Chen, Z. Shu, S. Zhang, P. Zeng, H. Liang, M. Zheng, H. Duan, Sub-10 nm fabrication: methods and applications, Int. J. Extreme Manuf. 3 (2021) 032002. https://doi.org/10.1088/2631-7990/ac087c.

[9] F.Z. Fang, Atomic and close-to-atomic scale manufacturing: perspectives and measures, Int. J. Extreme Manuf. 2 (2020) 030201. https://doi.org/10.1088/2631-7990/aba495.

[10] D.M. Eigler, E.K. Schweizer, Positioning single atoms with a scanning tunnelling microscope, Nature. 344 (1990) 524–526. https://doi.org/10.1038/344524a0.

[11] K.-F. Braun, K.-H. Rieder, Engineering Electronic Lifetimes in Artificial Atomic Structures, Phys. Rev. Lett. 88 (2002) 096801. https://doi.org/10.1103/PhysRevLett.88.096801.

[12] M.F. Crommie, C.P. Lutz, D.M. Eigler, Confinement of electrons to quantum corrals on a metal surface, Science. 262 (1993) 218–220. https://doi.org/10.1126/science.262.5131.218.

[13] P. Zeppenfeld, C.P. Lutz, D.M. Eigler, Manipulating atoms and molecules with a scanning tunneling microscope, Ultramicroscopy. 42–44 (1992) 128–133. https://doi.org/10.1016/0304-3991(92)90256-J.

[14] L. Bartels, G. Meyer, K.-H. Rieder, Controlled vertical manipulation of single CO molecules with the scanning tunneling microscope: A route to chemical contrast, Appl. Phys. Lett. 71 (1997) 213–215. https://doi.org/10.1063/1.119503.

[15] T.-C. Shen, C. Wang, G.C. Abeln, J.R. Tucker, J.W. Lyding, Ph. Avouris, R.E. Walkup, Atomic-scale desorption through electronic and vibrational excitation

mechanisms, Science. 268 (1995) 1590–1592. https://doi.org/10.1126/science.268.5217.1590.

[16] G. Dujardin, R.E. Walkup, Ph. Avouris, Dissociation of individual molecules with electrons from the tip of a scanning tunneling microscope, Science. 255 (1992) 1232–1235. https://doi.org/10.1126/science.255.5049.1232.

[17] L. Bartels, G. Meyer, K.-H. Rieder, Basic steps of lateral manipulation of single atoms and diatomic clusters with a scanning tunneling microscope tip, Phys. Rev. Lett. 79 (1997) 697–700. https://doi.org/10.1103/PhysRevLett.79.697.

[18] D.M. Eigler, C.P. Lutz, W.E. Rudge, An atomic switch realized with the scanning tunnelling microscope, Nature. 352 (1991) 600–603. https://doi.org/10.1038/352600a0.

[19] J.N. Randall, J.H.G. Owen, J. Lake, R. Saini, E. Fuchs, M. Mahdavi, S.O.R. Moheimani, B.C. Schaefer, Highly parallel scanning tunneling microscope based hydrogen depassivation lithography, J. Vac. Sci. Technol. B. 36 (2018) 06JL05. https://doi.org/10.1116/1.5047939.

[20] J.W. Lyding, T.C. Shen, J.S. Hubacek, J.R. Tucker, G.C. Abeln, Nanoscale patterning and oxidation of H-passivated Si(100)-2×1 surfaces with an ultrahigh vacuum scanning tunneling microscope, Appl. Phys. Lett. 64 (1994) 2010–2012. https://doi.org/10.1063/1.111722.

[21] J.B. Ballard, T.W. Sisson, J.H.G. Owen, W.R. Owen, E. Fuchs, J. Alexander, J.N. Randall, J.R. Von Ehr, Multimode hydrogen depassivation lithography: A method for optimizing atomically precise write times, J. Vac. Sci. Technol. B Nanotechnol. Microelectron. Mater. Process. Meas. Phenom. 31 (2013) 06FC01. https://doi.org/10.1116/1.4823756.

[22] M.A. Walsh, M.C. Hersam, Atomic-scale templates patterned by ultrahigh vacuum scanning tunneling microscopy on silicon, Annu. Rev. Phys. Chem. 60 (2009) 193–216. https://doi.org/10.1146/annurev.physchem.040808.090314.

[23] B.N.J. Persson, Inelastic vacuum tunneling, Phys. Scr. 38 (1988) 282–290. https://doi.org/10.1088/0031-8949/38/2/034.

[24] N. Kobayashi, K. Hirose, M. Tsukada, First-principles study of Na atom transfer induced by the tip of a STM, Surf. Sci. 348 (1996) 299–304. https://doi.org/10.1016/0039-6028(95)00949-3.

[25] U.J. Quaade, K. Stokbro, C. Thirstrup, F. Grey, Mechanism of single atom switch on silicon, Surf. Sci. 415 (1998) L1037–L1045. https://doi.org/10.1016/S0039-6028(98)00560-3.

[26] G.D. Nguyen, L. Liang, Q. Zou, M. Fu, A.D. Oyedele, B.G. Sumpter, Z. Liu, Z. Gai, K. Xiao, A.-P. Li, 3D Imaging and Manipulation of Subsurface Selenium Vacancies in PdSe 2, Phys. Rev. Lett. 121 (2018) 086101. https://doi.org/10.1103/PhysRevLett.121.086101.

[27] Y. Xie, Q. Liu, P. Zhang, W. Zhang, S. Wang, M. Zhuang, Y. Li, F. Gan, J. Zhuang, Reliable lateral and vertical manipulations of a single Cu adatom on a Cu(111) surface with multi-atom apex tip: semiempirical and first-principles simulations, Nanotechnology. 19 (2008) 335710. https://doi.org/10.1088/0957-4484/19/33/335710.

[28] P. Liu, M. Wu, H. Liu, F. Lu, W.-H. Wang, K. Cho, First-Principle Prediction on STM Tip Manipulation of Ti Adatom on Two-Dimensional Monolayer YBr_3, Scanning. 2019 (2019) 1–7. https://doi.org/10.1155/2019/5434935.

[29] N. Oyabu, Ó. Custance, I. Yi, Y. Sugawara, S. Morita, Mechanical Vertical Manipulation of Selected Single Atoms by Soft Nanoindentation Using Near Contact Atomic Force Microscopy, Phys. Rev. Lett. 90 (2003) 176102. https://doi.org/10.1103/PhysRevLett.90.176102.

[30] S. Kawai, H. Kawakatsu, Mechanical atom manipulation with small amplitude dynamic force microscopy, Appl. Phys. Lett. 89 (2006) 18–21. https://doi.org/10.1063/1.2220539.

[31] Y. Sugimoto, P. Pou, O. Custance, P. Jelinek, M. Abe, R. Perez, S. Morita, Complex patterning by vertical interchange atom manipulation using atomic force microscopy, Science. 322 (2008) 413–417. https://doi.org/10.1126/science.1160601.

[32] Y. Sugimoto, M. Abe, S. Hirayama, N. Oyabu, O. Custance, S. Morita, Atom inlays performed at room temperature using atomic force microscopy, Nat. Mater. 4 (2005) 156–159. https://doi.org/10.1038/nmat1297.

[33] Y. Sugimoto, P. Jelinek, P. Pou, M. Abe, S. Morita, R. Perez, O. Custance, Mechanism for Room-Temperature Single-Atom Lateral Manipulations on Semiconductors using Dynamic Force Microscopy, Phys. Rev. Lett. 98 (2007) 106104. https://doi.org/10.1103/PhysRevLett.98.106104.

[34] B. Enkhtaivan, Y. Sugimoto, A. Oshiyama, First-principles study of lateral atom manipulation assisted by structural relaxation of a scanning tip apex, Phys. Rev. B. 96 (2017) 1–7. https://doi.org/10.1103/PhysRevB.96.155417.

[35] J. Bamidele, S.H. Lee, Y. Kinoshita, R. Turanský, Y. Naitoh, Y.J. Li, Y. Sugawara, I. Štich, L. Kantorovich, Vertical atomic manipulation with dynamic

atomic-force microscopy without tip change via a multi-step mechanism, Nat. Commun. 5 (2014) 1–7. https://doi.org/10.1038/ncomms5476.

[36] E. Albisetti, A. Calò, A. Zanut, X. Zheng, G.M. De Peppo, E. Riedo, Thermal scanning probe lithography, Nat. Rev. Methods Primer. 2 (2022) 32. https://doi.org/10.1038/s43586-022-00110-0.

[37] S.T. Howell, A. Grushina, F. Holzner, J. Brugger, Thermal scanning probe lithography—a review, Microsyst. Nanoeng. 6 (2020) 1–24. https://doi.org/10.1038/s41378-019-0124-8.

[38] G. Liu, M. Hirtz, H. Fuchs, Z. Zheng, Development of Dip-Pen Nanolithography (DPN) and its derivatives, Small. 15 (2019) 1900564. https://doi.org/10.1002/smll.201900564.

[39] T. Michels, I.W. Rangelow, Review of scanning probe micromachining and its applications within nanoscience, Microelectron. Eng. 126 (2014) 191–203. https://doi.org/10.1016/j.mee.2014.02.011.

[40] P. Fan, J. Gao, H. Mao, Y. Geng, Y. Yan, Y. Wang, S. Goel, X.C. Luo, Scanning Probe Lithography: State-of-the-Art and Future Perspectives, Micromachines. 13 (2022) 228. https://doi.org/10.3390/mi13020228.

[41] R. Garcia, A.W. Knoll, E. Riedo, Advanced scanning probe lithography, Nat. Nanotechnol. 9 (2014) 577–587. https://doi.org/10.1038/nnano.2014.157.

[42] Y. Krivoshapkina, M. Kaestner, I.W. Rangelow, Tip-based nanolithography methods and materials, in: Front. Nanosci., Elsevier, 2016: pp. 497–542. https://doi.org/10.1016/B978-0-08-100354-1.00015-6.

[43] J.A. Dagata, J. Schneir, H.H. Harary, C.J. Evans, M.T. Postek, J. Bennett, Modification of hydrogen-passivated silicon by a scanning tunneling

microscope operating in air, Appl. Phys. Lett. 56 (1990) 2001–2003. https://doi.org/10.1063/1.102999.

[44] H. Sugimura, T. Yamamoto, N. Nakagiri, M. Miyashita, T. Onuki, Maskless patterning of silicon surface based on scanning tunneling microscope tip-induced anodization and chemical etching, Appl. Phys. Lett. 65 (1994) 1569–1571. https://doi.org/10.1063/1.112917.

[45] N. Kurra, R.G. Reifenberger, G.U. Kulkarni, Nanocarbon-Scanning Probe Microscopy Synergy: Fundamental Aspects to Nanoscale Devices, ACS Appl. Mater. Interfaces. 6 (2014) 6147–6163. https://doi.org/10.1021/am500122g.

[46] F. Hui, C. Wen, S. Chen, E. Koren, R. Dechter, D. Lewis, M. Lanza, Emerging Scanning Probe–Based Setups for Advanced Nanoelectronic Research, Adv. Funct. Mater. 30 (2020) 1902776. https://doi.org/10.1002/adfm.201902776.

[47] R. Tominov, V. Avilov, Z. Vakulov, D. Khakhulin, O. Ageev, I. Valov, V. Smirnov, Forming-Free Resistive Switching of Electrochemical Titanium Oxide Localized Nanostructures: Anodization, Chemical Composition, Nanoscale Size Effects, and Memristive Storage, Adv. Electron. Mater. 8 (2022) 2200215. https://doi.org/10.1002/aelm.202200215.

[48] C.R. Peiris, S. Ferrie, S. Ciampi, W.D.A. Rickard, N. Darwish, Memristor Arrays Formed by Reversible Formation and Breakdown of Nanoscale Silica Layers on Si–H Surfaces, ACS Appl. Nano Mater. 5 (2022) 6609–6617. https://doi.org/10.1021/acsanm.2c00663.

[49] R.K. Puddy, C.J. Chua, M.R. Buitelaar, Transport spectroscopy of a graphene quantum dot fabricated by atomic force microscope nanolithography, Appl. Phys. Lett. 103 (2013) 183117. https://doi.org/10.1063/1.4828663.

[50] F.M. Espinosa, Y.K. Ryu, K. Marinov, D. Dumcenco, A. Kis, R. Garcia, Direct fabrication of thin layer MoS $_2$ field-effect nanoscale transistors by oxidation scanning probe lithography, Appl. Phys. Lett. 106 (2015) 103503. https://doi.org/10.1063/1.4914349.

[51] M. Pea, M. De Seta, L. Di Gaspare, L. Persichetti, A.M. Scaparro, V. Miseikis, C. Coletti, A. Notargiacomo, Submicron Size Schottky Junctions on As-Grown Monolayer Epitaxial Graphene on Ge(100): A Low-Invasive Scanned-Probe-Based Study, ACS Appl. Mater. Interfaces. 11 (2019) 35079–35087. https://doi.org/10.1021/acsami.9b09681.

[52] A Notargiacomo, V Foglietti, E Cianci, G Capellini, M Adami, P Faraci, F Evangelisti, C Nicolini, Atomic force microscopy lithography as a nanodevice development technique*, Nanotechnology. 10 (1999) 458. https://doi.org/10.1088/0957-4484/10/4/317.

[53] R.Md.M. Hasan, X.C. Luo, J.N. Sun, Rolling Nanoelectrode Lithography, Micromachines. 11 (2020) 656. https://doi.org/10.3390/mi11070656.

[54] K. Ivanova, Y. Sarov, Tzv. Ivanov, A. Frank, J. Zöllner, Ch. Bitterlich, U. Wenzel, B.E. Volland, S. Klett, I.W. Rangelow, P. Zawierucha, M. Zielony, T. Gotszalk, D. Dontzov, W. Schott, N. Nikolov, M. Zier, B. Schmidt, W. Engl, T. Sulzbach, I. Kostic, Scanning proximal probes for parallel imaging and lithography, J. Vac. Sci. Technol. B Microelectron. Nanometer Struct. 26 (2008) 2367–2373. https://doi.org/10.1116/1.2990789.

[55] M. Kaestner, M. Hofer, I.W. Rangelow, Nanolithography by scanning probes on calixarene molecular glass resist using mix-and-match lithography, J.

MicroNanolithography MEMS MOEMS. 12 (2013) 031111. https://doi.org/10.1117/1.JMM.12.3.031111.

[56] I.W. Rangelow, T. Ivanov, Y. Sarov, A. Schuh, A. Frank, H. Hartmann, J.-P. Zöllner, D.L. Olynick, V. Kalchenko, Nanoprobe maskless lithography, in: D.J.C. Herr (Ed.), Proc SPIE 7637, San Jose, California, 2010: p. 76370V. https://doi.org/10.1117/12.852265.

[57] D. Stiévenard, B. Legrand, Silicon surface nano-oxidation using scanning probe microscopy, Prog. Surf. Sci. 81 (2006) 112–140. https://doi.org/10.1016/j.progsurf.2006.01.003.

[58] T. Hattori, Y. Ejiri, K. Saito, M. Yasutake, Fabrication of nanometer-scale structures using atomic force microscope with conducting probe, J. Vac. Sci. Technol. Vac. Surf. Films. 12 (1994) 2586–2590. https://doi.org/10.1116/1.579062.

[59] F. Marchi, Growth of silicon oxide on hydrogenated silicon during lithography with an atomic force microscope, J. Vac. Sci. Technol. B Microelectron. Nanometer Struct. 16 (1998) 2952. https://doi.org/10.1116/1.590325.

[60] P. Avouris, T. Hertel, R. Martel, Atomic force microscope tip-induced local oxidation of silicon: kinetics, mechanism, and nanofabrication, Appl. Phys. Lett. 71 (1997) 285–287. https://doi.org/10.1063/1.119521.

[61] A.E. Gordon, Mechanisms of surface anodization produced by scanning probe microscopes, J. Vac. Sci. Technol. B Microelectron. Nanometer Struct. 13 (1995) 2805. https://doi.org/10.1116/1.588270.

[62] P.A. Fontaine, E. Dubois, D. Stiévenard, Characterization of scanning tunneling microscopy and atomic force microscopy-based techniques for nanolithography

on hydrogen-passivated silicon, J. Appl. Phys. 84 (1998) 1776–1781. https://doi.org/10.1063/1.368334.

[63] H.C. Day, D.R. Allee, Selective area oxidation of silicon with a scanning force microscope, Appl. Phys. Lett. 62 (1993) 2691–2693. https://doi.org/10.1063/1.109259.

[64] J.A. Dagata, T. Inoue, J. Itoh, H. Yokoyama, Understanding scanned probe oxidation of silicon, Appl. Phys. Lett. 73 (1998) 271–273. https://doi.org/10.1063/1.121777.

[65] J.A. Dagata, T. Inoue, J. Itoh, K. Matsumoto, H. Yokoyama, Role of space charge in scanned probe oxidation, J. Appl. Phys. 84 (1998) 6891–6900. https://doi.org/10.1063/1.368986.

[66] H. Kuramochi, F. Pérez-Murano, J.A. Dagata, H. Yokoyama, Faradaic current detection during anodic oxidation of the H-passivated p-Si(001) surface with controlled relative humidity, Nanotechnology. 15 (2004) 297–302. https://doi.org/10.1088/0957-4484/15/3/012.

[67] R. Garcia, M. Calleja, Patterning of silicon surfaces with noncontact atomic force microscopy: Field-induced formation of nanometer-size water bridges, J. Appl. Phys. 86 (1999) 1898. https://doi.org/10.1063/1.370985.

[68] H. Kuramochi, K. Ando, H. Yokoyama, Effect of humidity on nano-oxidation of p-Si(001) surface, Surf. Sci. 542 (2003) 56–63. https://doi.org/10.1016/S0039-6028(03)00912-9.

[69] E.S. Snow, G.G. Jernigan, P.M. Campbell, The kinetics and mechanism of scanned probe oxidation of Si, Appl. Phys. Lett. 76 (2000) 1782–1784. https://doi.org/10.1063/1.126166.

[70] B. Theogene, J. Cui, X. Wang, W. Wang, X. Mei, P. Yi, X. Yang, X. He, H. Xie, 3-D finite element calculation of electric field enhancement for nanostructures fabrication mechanism on silicon surface with AFM tip induced local anodic oxidation, Integr. Ferroelectr. 190 (2018) 129–141. https://doi.org/10.1080/10584587.2018.1457346.

[71] T. Cramer, F. Zerbetto, R. García, Molecular Mechanism of Water Bridge Buildup: Field-Induced Formation of Nanoscale Menisci, Langmuir. 24 (2008) 6116–6120. https://doi.org/10.1021/la800220r.

[72] H.J. Choi, J.Y. Kim, S.D. Hong, M.Y. Ha, J. Jang, Molecular simulation of the nanoscale water confined between an atomic force microscope tip and a surface, Mol. Simul. 35 (2009) 466–472. https://doi.org/10.1080/08927020802635129.

[73] J. Gao, X.C. Luo, W. Chang, Z. Wang, Y. Yan, Y. Geng, Insight into Atomic-Scale Adhesion at the C–Cu Interface During the Initial Stage of Nanoindentation, Nanomanufacturing Metrol. 5 (2022) 250–258. https://doi.org/10.1007/s41871-022-00149-3.

[74] X.C. Luo, X.G. Guo, J. Gao, S. Goel, S.Z. Chavoshi, Molecular Dynamics Simulation of Advanced Machining Processes, in: Adv. Mach. Sci., CRC Press, 2022: pp. 385–424. http://dx.doi.org/10.1201/9780429160011-14.

[75] J. Wen, T. Ma, W. Zhang, A.C.T. van Duin, X. Lu, Surface Orientation and Temperature Effects on the Interaction of Silicon with Water: Molecular Dynamics Simulations Using ReaxFF Reactive Force Field, J. Phys. Chem. A. 121 (2017) 587–594. https://doi.org/10.1021/acs.jpca.6b11310.

[76] Y. Sun, Y. Liu, X. Chen, Z. Zhai, F. Xu, Y. Liu, Micromechanism of oxygen transport during initial stage oxidation in Si(100) surface: A ReaxFF molecular

dynamics simulation study, Appl. Surf. Sci. 406 (2017) 178–185. https://doi.org/10.1016/j.apsusc.2017.01.302.

[77] S. Yuan, X. Wang, H. Zhang, S. Yuan, Reactive Molecular Dynamics on the Oxidation of H–Si(100) Surface: Effect of Humidity and Temperature, J. Phys. Chem. C. 124 (2020) 1932–1940. https://doi.org/10.1021/acs.jpcc.9b08702.

[78] Y. Sun, Y.-L. Liu, S. Izumi, X.-F. Chen, Z. Zhai, S.-H. Tian, Initial stage oxidation on nano-trenched Si(1 0 0) surface, J. Phys. Appl. Phys. 51 (2018) 015305. https://doi.org/10.1088/1361-6463/aa99ab.

[79] O. Assowe, O. Politano, V. Vignal, P. Arnoux, B. Diawara, O. Verners, A.C.T. van Duin, Reactive Molecular Dynamics of the Initial Oxidation Stages of Ni(111) in Pure Water: Effect of an Applied Electric Field, J. Phys. Chem. A. 116 (2012) 11796–11805. https://doi.org/10.1021/jp306932a.

[80] L. Ai, H. Huang, Y. Zhou, M. Chen, Y. Lü, The oxidation of Fe/Ni alloy surface with supercritical water: A ReaxFF molecular dynamics simulation, Appl. Surf. Sci. 553 (2021) 149519. https://doi.org/10.1016/j.apsusc.2021.149519.

[81] J. Yeon, S.C. Chowdhury, J.W. Gillespie Jr., Hydroxylation and water-surface interaction for S-glass and silica glass using ReaxFF based molecular dynamics simulations, Appl. Surf. Sci. 608 (2023) 155078. https://doi.org/10.1016/j.apsusc.2022.155078.

[82] X. Jiang, Y. Hu, L. Ling, X. Wang, The initial wet oxidation process on Fe-Cr alloy surface: Insights from ReaxFF molecular dynamic simulations, Appl. Surf. Sci. 548 (2021) 149159. https://doi.org/10.1016/j.apsusc.2021.149159.

[83] L. Ai, Y. Zhou, H. Huang, Y. Lv, M. Chen, A reactive force field molecular dynamics simulation of nickel oxidation in supercritical water, J. Supercrit. Fluids. 133 (2018) 421–428. https://doi.org/10.1016/j.supflu.2017.10.025.

[84] J. Wen, T. Ma, W. Zhang, G. Psofogiannakis, A.C.T. van Duin, L. Chen, L. Qian, Y. Hu, X. Lu, Atomic insight into tribochemical wear mechanism of silicon at the Si/SiO2 interface in aqueous environment: Molecular dynamics simulations using ReaxFF reactive force field, Appl. Surf. Sci. 390 (2016) 216–223. https://doi.org/10.1016/j.apsusc.2016.08.082.

[85] M. Wang, F. Duan, Atomic-Level Material Removal Mechanisms of Si(110) Chemical Mechanical Polishing: Insights from ReaxFF Reactive Molecular Dynamics Simulations, Langmuir. 37 (2021) 2161–2169. https://doi.org/10.1021/acs.langmuir.0c03416.

[86] S. Yuan, X. Guo, P. Li, S. Zhang, M. Li, Z. Jin, R. Kang, D. Guo, F. Liu, L. Zhang, Atomistic understanding of interfacial processing mechanism of silicon in water environment: A ReaxFF molecular dynamics simulation, Front. Mech. Eng. 16 (2021) 570–579. https://doi.org/10.1007/s11465-021-0642-6.

[87] S. Yuan, X. Guo, S. Zhang, C. Zhang, P. Li, Z. Jin, R. Kang, D. Guo, Influence mechanism of defects on the subsurface damage and structural evolution of diamond in CMP process, Appl. Surf. Sci. 566 (2021) 150638. https://doi.org/10.1016/j.apsusc.2021.150638.

[88] Z. Shi, Z. Jin, X. Guo, S. Yuan, J. Guo, Insights into the atomistic behavior in diamond chemical mechanical polishing with OH environment using ReaxFF molecular dynamics simulation, Comput. Mater. Sci. 166 (2019) 136–142. https://doi.org/10.1016/j.commatsci.2019.05.001.

[89] X. Guo, X. Wang, Z. Jin, R. Kang, Atomistic mechanisms of Cu CMP in aqueous H2O2: Molecular dynamics simulations using ReaxFF reactive force field, Comput. Mater. Sci. 155 (2018) 476–482. https://doi.org/10.1016/j.commatsci.2018.09.022.

[90] J. Yeon, A.C.T. van Duin, S.H. Kim, Effects of Water on Tribochemical Wear of Silicon Oxide Interface: Molecular Dynamics (MD) Study with Reactive Force Field (ReaxFF), Langmuir. 32 (2016) 1018–1026. https://doi.org/10.1021/acs.langmuir.5b04062.

[91] Y. Wang, J. Qin, J. Xu, J. Sun, L. Chen, L. Qian, M. Kubo, Definition of Atomic-Scale Contact: What Dominates the Atomic-Scale Friction Behaviors?, Langmuir. 38 (2022) 11699–11706. https://doi.org/10.1021/acs.langmuir.2c01786.

[92] F. Tavazza, T.P. Senftle, C. Zou, C.A. Becker, A.C.T. van Duin, Molecular Dynamics Investigation of the Effects of Tip–Substrate Interactions during Nanoindentation, J. Phys. Chem. C. 119 (2015) 13580–13589. https://doi.org/10.1021/acs.jpcc.5b01275.

[93] R.Md.M. Hasan, O. Politano, X.C. Luo, ReaxFF molecular dynamics simulation study of nanoelectrode lithography oxidation process on silicon (100) surface, Appl. Surf. Sci. 496 (2019) 143679. https://doi.org/10.1016/j.apsusc.2019.143679.

[94] R.Md.M. Hasan, O. Politano, X.C. Luo, Substrate orientation effects on nanoelectrode lithography: ReaxFF molecular dynamics and experimental study, J. Phys. Appl. Phys. 53 (2020) 295108. https://doi.org/10.1088/1361-6463/ab86e2.

[95] E.S. Snow, P.M. Campbell, Fabrication of Si nanostructures with an atomic force microscope, Appl. Phys. Lett. 64 (1994) 1932–1934. https://doi.org/10.1063/1.111746.

[96] I. Tessmer, P. Kaur, J. Lin, H. Wang, Investigating bioconjugation by atomic force microscopy, J. Nanobiotechnology. 11 (2013) 25. https://doi.org/10.1186/1477-3155-11-25.

[97] R. García, M. Calleja, F. Pérez-Murano, Local oxidation of silicon surfaces by dynamic force microscopy: Nanofabrication and water bridge formation, Appl. Phys. Lett. 72 (1998) 2295–2297. https://doi.org/10.1063/1.121340.

[98] S. Gómez-Moñivas, J.J. Sáenz, M. Calleja, R. García, Field-Induced Formation of Nanometer-Sized Water Bridges, Phys. Rev. Lett. 91 (2003) 056101. https://doi.org/10.1103/PhysRevLett.91.056101.

[99] J. Martinez, R.V. Martínez, R. Garcia, Silicon Nanowire Transistors with a Channel Width of 4 nm Fabricated by Atomic Force Microscope Nanolithography, Nano Lett. 8 (2008) 3636–3639. https://doi.org/10.1021/nl801599k.

[100] Y. Gotoh, K. Matsumoto, T. Maeda, E.B. Cooper, S.R. Manalis, H. Fang, S.C. Minne, T. Hunt, H. Dai, J. Harris, C.F. Quate, Experimental and theoretical results of room-temperature single-electron transistor formed by the atomic force microscope nano-oxidation process, J. Vac. Sci. Technol. Vac. Surf. Films. 18 (2000) 1321–1325. https://doi.org/10.1116/1.582347.

[101] B. Legrand, D. Stievenard, Nanooxidation of silicon with an atomic force microscope: A pulsed voltage technique, Appl. Phys. Lett. 74 (1999) 4049–4051. https://doi.org/10.1063/1.123257.

[102] B. Legrand, D. Stiévenard, Atomic force microscope tip-surface behavior under continuous bias or pulsed voltages in noncontact mode, Appl. Phys. Lett. 76 (2000) 1018–1020. https://doi.org/10.1063/1.125925.

[103] M. Calleja, R. García, Nano-oxidation of silicon surfaces by noncontact atomic-force microscopy: Size dependence on voltage and pulse duration, Appl. Phys. Lett. 76 (2000) 3427–3429. https://doi.org/10.1063/1.126856.

[104] N. Clement, D. Tonneau, B. Gely, H. Dallaporta, V. Safarov, J. Gautier, High aspect ratio nano-oxidation of silicon with noncontact atomic force microscopy, J. Vac. Sci. Technol. B Microelectron. Nanometer Struct. 21 (2003) 2348. https://doi.org/10.1116/1.1620513.

[105] A.A. Tseng, Three-dimensional patterning of nanostructures using atomic force microscopes, J. Vac. Sci. Technol. B Nanotechnol. Microelectron. Mater. Process. Meas. Phenom. 29 (2011) 040801. https://doi.org/10.1116/1.3609921.

[106] M. Lorenzoni, B. Torre, Scanning probe oxidation of SiC, fabrication possibilities and kinetics considerations, Appl. Phys. Lett. 103 (2013) 163109. https://doi.org/10.1063/1.4825265.

[107] I. Fernandez-Cuesta, X. Borrisé, F. Pérez-Murano, Atomic force microscopy local oxidation of silicon nitride thin films for mask fabrication, Nanotechnology. 16 (2005) 2731–2737. https://doi.org/10.1088/0957-4484/16/11/045.

[108] M.S. Johannes, D.G. Cole, R.L. Clark, Three-dimensional design and replication of silicon oxide nanostructures using an atomic force microscope, Nanotechnology. 18 (2007) 345304. https://doi.org/10.1088/0957-4484/18/34/345304.

[109] C.-F. Chen, S.-D. Tzeng, H.-Y. Chen, S. Gwo, Silicon microlens structures fabricated by scanning-probe gray-scale oxidation, Opt. Lett. 30 (2005) 652. https://doi.org/10.1364/OL.30.000652.

[110] U.S. Kim, N. Morita, D.W. Lee, M. Jun, J.W. Park, The possibility of multi-layer nanofabrication via atomic force microscope-based pulse electrochemical nanopatterning, Nanotechnology. 28 (2017) 195302. https://doi.org/10.1088/1361-6528/aa6954.

[111] I. Choi, Y. Kim, J. Yi, Fabrication of hierarchical micro/nanostructures via scanning probe lithography and wet chemical etching, Ultramicroscopy. 108 (2008) 1205–1209. https://doi.org/10.1016/j.ultramic.2008.04.076.

[112] Y. Kim, S.K. Kang, I. Choi, J. Lee, J. Yi, Fabrication of a 3-dimensional microstructure by sequential anodic oxidation (SAO), Microelectron. Eng. 84 (2007) 308–312. https://doi.org/10.1016/j.mee.2006.10.084.

[113] Y. Yang, W. Zhao, Fabrication of nanoscale to microscale 2.5D square patterns on metallic films by the coupling AFM lithography, J. Manuf. Process. 46 (2019) 129–138. https://doi.org/10.1016/j.jmapro.2019.08.032.

[114] A. Agarwal, M.J. Kushner, Plasma atomic layer etching using conventional plasma equipment, J. Vac. Sci. Technol. Vac. Surf. Films. 27 (2009) 37–50. https://doi.org/10.1116/1.3021361.

[115] M. Konh, C. He, X. Lin, X. Guo, V. Pallem, R.L. Opila, A.V. Teplyakov, Z. Wang, B. Yuan, Molecular mechanisms of atomic layer etching of cobalt with sequential exposure to molecular chlorine and diketones, J. Vac. Sci. Technol. A. 37 (2019) 021004. https://doi.org/10.1116/1.5082187.

[116] K.S. Kim, K.H. Kim, Y. Nam, J. Jeon, S. Yim, E. Singh, J.Y. Lee, S.J. Lee, Y.S. Jung, G.Y. Yeom, D.W. Kim, Atomic Layer Etching Mechanism of MoS2 for Nanodevices, ACS Appl. Mater. Interfaces. 9 (2017) 11967–11976. https://doi.org/10.1021/acsami.6b15886.

[117] R.C. Longo, A. Ranjan, P.L.G. Ventzek, Density Functional Theory Study of Oxygen Adsorption on Polymer Surfaces for Atomic-Layer Etching: Implications for Semiconductor Device Fabrication, ACS Appl. Nano Mater. 3 (2020) 5189–5202. https://doi.org/10.1021/acsanm.0c00618.

[118] H. Kim, Characteristics and applications of plasma enhanced-atomic layer deposition, Thin Solid Films. 519 (2011) 6639–6644. https://doi.org/10.1016/j.tsf.2011.01.404.

[119] G.N. Parsons, R.D. Clark, Area-Selective Deposition: Fundamentals, Applications, and Future Outlook, Chem. Mater. 32 (2020) 4920–4953. https://doi.org/10.1021/acs.chemmater.0c00722.

[120] R. Chen, Y.-C. Li, J.-M. Cai, K. Cao, H.-B.-R. Lee, Atomic level deposition to extend Moore's law and beyond, Int. J. Extreme Manuf. 2 (2020) 022002. https://doi.org/10.1088/2631-7990/ab83e0.

[121] A.J.M. Mackus, M.J.M. Merkx, W.M.M. Kessels, From the Bottom-Up: Toward Area-Selective Atomic Layer Deposition with High Selectivity, Chem. Mater. 31 (2019) 2–12. https://doi.org/10.1021/acs.chemmater.8b03454.

[122] Y.-C. Li, K. Cao, Y.-X. Lan, J.-M. Zhang, M. Gong, Y.-W. Wen, B. Shan, R. Chen, Inherently Area-Selective Atomic Layer Deposition of Manganese Oxide through Electronegativity-Induced Adsorption, Molecules. 26 (2021) 3056. https://doi.org/10.3390/molecules26103056.

[123] M. Leskelä, J. Niinistö, M. Ritala, Atomic Layer Deposition, Compr. Mater. Process. 4 (2014) 101–123. https://doi.org/10.1016/B978-0-08-096532-1.00401-5.

[124] S.D. Elliott, Atomic-scale simulation of ALD chemistry, Semicond. Sci. Technol. 27 (2012) 074008. https://doi.org/10.1088/0268-1242/27/7/074008.

[125] S.D. Elliott, H.P. Pinto, Modelling the Deposition of High-k Dielectric Films by First Principles, J. Electroceramics. 13 (2004) 117–120. https://doi.org/10.1007/s10832-004-5086-y.

[126] T. Weckman, K. Laasonen, First principles study of the atomic layer deposition of alumina by TMA–H $_2$ O-process, Phys. Chem. Chem. Phys. 17 (2015) 17322–17334. https://doi.org/10.1039/C5CP01912E.

[127] S.D. Elliott, J.C. Greer, Simulating the atomic layer deposition of alumina from first principles, J. Mater. Chem. 14 (2004) 3246. https://doi.org/10.1039/b405776g.

[128] T.P. Senftle, S. Hong, M.M. Islam, S.B. Kylasa, Y. Zheng, Y.K. Shin, C. Junkermeier, R. Engel-Herbert, M.J. Janik, H.M. Aktulga, T. Verstraelen, A. Grama, A.C.T. van Duin, The ReaxFF reactive force-field: development, applications and future directions, Npj Comput. Mater. 2 (2016) 15011. https://doi.org/10.1038/npjcompumats.2015.11.

[129] D. Romine, R. Sakidja, Modeling atomic layer deposition of alumina using reactive force field molecular dynamics, MRS Adv. 7 (2022) 185–189. https://doi.org/10.1557/s43580-022-00271-w.

[130] P.O. Oviroh, R. Akbarzadeh, D. Pan, R.A.M. Coetzee, T.-C. Jen, New development of atomic layer deposition: processes, methods and applications,

Sci. Technol. Adv. Mater. 20 (2019) 465–496. https://doi.org/10.1080/14686996.2019.1599694.

[131] M. Shirazi, S.D. Elliott, Atomistic kinetic Monte Carlo study of atomic layer deposition derived from density functional theory, J. Comput. Chem. 35 (2014) 244–259. https://doi.org/10.1002/jcc.23491.

[132] G. Mazaleyrat, A. Estève, L. Jeloaica, M. Djafari-Rouhani, A methodology for the kinetic Monte Carlo simulation of alumina atomic layer deposition onto silicon, Comput. Mater. Sci. 33 (2005) 74–82. https://doi.org/10.1016/j.commatsci.2004.12.069.

[133] A. Dkhissi, A. Estève, C. Mastail, S. Olivier, G. Mazaleyrat, L. Jeloaica, M. Djafari Rouhani, Multiscale Modeling of the Atomic Layer Deposition of HfO_2 Thin Film Grown on Silicon: How to Deal with a Kinetic Monte Carlo Procedure, J. Chem. Theory Comput. 4 (2008) 1915–1927. https://doi.org/10.1021/ct8001249.

[134] M. Barra, J.C. Scaiano, T.A. Fisher, G.J. Cernigliaro, R. Sinta, J.C. Scaiano, On the Photodecomposition Mechanism of o-Diazonaphthoquinones, J. Am. Chem. Soc. 114 (1992) 2630–2634. https://doi.org/10.1021/ja00033a041.

[135] L. Qin, Y. Huang, F. Xia, L. Wang, J. Ning, H. Chen, X. Wang, W. Zhang, Y. Peng, Q. Liu, Z. Zhang, 5 nm Nanogap Electrodes and Arrays by Super-resolution Laser Lithography, Nano Lett. 20 (2020) 4916–4923. https://doi.org/10.1021/acs.nanolett.0c00978.

[136] A.M. Katzenmeyer, S. Dmitrovic, A.D. Baczewski, Q. Campbell, E. Bussmann, T.-M. Lu, E.M. Anderson, S.W. Schmucker, J.A. Ivie, D.M. Campbell, D.R. Ward, D.A. Scrymgeour, G.T. Wang, S. Misra, Photothermal alternative to

device fabrication using atomic precision advanced manufacturing techniques, J. MicroNanopatterning Mater. Metrol. 20 (2021) 014901. https://doi.org/10.1117/1.JMM.20.1.014901.

[137] M.E. Casida, M. Huix-Rotllant, Progress in Time-Dependent Density-Functional Theory, Annu. Rev. Phys. Chem. 63 (2012) 287–323. https://doi.org/10.1146/annurev-physchem-032511-143803.

[138] R.L. Waterland, K.D. Dobbs, A.M. Rinehart, A.E. Feiring, R.C. Wheland, B.E. Smart, Quantum chemical modeling for 157 nm photolithography, J. Fluor. Chem. 122 (2003) 37–46. https://doi.org/10.1016/S0022-1139(03)00078-2.

[139] C.-A. Palma, K. Diller, R. Berger, A. Welle, J. Björk, J.L. Cabellos, D.J. Mowbray, A.C. Papageorgiou, N.P. Ivleva, S. Matich, E. Margapoti, R. Niessner, B. Menges, J. Reichert, X. Feng, H.J. Räder, F. Klappenberger, A. Rubio, K. Müllen, J.V. Barth, Photoinduced C–C Reactions on Insulators toward Photolithography of Graphene Nanoarchitectures, J. Am. Chem. Soc. 136 (2014) 4651–4658. https://doi.org/10.1021/ja412868w.

[140] S. Ando, DFT Calculations on Refractive Index Dispersion of Fluoro-compounds in the DUV-UV-Visible Region, J. Photopolym. Sci. Technol. 19 (2006) 351–360. https://doi.org/10.2494/photopolymer.19.351.

[141] V.R. Manfrinato, A. Stein, L. Zhang, C.Y. Nam, K.G. Yager, E.A. Stach, C.T. Black, Aberration-Corrected Electron Beam Lithography at the One Nanometer Length Scale, Nano Lett. 17 (2017) 4562–4567. https://doi.org/10.1021/acs.nanolett.7b00514.

[142] W.F. Van Dorp, X. Zhang, B.L. Feringa, J.B. Wagner, T.W. Hansen, J.T.M. De Hosson, Nanometer-scale lithography on microscopically clean graphene,

Nanotechnology. 22 (2011) 505303. https://doi.org/10.1088/0957-4484/22/50/505303.

[143] B. Sommer, J. Sonntag, A. Ganczarczyk, D. Braam, G. Prinz, A. Lorke, M. Geller, Electron-beam induced nano-etching of suspended graphene, Sci. Rep. 5 (2015) 7781. https://doi.org/10.1038/srep07781.

[144] I. Utke, P. Hoffmann, J. Melngailis, Gas-assisted focused electron beam and ion beam processing and fabrication, J. Vac. Sci. Technol. B Microelectron. Nanometer Struct. 26 (2008) 1197. https://doi.org/10.1116/1.2955728.

[145] Z. Wang, J. Zhang, G. Li, Z. Xu, H. Zhang, J. Zhang, A. Hartmaier, F.Z. Fang, Y. Yan, T. Sun, Anisotropy-Related Machining Characteristics in Ultra-Precision Diamond Cutting of Crystalline Copper, Nanomanufacturing Metrol. 3 (2020) 123–132. https://doi.org/10.1007/s41871-020-00060-9.

[146] M. Tripathi, A. Mittelberger, N.A. Pike, C. Mangler, J.C. Meyer, M.J. Verstraete, J. Kotakoski, T. Susi, Electron-Beam Manipulation of Silicon Dopants in Graphene, Nano Lett. 18 (2018) 5319–5323. https://doi.org/10.1021/acs.nanolett.8b02406.

[147] N.S. Smith, J.A. Notte, A.V. Steele, Advances in source technology for focused ion beam instruments, MRS Bull. 39 (2014) 329–335. https://doi.org/10.1557/mrs.2014.53.

[148] J.L. Hanssen, E.A. Dakin, J.J. McClelland, M. Jacka, Using laser-cooled atoms as a focused ion beam source, J. Vac. Sci. Technol. B Microelectron. Nanometer Struct. 24 (2006) 2907. https://doi.org/10.1116/1.2363406.

[149] J.L. Hanssen, J.J. McClelland, E.A. Dakin, M. Jacka, Laser-cooled atoms as a focused ion-beam source, Phys. Rev. A. 74 (2006) 063416. https://doi.org/10.1103/PhysRevA.74.063416.

[150] B. Knuffman, A.V. Steele, J.J. McClelland, Cold atomic beam ion source for focused ion beam applications, J. Appl. Phys. 114 (2013) 044303. https://doi.org/10.1063/1.4816248.

[151] J. Notte, B. Ward, N. Economou, R. Hill, R. Percival, L. Farkas, S. McVey, D.G. Seiler, A.C. Diebold, R. McDonald, C.M. Garner, D. Herr, R.P. Khosla, E.M. Secula, An Introduction to the Helium Ion Microscope, in: AIP Conf. Proc., AIP, Gaithersburg, MD, 2007: pp. 489–496. https://doi.org/10.1063/1.2799423.

[152] E. Mitterreiter, B. Schuler, B. Schuler, K.A. Cochrane, U. Wurstbauer, U. Wurstbauer, A. Weber-Bargioni, C. Kastl, A.W. Holleitner, A.W. Holleitner, Atomistic Positioning of Defects in Helium Ion Treated Single-Layer MoS2, Nano Lett. 20 (2020) 4437–4444. https://doi.org/10.1021/acs.nanolett.0c01222.

[153] D. Winston, B.M. Cord, B. Ming, D.C. Bell, W.F. DiNatale, L.A. Stern, A.E. Vladar, M.T. Postek, M.K. Mondol, J.K.W. Yang, K.K. Berggren, Scanning-helium-ion-beam lithography with hydrogen silsesquioxane resist, J. Vac. Sci. Technol. B Microelectron. Nanometer Struct. 27 (2009) 2702. https://doi.org/10.1116/1.3250204.

[154] D. Fox, Y.B. Zhou, A. O'Neill, S. Kumar, J.J. Wang, J.N. Coleman, G.S. Duesberg, J.F. Donegan, H.Z. Zhang, Helium ion microscopy of graphene: beam damage, image quality and edge contrast, Nanotechnology. 24 (2013) 335702. https://doi.org/10.1088/0957-4484/24/33/335702.

[155] D.S. Fox, Y. Zhou, P. Maguire, A. Oneill, C. Ócoileaín, R. Gatensby, A.M. Glushenkov, T. Tao, G.S. Duesberg, I.V. Shvets, M. Abid, M. Abid, H.C. Wu, Y. Chen, J.N. Coleman, J.F. Donegan, H. Zhang, Nanopatterning and Electrical Tuning of MoS2 Layers with a Subnanometer Helium Ion Beam, Nano Lett. 15 (2015) 5307–5313. https://doi.org/10.1021/acs.nanolett.5b01673.

[156] K. Gamo, N. Takakura, N. Samoto, R. Shimizu, S. Namba, Ion beam assisted deposition of metal organic films using focused ion beams, Jpn. J. Appl. Phys. 23 (1984) L293. https://doi.org/10.1143/JJAP.23.L293.

[157] E. Holmström, A. Kuronen, K. Nordlund, Threshold defect production in silicon determined by density functional theory molecular dynamics simulations, Phys. Rev. B. 78 (2008) 045202. https://doi.org/10.1103/PhysRevB.78.045202.

[158] P. Olsson, C. Becquart, C. Domain, Ab initio threshold displacement energies in iron, Mater. Res. Lett. 4 (2016) 219–225. https://doi.org/10.1080/21663831.2016.1181680.

[159] E. Holmström, K. Nordlund, A. Kuronen, Threshold defect production in germanium determined by density functional theory molecular dynamics simulations, Phys. Scr. 81 (2010) 035601. https://doi.org/dx.doi.org/10.1088/0031-8949/81/03/035601.

[160] J.P. Biersack, L. Haggmark, A Monte Carlo computer program for the transport of energetic ions in amorphous targets, Nucl. Instrum. Methods. 174 (1980) 257–269. https://doi.org/10.1016/0029-554X(80)90440-1.

[161] O.V. Yazyev, I. Tavernelli, U. Rothlisberger, L. Helm, Early stages of radiation damage in graphite and carbon nanostructures: A first-principles molecular

dynamics study, Phys. Rev. B. 75 (2007) 115418. https://doi.org/10.1103/PhysRevB.75.115418.

[162] M. Terrones, H. Terrones, F. Banhart, J.-C. Charlier, P. Ajayan, Coalescence of single-walled carbon nanotubes, Science. 288 (2000) 1226–1229. https://doi.org/10.1126/science.288.5469.1226.

[163] I. Shein, M. Kuznetsov, A. Enyashin, Molecular dynamics simulations of defect formation in thin graphite films using the density functional tight-binding method, J. Struct. Chem. 57 (2016) 808–811. https://doi.org/10.1134/S0022476616040260.

[164] A. Lim, W. Foulkes, A. Horsfield, D. Mason, A. Schleife, E. Draeger, A. Correa, Electron elevator: excitations across the band gap via a dynamical gap state, Phys. Rev. Lett. 116 (2016) 043201. https://doi.org/10.1103/PhysRevLett.116.043201.

[165] A. Ojanperä, A.V. Krasheninnikov, M. Puska, Electronic stopping power from first-principles calculations with account for core electron excitations and projectile ionization, Phys. Rev. B. 89 (2014) 035120. https://doi.org/10.1103/PhysRevB.89.035120.

[166] J. Pruneda, D. Sánchez-Portal, A. Arnau, J. Juaristi, E. Artacho, Electronic stopping power in LiF from first principles, Phys. Rev. Lett. 99 (2007) 235501. https://doi.org/10.1103/PhysRevLett.99.235501.

[167] A.A. Correa, J. Kohanoff, E. Artacho, D. Sánchez-Portal, A. Caro, Nonadiabatic forces in ion-solid interactions: the initial stages of radiation damage, Phys. Rev. Lett. 108 (2012) 213201. https://doi.org/10.1103/PhysRevLett.108.213201.

[168] A.V. Krasheninnikov, Y. Miyamoto, D. Tománek, Role of electronic excitations in ion collisions with carbon nanostructures, Phys. Rev. Lett. 99 (2007) 016104. https://doi.org/10.1103/PhysRevLett.99.016104.

[169] Y. Miyamoto, A. Rubio, D. Tománek, Real-time ab initio simulations of excited carrier dynamics in carbon nanotubes, Phys. Rev. Lett. 97 (2006) 126104. https://doi.org/10.1103/PhysRevLett.97.126104.

[170] F.Z. Fang, The three paradigms of manufacturing advancement, J. Manuf. Syst. 63 (2022) 504–505. https://doi.org/10.1016/j.jmsy.2022.05.007.

[171] H. Mabuchi, The Quantum-Classical Transition on Trial, Eng. Sci. 65 (2002) 22–29.

[172] C. Herzenberg, Why our human-sized world behaves classically, not quantum-mechanically: A popular non-technical exposition of a new idea, ArXiv Prepr. Physics0701155. (2007). https://doi.org/10.48550/arXiv.physics/0701155.

[173] V.E. Campbell, M. Tonelli, I. Cimatti, J.-B. Moussy, L. Tortech, Y.J. Dappe, E. Rivière, R. Guillot, S. Delprat, R. Mattana, Engineering the magnetic coupling and anisotropy at the molecule–magnetic surface interface in molecular spintronic devices, Nat. Commun. 7 (2016) 1–10. https://doi.org/10.1038/ncomms13646.

[174] Y. Cai, W. Chang, X.C. Luo, Y. Qin, Hydrophobicity of pyramid structures fabricated by micro milling, in: 2017 World Congr. Micro Nano Manuf., 2017: pp. 1–4.

[175] M.J. Madou, Fundamentals of microfabrication and nanotechnology, three-volume set, CRC Press, 2018.

[176] K.H. Bennemann, Covalent Bonding in Diamond, Phys. Rev. 139 (1965) A482–A488. https://doi.org/10.1103/PhysRev.139.A482.

[177] A.S. Akhmatov, Molecular physics of boundary friction, Israel program for scientific translations, 1966.

[178] C. Kittel, Introduction to solid state physics, John Wiley & sons, inc, 2005.

[179] X. Wang, S. Ramírez-Hinestrosa, J. Dobnikar, D. Frenkel, The Lennard-Jones potential: when (not) to use it, Phys. Chem. Chem. Phys. 22 (2020) 10624–10633. https://doi.org/10.1039/C9CP05445F.

[180] R. Shankar, Principles of quantum mechanics, Springer Science & Business Media, 2012. https://doi.org/10.1007/978-1-4757-0576-8.

[181] M.C. Payne, M.P. Teter, D.C. Allan, T.A. Arias, J.D. Joannopoulos, Iterative minimization techniques for ab initio total-energy calculations: Molecular dynamics and conjugate gradients, Rev. Mod. Phys. 64 (1992) 1045–1097. https://doi.org/10.1103/RevModPhys.64.1045.

[182] A.C.T. van Duin, S. Dasgupta, F. Lorant, W.A. Goddard, ReaxFF: A Reactive Force Field for Hydrocarbons, J. Phys. Chem. A. 105 (2001) 9396–9409. https://doi.org/10.1021/jp004368u.

[183] K. Chenoweth, A.C.T. van Duin, W.A. Goddard, ReaxFF Reactive Force Field for Molecular Dynamics Simulations of Hydrocarbon Oxidation, J. Phys. Chem. A. 112 (2008) 1040–1053. https://doi.org/10.1021/jp709896w.

[184] H. Lüth, Quantum Physics in the Nanoworld, 2nd ed., Springer Cham, Switzerland, 2013. https://doi.org/10.1007/978-3-319-14669-0.

[185] R. Egerton, Physics of Electron Scattering, in: Electron Energy-Loss Spectrosc. Electron Microsc., 3rd ed., Springer, New York, NY, 2011: pp. 111–229. https://doi.org/10.1007/978-1-4419-9583-4.

[186] Y. Lee, X. Yao, M.V. Fischetti, K. Cho, Real-time ab initio simulation of inelastic electron scattering using the exact, density functional, and alternative approaches, Phys. Chem. Chem. Phys. 22 (2020) 8616–8624. https://doi.org/10.1039/c9cp06376e.

[187] J. Javanainen, J.H. Eberly, Q. Su, Numerical simulations of multiphoton ionization and above-threshold electron spectra, Phys. Rev. A. 38 (1988) 3430–3446. https://doi.org/10.1103/PhysRevA.38.3430.

[188] W. Möller, Fundamentals of ion-surface interaction, Short Resume Lect. (2004).

[189] R.J. Macdonald, The ejection of atomic particles from ion bombarded solids, Adv. Phys. 19 (1970) 457–524. https://doi.org/10.1080/00018737000101161.

[190] A. Elsukova, A. Han, D. Zhao, M. Beleggia, Effect of Molecular Weight on the Feature Size in Organic Ice Resists, Nano Lett. 18 (2018) 7576–7582. https://doi.org/10.1021/acs.nanolett.8b03130.

[191] G. Seniutinas, A. Balčytis, I. Reklaitis, F. Chen, J. Davis, C. David, S. Juodkazis, Tipping solutions: emerging 3D nano-fabrication/ -imaging technologies, Nanophotonics. 6 (2017) 923–941. https://doi.org/10.1515/nanoph-2017-0008.

[192] Y.-L. Zhang, Q.-D. Chen, H. Xia, H.-B. Sun, Designable 3D nanofabrication by femtosecond laser direct writing, Nano Today. 5 (2010) 435–448. https://doi.org/10.1016/j.nantod.2010.08.007.

[193] S. Plimpton, Fast Parallel Algorithms for Short-Range Molecular Dynamics, J. Comput. Phys. 117 (1995) 1–19. https://doi.org/10.1006/jcph.1995.1039.

[194] L. Martínez, R. Andrade, E.G. Birgin, J.M. Martínez, PACKMOL: A package for building initial configurations for molecular dynamics simulations, J. Comput. Chem. 30 (2009) 2157–2164. https://doi.org/10.1002/jcc.21224.

[195] G. Psofogiannakis, A.C.T. van Duin, Development of a ReaxFF reactive force field for Si/Ge/H systems and application to atomic hydrogen bombardment of Si, Ge, and SiGe (100) surfaces, Surf. Sci. 646 (2015) 253–260. https://doi.org/10.1016/j.susc.2015.08.019.

[196] A.C.T. van Duin, C. Zou, K. Joshi, V. Bryantsev, W.A. Goddard, A Reaxff Reactive Force-field for Proton Transfer Reactions in Bulk Water and its Applications to Heterogeneous Catalysis, in: A. Asthagiri, M.J. Janik (Eds.), Comput. Catal., The Royal Society of Chemistry, 2013: pp. 223–243. https://doi.org/10.1039/9781849734905-00223.

[197] J. Wen, T. Ma, W. Zhang, A.C.T. van Duin, X. Lu, Atomistic mechanisms of Si chemical mechanical polishing in aqueous H2O2: ReaxFF reactive molecular dynamics simulations, Comput. Mater. Sci. 131 (2017) 230–238. https://doi.org/10.1016/j.commatsci.2017.02.005.

[198] R.M.M. Hasan, Nanoelectrode lithography: modelling, experimental validation and instrumentation, University of Strathclyde, 2020. http://purl.org/coar/resource_type/c_db06.

[199] H.M. Aktulga, J.C. Fogarty, S.A. Pandit, A.Y. Grama, Parallel reactive molecular dynamics: Numerical methods and algorithmic techniques, Parallel Comput. 38 (2012) 245–259. https://doi.org/10.1016/j.parco.2011.08.005.

[200] J. Chen, T.J. Martínez, Charge conservation in electronegativity equalization and its implications for the electrostatic properties of fluctuating-charge models, J. Chem. Phys. 131 (2009) 044114. https://doi.org/10.1063/1.3183167.

[201] A. Stukowski, Visualization and analysis of atomistic simulation data with OVITO–the Open Visualization Tool, Model. Simul. Mater. Sci. Eng. 18 (2009) 015012. https://doi.org/10.1088/0965-0393/18/1/015012.

[202] L. Pauling, The nature of the chemical bond, Cornell University Press, Ithaca N. Y. (1960).

[203] W.D. Luedtke, U. Landman, Preparation and melting of amorphous silicon by molecular-dynamics simulations, Phys. Rev. B. 37 (1988) 4656–4663. https://doi.org/10.1103/PhysRevB.37.4656.

[204] R.J. Bell, P. Dean, The structure of vitreous silica: Validity of the random network theory, Philos. Mag. 25 (1972) 1381–1398. https://doi.org/10.1080/14786437208223861.

[205] D.I. Grimley, A.C. Wright, R.N. Sinclair, Neutron scattering from vitreous silica IV. Time-of-flight diffraction, J Non Cryst Solids. 119 (1990) 49–64. https://doi.org/10.1016/0022-3093(90)90240-M.

[206] M.V. Coleman, D.J.D. Thomas, The Structure of Silicon Oxide Films, Phys. Status Solidi B. 22 (1967) 593–602. https://doi.org/10.1002/pssb.19670220231.

[207] M. Chander, Y.Z. Li, J.C. Patrin, J.H. Weaver, Si(100)-(2×1) surface defects and dissociative and nondissociative adsorption of H 2 O studied with scanning tunneling microscopy, Phys. Rev. B. 48 (1993) 2493–2499. https://doi.org/10.1103/PhysRevB.48.2493.

[208] M.K. Weldon, B.B. Stefanov, K. Raghavachari, Y.J. Chabal, Initial H 2 O -induced Oxidation of Si(100)– (2 × 1), Phys. Rev. Lett. 79 (1997) 2851–2854. https://doi.org/10.1103/PhysRevLett.79.2851.

[209] G.J. Pietsch, Y.J. Chabal, G.S. Higashi, Infrared-absorption spectroscopy of Si(100) and Si(111) surfaces after chemomechanical polishing, J. Appl. Phys. 78 (1995) 1650–1658. https://doi.org/10.1063/1.360721.

[210] G.J. Pietsch, Y.J. Chabal, G.S. Higashi, The atomic-scale removal mechanism during chemo-mechanical polishing of Si(100) and Si(111), Surf. Sci. 331–333 (1995) 395–401. https://doi.org/10.1016/0039-6028(95)00292-8.

[211] S. Dumpala, S.R. Broderick, U. Khalilov, E.C. Neyts, A.C.T. van Duin, J. Provine, R.T. Howe, K. Rajan, Integrated atomistic chemical imaging and reactive force field molecular dynamic simulations on silicon oxidation, Appl. Phys. Lett. 106 (2015) 011602. https://doi.org/10.1063/1.4905442.

[212] A.S. Kozhukhov, D.V. Scheglov, L.I. Fedina, A.V. Latyshev, The initial stages of atomic force microscope based local anodic oxidation of silicon, AIP Adv. 8 (2018) 025113. https://doi.org/10.1063/1.5007914.

[213] D.B. Asay, S.H. Kim, Evolution of the Adsorbed Water Layer Structure on Silicon Oxide at Room Temperature, J. Phys. Chem. B. 109 (2005) 16760–16763. https://doi.org/10.1021/jp053042o.

[214] S.F. Lyuksyutov, P.B. Paramonov, I. Dolog, R.M. Ralich, Peculiarities of an anomalous electronic current during atomic force microscopy assisted nanolithography on n-type silicon, Nanotechnology. 14 (2003) 716–721. https://doi.org/10.1088/0957-4484/14/7/305.

[215] D. Graf, M. Frommenwiler, P. Studerus, T. Ihn, K. Ensslin, D.C. Driscoll, A.C. Gossard, Local oxidation of Ga[Al]As heterostructures with modulated tip-sample voltages, J. Appl. Phys. 99 (2006) 053707. https://doi.org/10.1063/1.2176162.

[216] J.A. Dagata, F. Perez-Murano, C. Martin, H. Kuramochi, H. Yokoyama, Current, charge, and capacitance during scanning probe oxidation of silicon. I. Maximum charge density and lateral diffusion, J. Appl. Phys. 96 (2004) 2386–2392. https://doi.org/10.1063/1.1771820.

[217] A.A. Tseng, A. Notargiacomo, T.P. Chen, Y. Liu, Profile Uniformity of Overlapped Oxide Dots Induced by Atomic Force Microscopy, J. Nanosci. Nanotechnol. 10 (2010) 4390–4399. https://doi.org/10.1166/jnn.2010.2361.

[218] Y. Ma, G. Ballesteros, J.M. Zajac, J. Sun, B.D. Gerardot, Highly directional emission from a quantum emitter embedded in a hemispherical cavity, Opt. Lett. 40 (2015) 2373. https://doi.org/10.1364/OL.40.002373.

[219] M. Wieland, J. Pradelles, S. Landis, L. Pain, G. Rademaker, I. Servin, G.D. Boer, P. Brandt, R.J.A. Jager, S.W.H.K. Steenbrink, Performance validation of Mapper's FLX-1200 (Conference Presentation), in: Nov. Patterning Technol. Semicond. MEMSNEMS MOEMS 2019, SPIE, 2019: p. 109580I. https://doi.org/10.1117/12.2514920.

[220] Andrew J. Hazelton, Andrea Wüest, Greg Hughes, Lloyd C. Litt, Frank Goodwin, Cost of ownership for future lithography technologies, in: SPIE Lithogr. Asia - Taiwan, 2008: p. 71401Q. https://doi.org/10.1117/12.804711.

[221] M. Kock, V. Kirchner, R. Schuster, Electrochemical micromachining with ultrashort voltage pulses–a versatile method with lithographical precision,

Electrochimica Acta. 48 (2003) 3213–3219. https://doi.org/10.1016/S0013-4686(03)00374-8.

[222] H. Zhou, Y. Jiang, C.M. Dmuchowski, C. Ke, J. Deng, Electric-Field-Assisted Contact Mode Atomic Force Microscope-Based Nanolithography With Low Stiffness Conductive Probes, J. Micro Nano-Manuf. 10 (2022) 011001. https://doi.org/10.1115/1.4054316.

[223] F. Lavini, N. Yang, R.K. Vasudevan, E. Strelcov, S. Jesse, M.B. Okatan, I. Kravchenko, D. Di Castro, S.V. Kalinin, G. Balestrino, C. Aruta, V. Foglietti, Bias assisted scanning probe microscopy direct write lithography enables local oxygen enrichment of lanthanum cuprates thin films, Nanotechnology. 26 (2015) 325302. https://doi.org/10.1088/0957-4484/26/32/325302.

[224] J. Zhao, L.A. Swartz, W. Lin, P.S. Schlenoff, J. Frommer, J.B. Schlenoff, G. Liu, Three-Dimensional Nanoprinting *via* Scanning Probe Lithography-Delivered Layer-by-Layer Deposition, ACS Nano. 10 (2016) 5656–5662. https://doi.org/10.1021/acsnano.6b01145.

[225] J. Fait, J. Čermák, J. Stuchlík, B. Rezek, Complex nano-patterning of structural, optical, electrical and electron emission properties of amorphous silicon thin films by scanning probe, Appl. Surf. Sci. 428 (2018) 1159–1165. https://doi.org/10.1016/j.apsusc.2017.09.228.